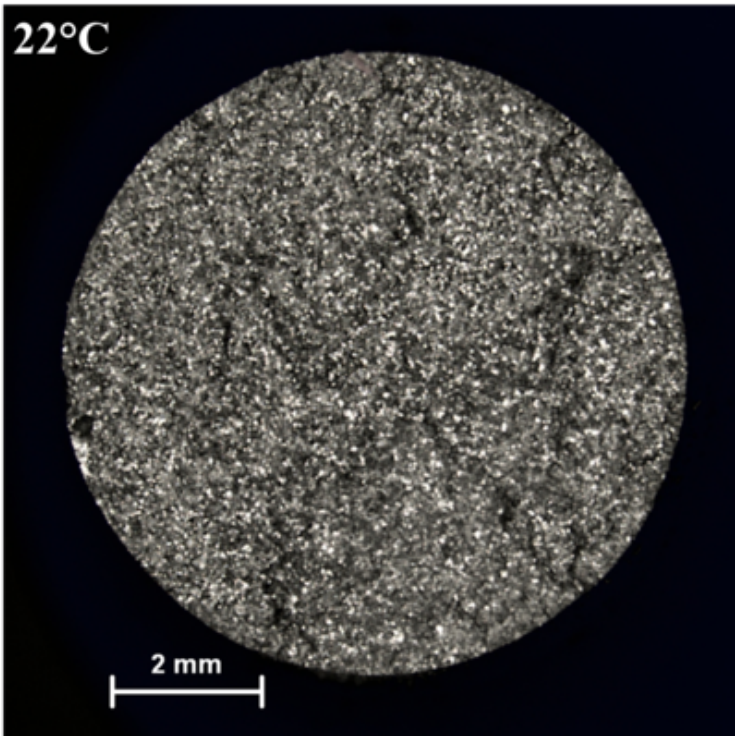

(a)

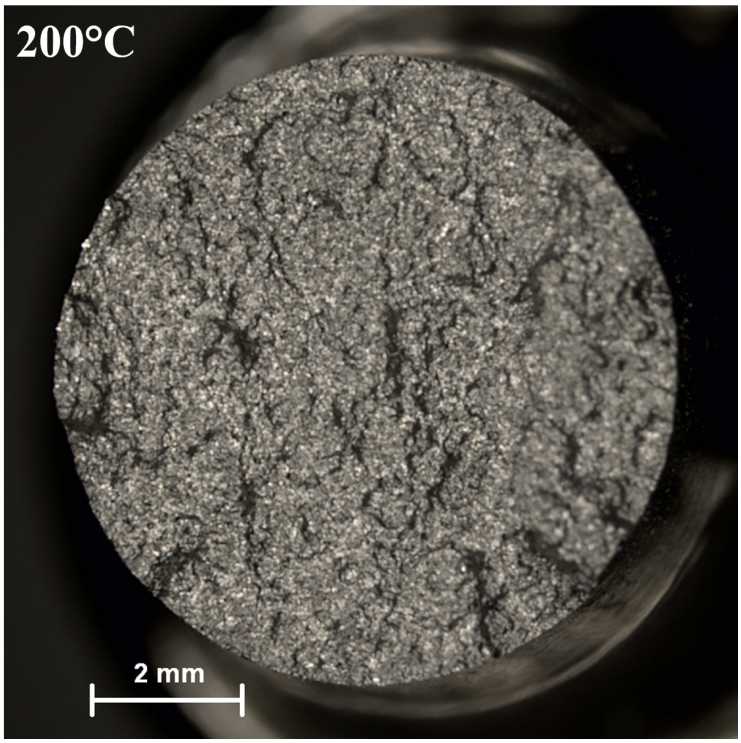

(b)

Figure 2.26: Optical microscope images of the fracture surfaces obtained from LCF tests at high strain levels at (a) room temperature and (b) 200 °C. Continued on next page, (c) 400 °C, (d) 600 °C, (e) 720 °C and (f) 800 °C.

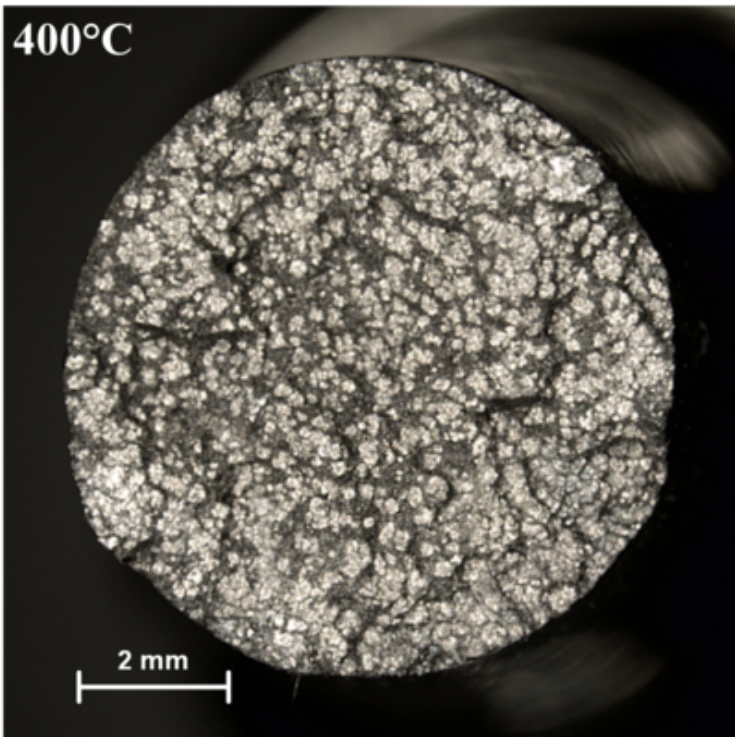

(c)

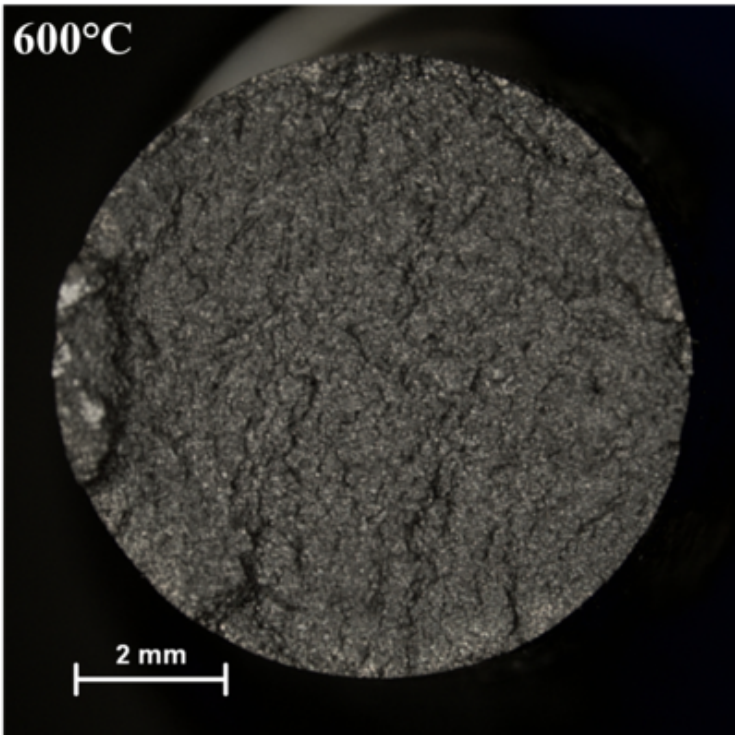

(d)

Figure 2.26: Continued from previous page.

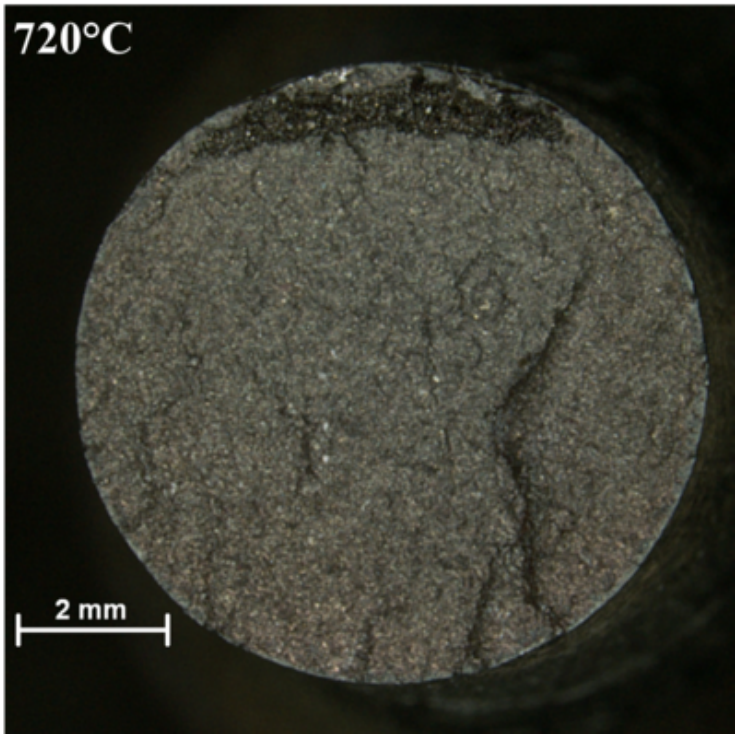

(e)

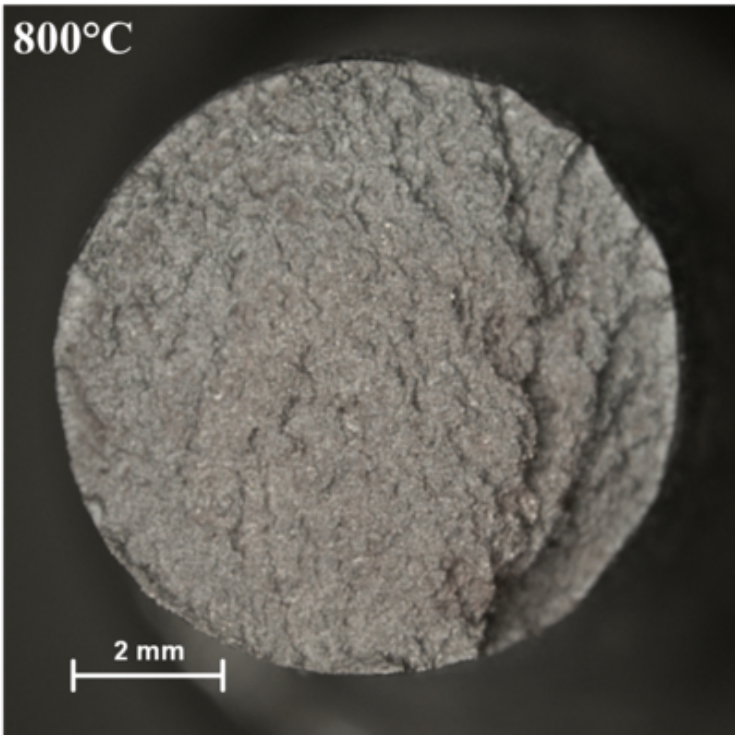

(f)

Figure 2.26: Continued from previous page.

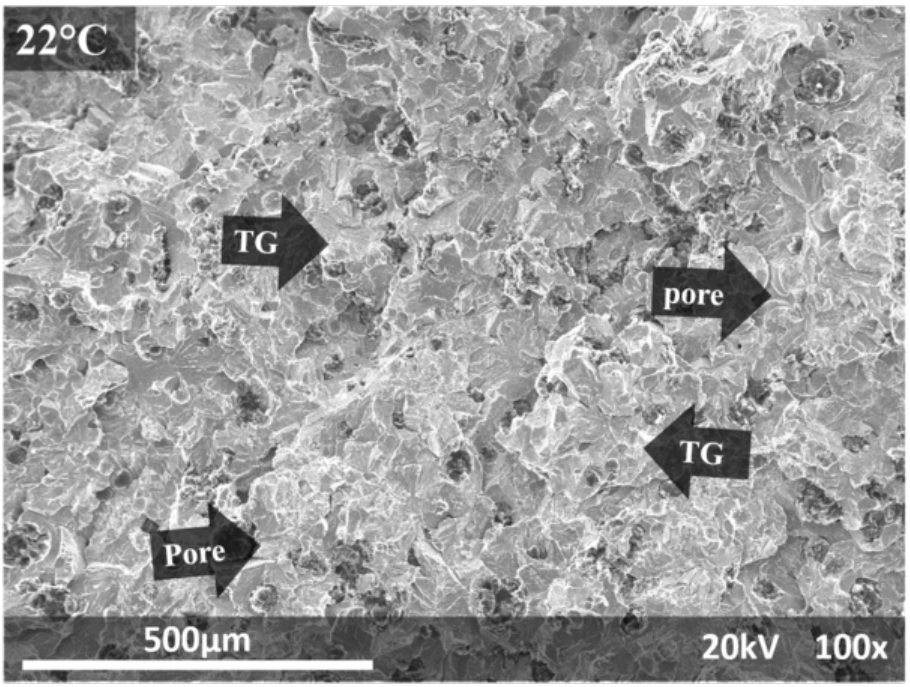

(a)

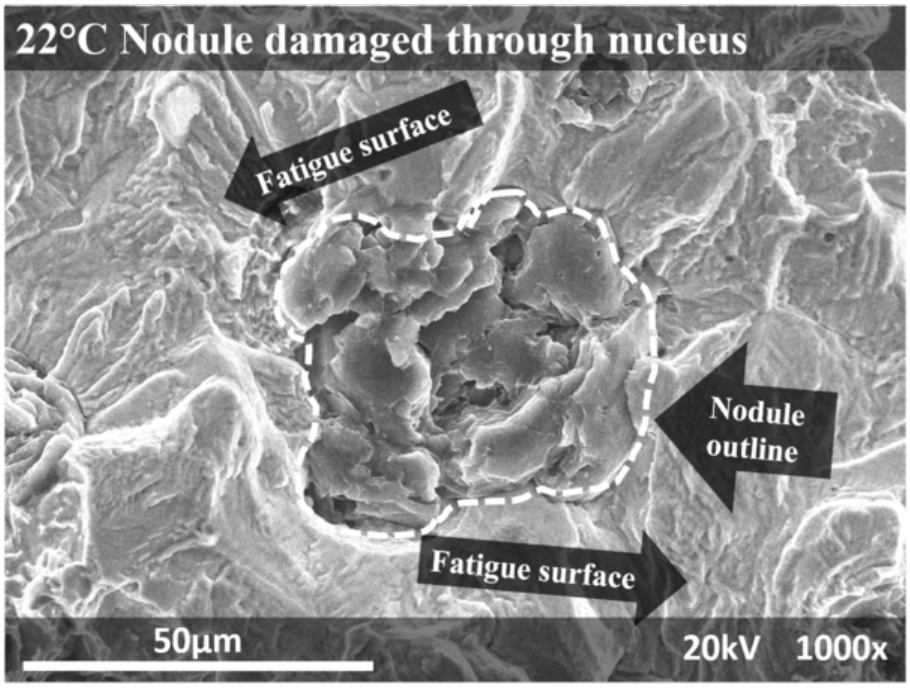

(b)

Figure 2.27: SEM images of (a) the fracture surface of a specimen tested under LCF at room temperature and (b) a graphite nodule which has fractured through the nucleus with adjacent fatigue fracture. Continued on next page, SEM image of (c) transgranular cleavage.

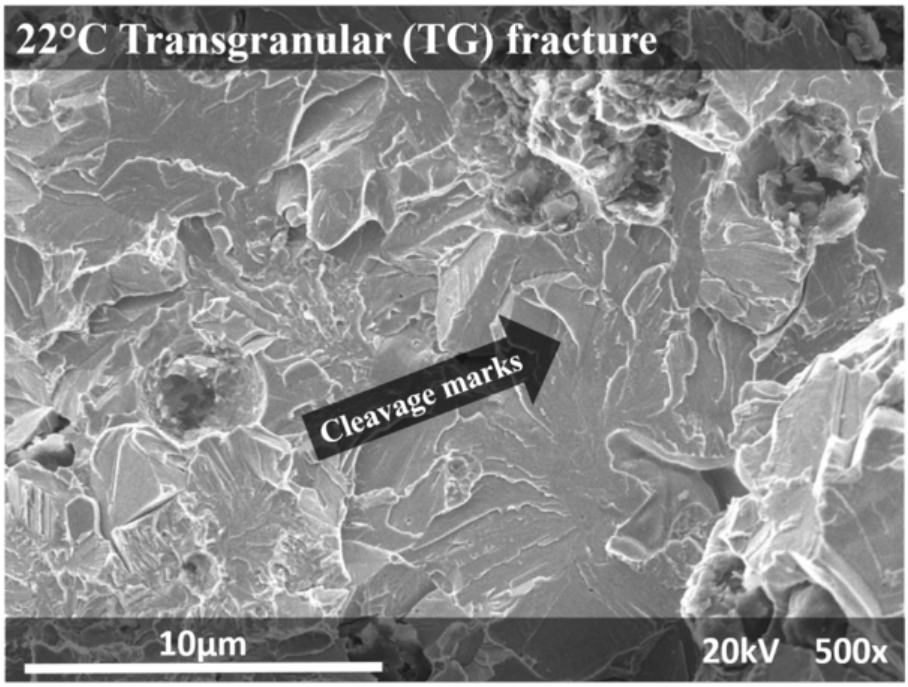

(c)

Figure 2.27: Continued from previous page.

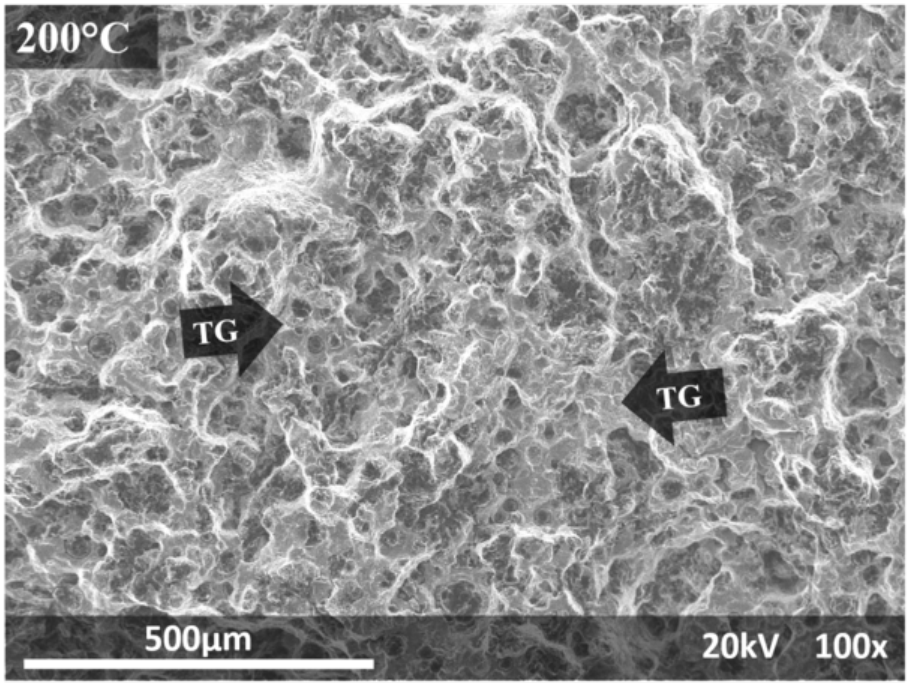

(a)

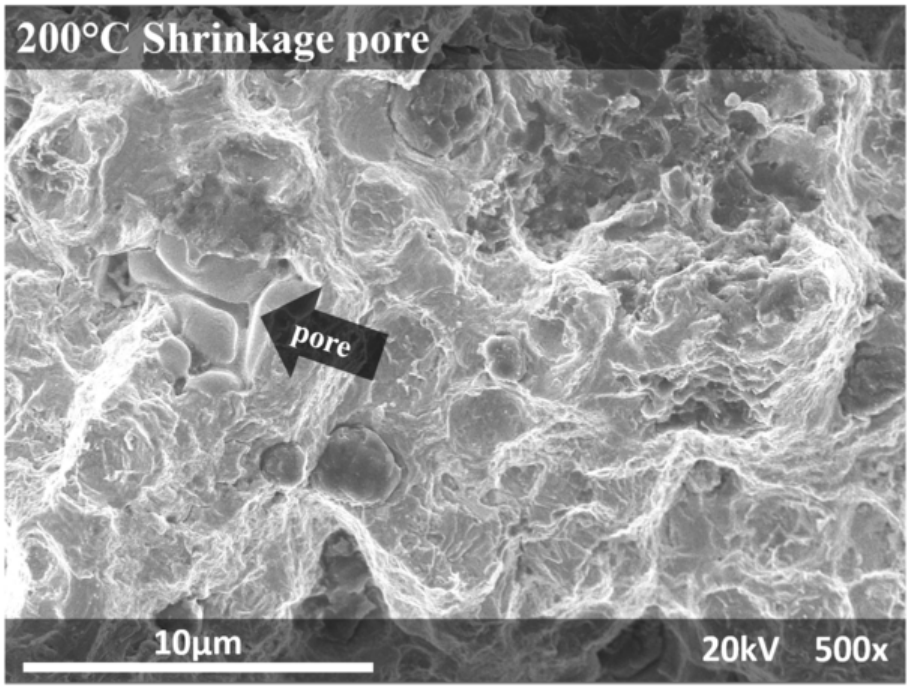

(b)

Figure 2.28: SEM images of (a) the fracture surface of a specimen tested under LCF at 200 °C and (b) a magnified view of the fracture surface.

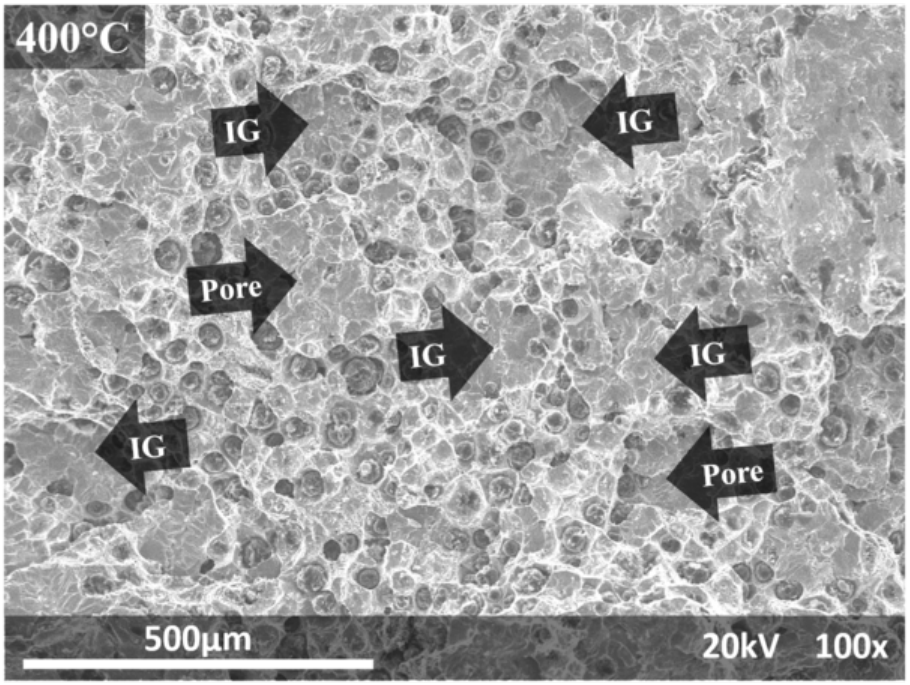

(a)

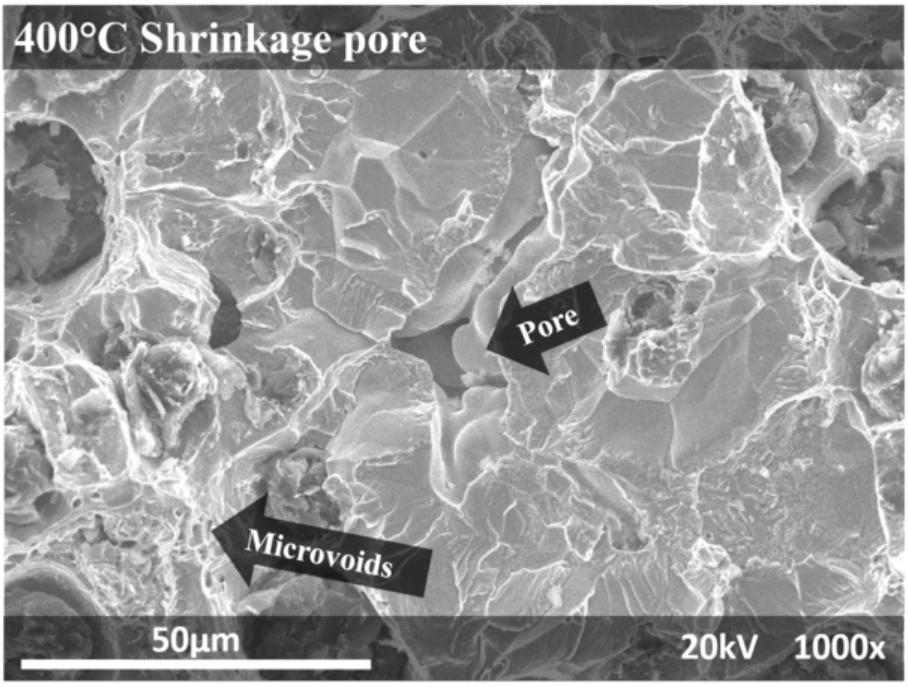

(b)

Figure 2.29: SEM images of (a) the fracture surface of a specimen tested under LCF at 400 °C and (b) intergranular facets. Continued on next page, SEM images of (c) shrinkage pore and (d) ductile microvoids (dimples).

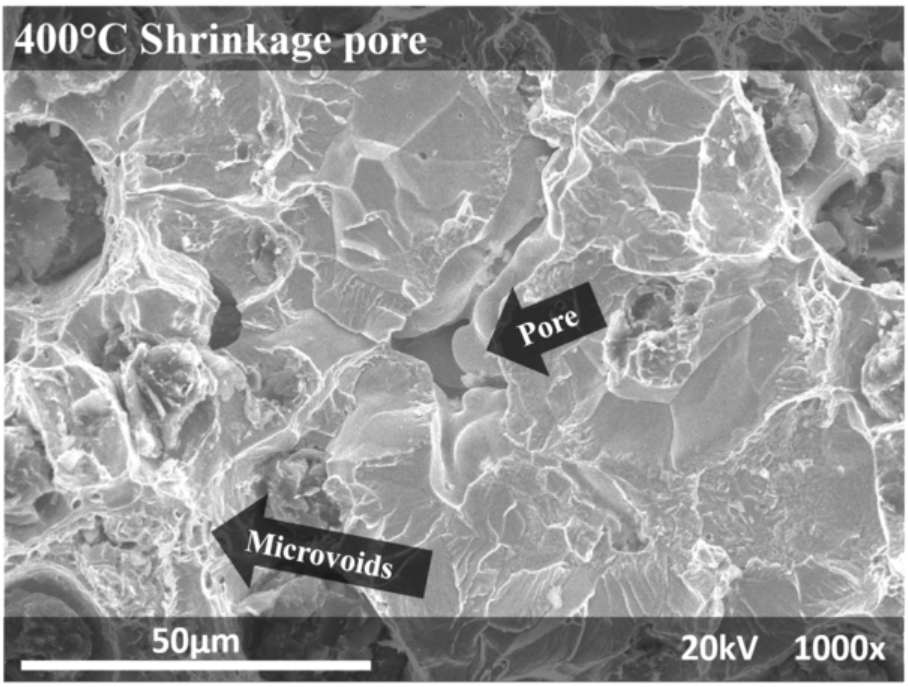

(c)

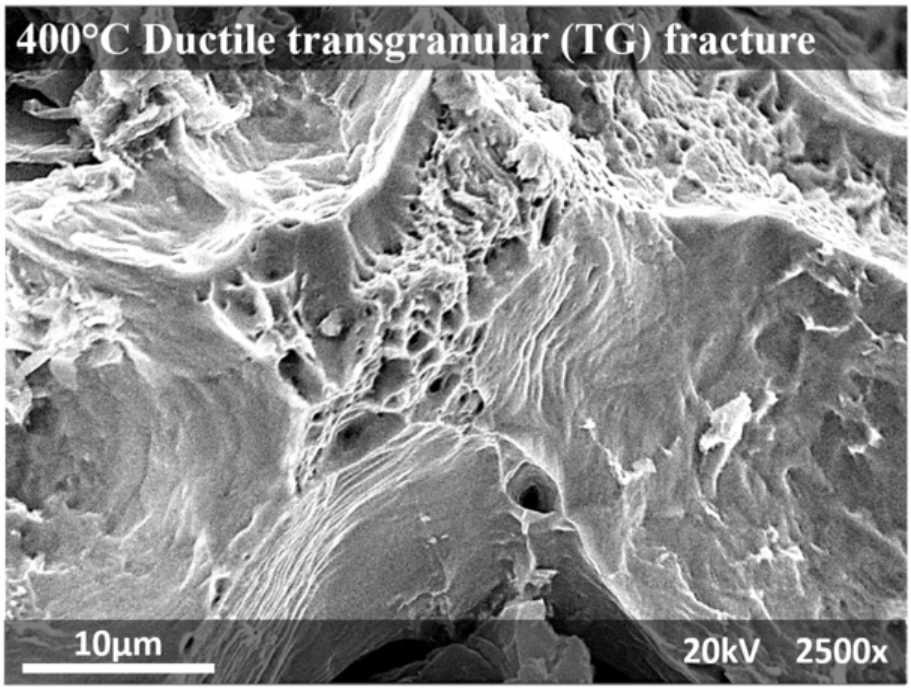

(d)

Figure 2.29: Continued from previous page.

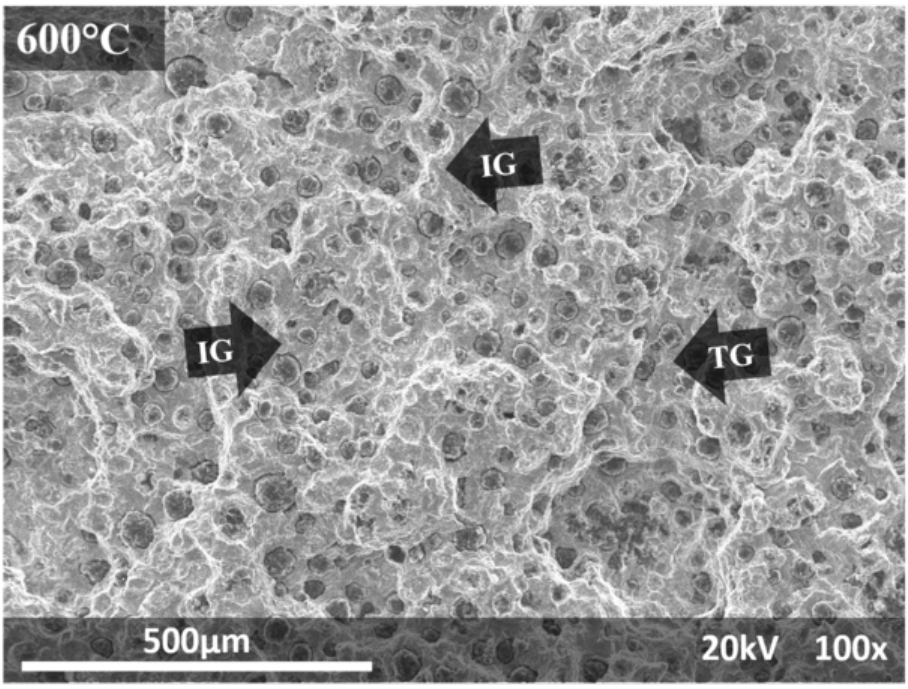

Figure 2.30: SEM image of the fracture surface of a specimen tested under LCF at 600 °C.

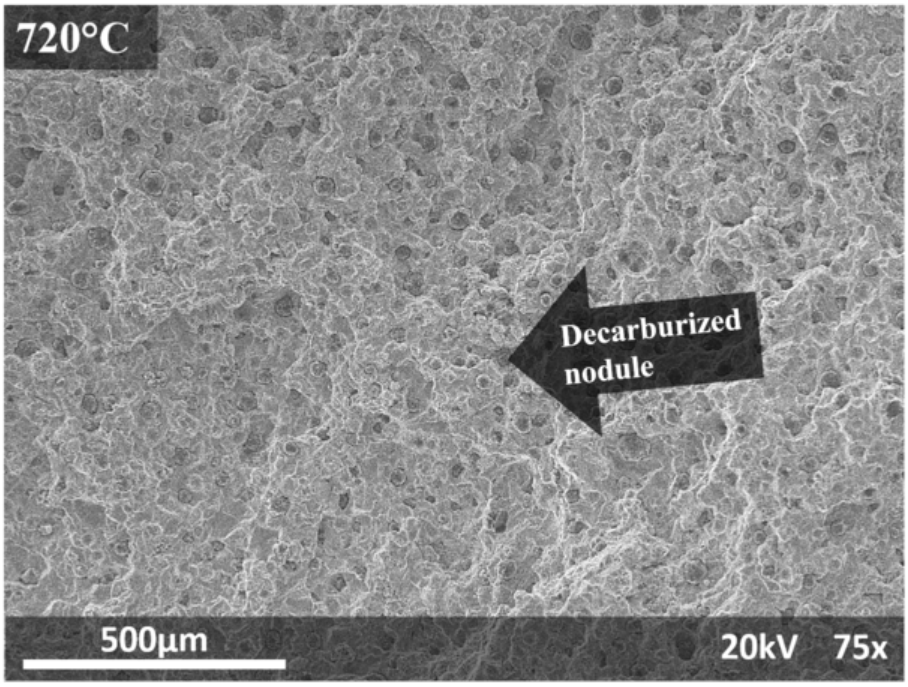

Figure 2.31: SEM image of the fracture surface of a specimen tested under LCF at 720 °C.

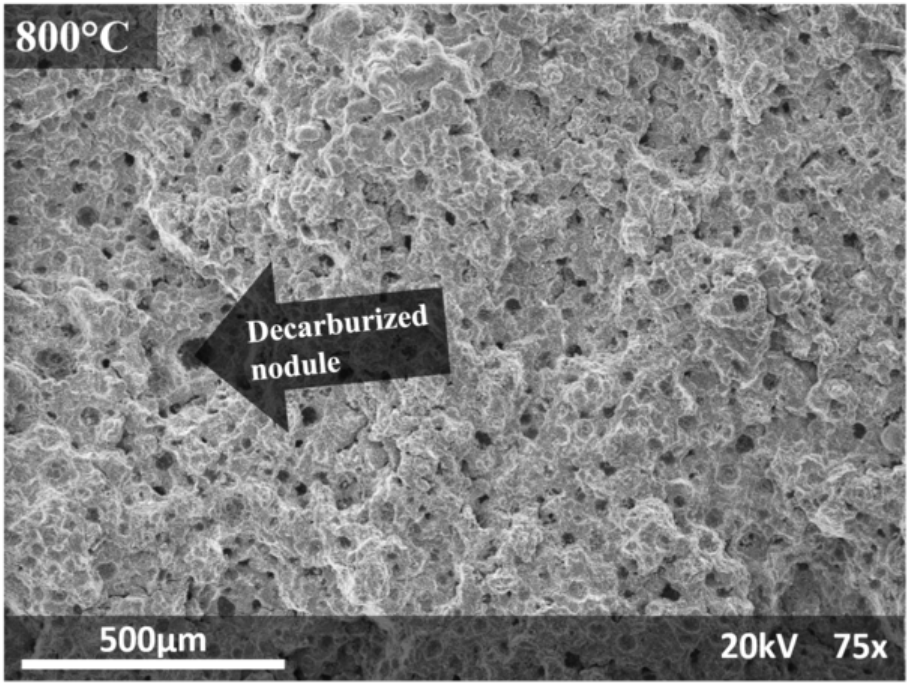

Figure 2.32: SEM image of the fracture surface of a specimen tested under LCF at 800 °C.

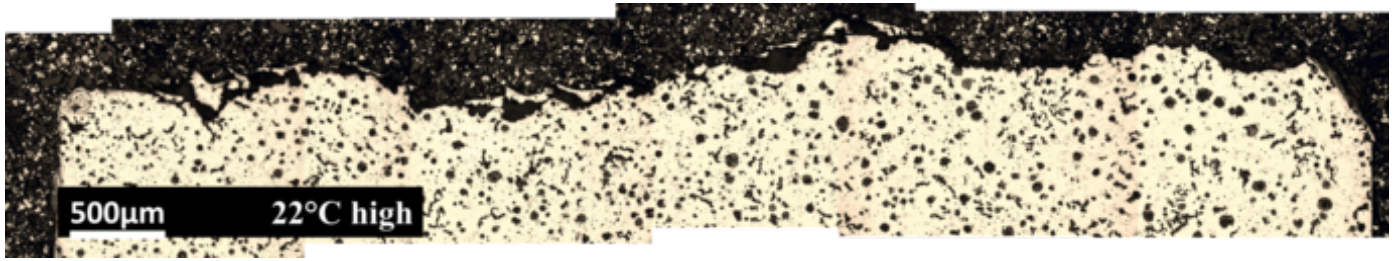

(a)

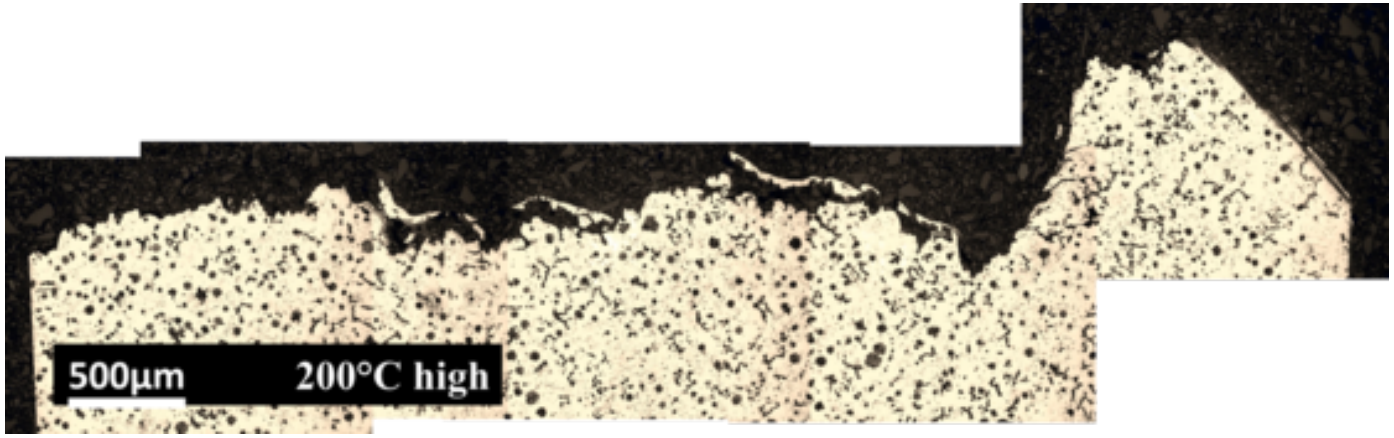

(b)

Figure 2.33: Optical micrographs longitudinal cross-sections through the fracture surface in specimens tested at a high strain level under low cycle fatigue at (a) room temperature and (b) 200 °C. Continued on next page, (c) 400 °C, (d) 600 °C, (e) 720 °C and (f) 800 °C.

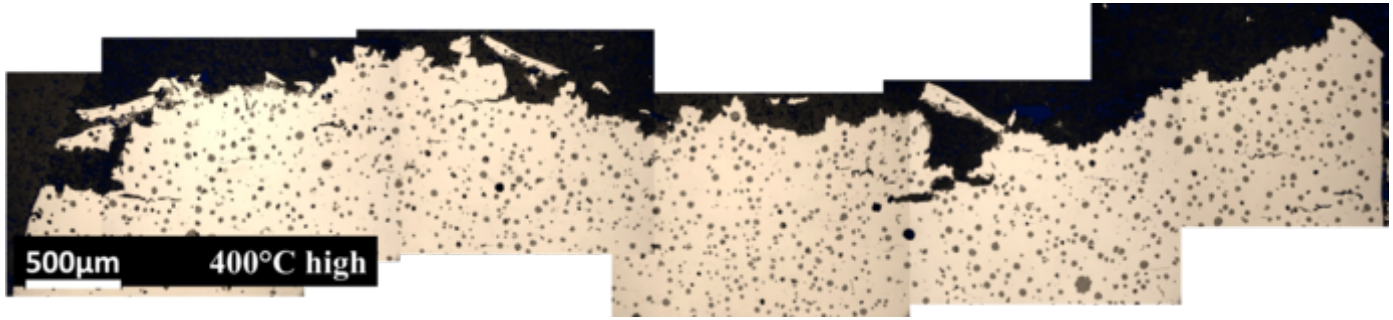

(c)

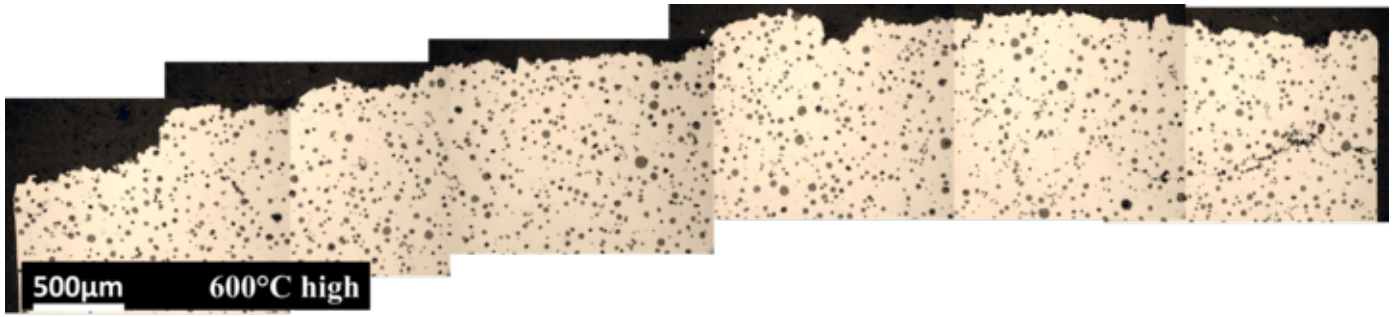

(d)

Figure 2.33: Continued from previous page.

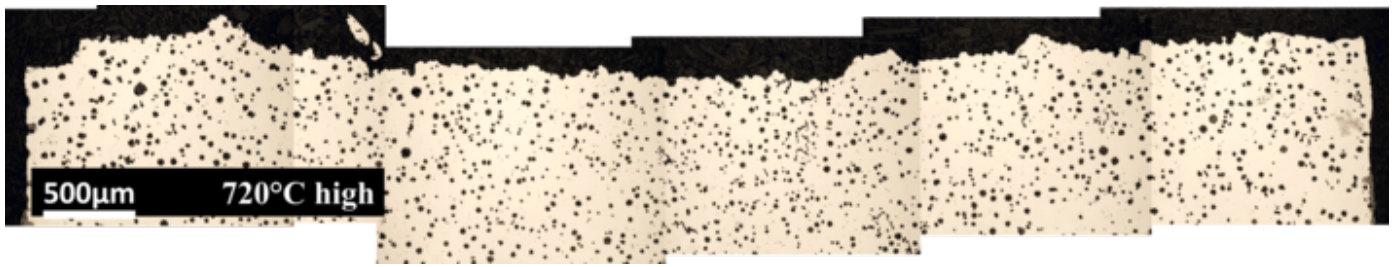

(e)

(f)

Figure 2.33: Continued from previous page.

2.4.3 Discussion

Both applied strain and temperature influence the failure mode that ultimately results in fatigue fracture of HiSiMo DCI. At low strain ranges, fracture initiates at shrinkage pores that intersect the specimen surface. Shrinkage pores serve as stress concentrators. Additionally, shrinkage pores are associated with intergranular spaces where impurity elements collect during solidification of the alloy. Thus, the mechanical properties in these regions can be affected by local gradients in composition and microstructure. Once the fatigue crack initiates at low strain ranges, it propagates over a measurable distance prior to the occurrence of the final tensile fracture. At high strain ranges, there is no clear nucleation site of a primary fatigue crack, and fatigue crack nucleation and propagation tends to occur by intergranular fracture. In particular, at the embrittled temperature and at high temperatures, the propagation of the fatigue crack occurs by predominant intergranular fracture. The effect of embrittlement is pronounced at high strain ranges at 400 °C, where the short fatigue life is significantly reduced from the other tested temperatures. Fractographic and chemical observations on the fracture surface show the presence of embrittled grain boundaries. In this way, it is clear that the embrittlement which occurs in HiSiMo significantly impacts the low cycle fatigue performance of the alloy, particularly when the strain (or stress) is high.

The energetically-favorable damage modes can be related to the phenomenological strain-life behaviors that were discovered in low cycle fatigue tests at various temperatures. At low levels of strain, the durability of the HiSiMo material is most critically influenced by its strength and transgranular fracture is predominant, particularly at lower temperatures. At high strain levels, ductility is of critical importance to influence the fatigue life, and failure in HiSiMo DCI tended to occur via intergranular fracture.

Transgranular fracture can be ductile and mediated by the mobility of dislocations,

or it can be brittle due to the preferential breaking of atomic bonds on specific crystallographic planes. The ductile mode of fracture is associated with the highest degree of energy dissipation. On the other hand, the tendency of a material to intergranular fracture is related to a lack of ability to plastically deform. Intergranular fracture is a brittle, and is associated with the lowest level of energy dissipation. Intergranular fracture thus corresponds to fatigue at high strain levels, at high temperatures, or at the temperature of minimum ductility.

2.4.4 Summary of the Low Cycle Behavior and Failure Modes of HiSiMo DCI

A thorough examination of the low cycle fatigue behavior of HiSiMo DCI was conducted to learn the relevant damage modes which can influence the strain-life behavior of the material at elevated temperatures. The key findings of the LCF characterization of the HiSiMo DCI considered in the present study are summarized below:

1. The fatigue strength coefficient generally decreases with temperature, and the fatigue ductility coefficient generally increases with temperature,
2. Fatigue crack nucleation and propagation tends to occur in a transgranular manner, except when the temperature is near 400 °C,
3. Fatigue crack growth tends to occur in a predominantly intergranular manner near 400 °C; thus, the LCF performance is significantly reduced at 400 °C due to embrittlement of the grain boundaries,

From these observations, it is clear that transgranular fracture is the most energetically favorable mode of damage when the temperature and strain are low. However, as the temperature or strain increase, intergranular fracture becomes more energetically favorable. Additionally, when the temperature is near 400 °C, the embrittled fracture of grain boundaries becomes energetically favorable, regardless of the applied strain.

CHAPTER III

Thermomechanical Fatigue Characterization

As discussed in Chapter I, exhaust manifolds and turbocharger housings are subjected to severe thermal cycles throughout their lives due to the start-stop cycles of the engine. When the hot exhaust gas flows through the interior of the manifold, it generates mechanical strains due to the thermal gradient along the manifold wall. The combination of thermal cycling and mechanical fatigue can, in the general case, drastically reduce the longevity of the component compared to isothermal fatigue behavior. For example, *Jaske* (1976) showed that isothermal fatigue properties are non-conservative for cases of thermal cycling. Thus, to accurately predict the durability of high temperature engine components, it is imperative to understand the coupled thermomechanical fatigue (TMF) behavior of the structural material.

In an effort to fully characterize the effect of coupled thermal and mechanical cycling on the durability and failure behavior of HiSiMo DCI for a realistic range of operating conditions, thermomechanical fatigue (TMF) tests were conducted for 62 specimens of HiSiMo DCI with varying maximum and minimum temperatures, and hold times at the maximum temperature. The test procedures and results are described in the following sections, along with fractography to characterize the relevant damage processes under these loading conditions.

Portions of this chapter have been published in *Avery et al.* (2015).

3.1 Generalities

TMF laboratory tests involve simultaneous cycling of temperature and strain. In a laboratory setting, TMF cycles can be applied in-phase (IP), where the maximum strain and temperature coincide, or out-of-phase (OP), where the maximum strain coincides with the minimum temperature (*ASTM E2368*, 2010). Figure 3.1 schematically illustrates IP and OP TMF loading. Any phasing between fully IP and fully OP can be realized in a physical component during a typical engine load cycle, and can be simulated in a modern TMF laboratory test. It is usually necessary to conduct tests that are representative of both IP and OP behavior to fully characterize the TMF behavior of a material. TMF tests are conducted under total strain control according to

$$\varepsilon_{total} = \varepsilon_{th} + \varepsilon_{mech} \tag{3.1}$$

where ε_{th} is the thermal strain, and ε_{mech} is the applied mechanical strain.

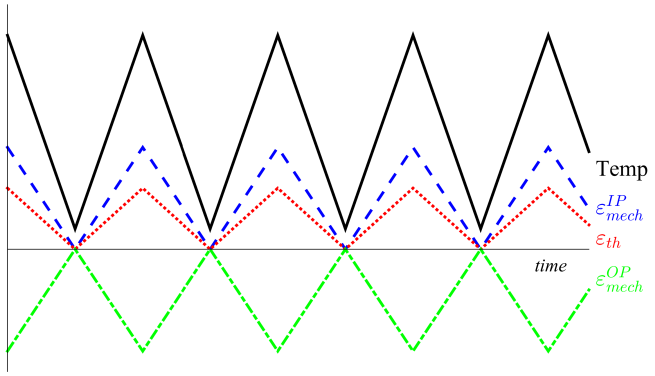

Figure 3.1: Illustration of in-phase (IP) and out-of-phase (OP) cycling of temperature and strain.

3.2 Test Procedure

Thermomechanical fatigue tests were conducted on specimens of HiSiMo DCI to determine the TMF life and failure behavior of the material. Tests were conducted at Ford's Research and Innovation Center in Dearborn, MI. Specimens with a geometry according to *ASTM E2368* (2010) were used. Specimens were machined on a lathe from the cast bars described in Chapter II, Section 2.2.2, and the shoulders of the specimens were cut with threads to facilitate placement in the high-temperature grips. Following machining, TMF specimens were polished using low-stress grinding parallel to the longitudinal axis of the specimen. The surface of each specimen was visually inspected and was found to be free from large machining marks or defects. The diameter of each specimen was measured with a shadowgraph at three locations in the reduced section of the specimen, and the average diameter was used for the calculation of stress. The diameter measurements ranged from 7.61 to 7.63 mm with most specimens measuring 7.62 mm.

For further details of the experimental set-up, and temperature and strain measurement, the reader is referred to Chapter II, Section 2.3.1. Additional cooling was utilized for the TMF tests via proportionally-controlled fans positioned radially around the specimen to achieve a linear cooling rate to the lowest tested temperature. Constant heating and cooling rates of $3.5\,^{\circ}\mathrm{C\,s^{-1}}$ were used for all TMF tests such that the total time of a TMF cycle ranged from 120 to 286 s. This resulted in a strain rate that varied from about $1 \times 10^{-5}\,\mathrm{s^{-1}}$ to about $3.5 \times 10^{-4}\,\mathrm{s^{-1}}$, based on the applied strain range and the limits of the thermal cycle.

The specimens were assembled into the test frame and the elastic modulus was measured from ten fully elastic, isothermal cycles conducted under load control at 1 Hz. The modulus was measured for each specimen at temperatures ranging from the minimum to the maximum test temperatures, in 50 °C increments to allow an accurate calculation of the elastic and inelastic portions of strain throughout the anisothermal

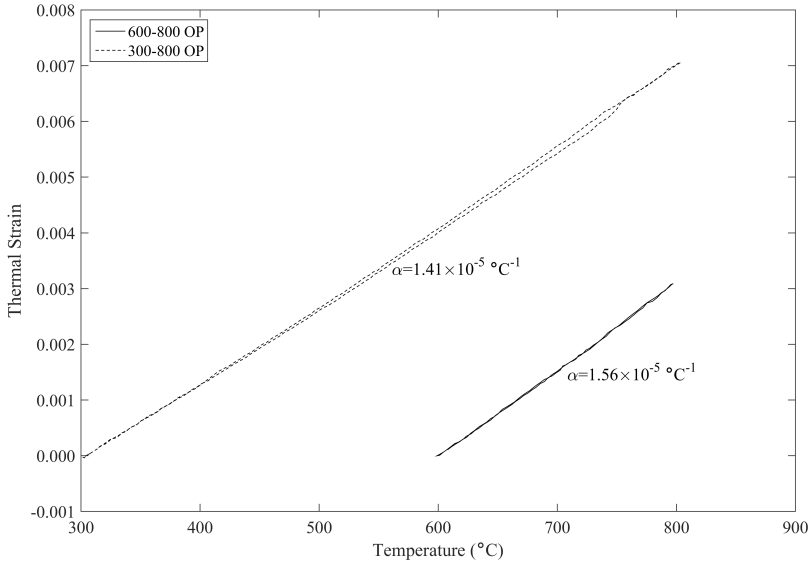

Figure 3.2: Strain-temperature loops for the stabilized zero-load cycle in the temperature ranges 300 to 800 °C and 600 to 800 °C. The measured values of α for each cycle are reported.

cycle. The specimen was then cycled from the minimum to the maximum temperature under zero load to allow the specimen temperature to reach a dynamic equilibrium. The thermal strain and coefficient of thermal expansion (α) were measured from the stabilized thermal cycle. Figure 3.2 shows the thermal strain for a TMF cycle for two temperature ranges. The slope of the curve gives the coefficient of thermal expansion.

The TMF cycles were started from the minimum temperature under total strain control. TMF life was determined by a 50 % drop in maximum load from the stabilized value. Tests were discontinued at 10,000 cycles.

3.3 Results

3.3.1 Effect of Reducing Minimum Cycle Temperature

The maximum service temperature for HiSiMo DCI is limited to approximately 810 °C to avoid the transformation of ferrite in the matrix to austenite (*Sponseller et al.*, 1968; *Li et al.*, 2004). Thus, the maximum temperature used for TMF tests

in this study was 800 °C. The minimum temperature of the thermal cycle was varied from 600 to 300 °C to change the proportion of creep, oxidation and fatigue damage that would accumulate in each cycle. In particular, it was of critical importance to extend the temperature cycle below 400 °C to determine the influence of the embrittlement on TMF life and failure behavior.

Figure 3.3 shows the strain-life curve for tests conducted with a constant maximum temperature of 800 °C, and minimum temperature from 600 to 300 °C. As shown in Figure 3.3, decreasing the minimum temperature from 600 to 500 °C, and again to 400 °C, results in a decrease in TMF life. The slope of the strain-life curve decreases as the minimum temperature decreases. Further decreasing the minimum cycle temperature to 300 °C did not result in a further loss of TMF life, and there is no difference in the strain-life curve for minimum cycle temperatures of 300 and 400 °C.

For IP TMF, decreasing the minimum cycle temperature from 600 °C to 300 °C resulted in no change in fatigue life, as shown in Figure 3.3. The IP TMF life is very similar to the OP TMF life in the temperature range 600 to 800 °C, but is significantly longer than the OP life in the temperature range 300 to 800 °C.

To understand the difference between the OP and IP TMF lives observed for varying minimum cycle temperatures, the stabilized stress-strain loops were examined for each loading case. The HiSiMo DCI was found to be cyclically stable under conditions of OP and IP TMF, as shown in Figure 3.4. The mid-life stress-strain loops are shown in Figure 3.5a for a mechanical strain range of approximately 0.005, and for temperature ranges of 300 to 800 °C and 600 to 800 °C. Recall that the OP and IP TMF lives showed no difference for the temperature range of 600 to 800 °C; the fatigue lives represented in Figure 3.5a for this temperature range are 975 cycles to failure for the OP TMF life, and 1500 cycles to failure for the IP TMF life. Conversely, the greatest difference between OP and IP TMF life was observed for the temperature

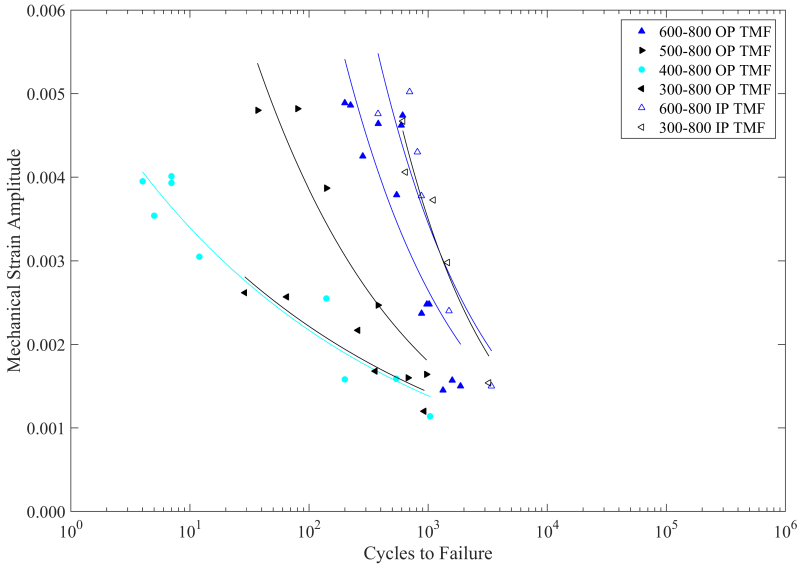

Figure 3.3: TMF life as a function of mechanical strain amplitude for different minimum temperatures for in-phase (IP) and out-of-phase (OP) loading.

range 300 to 800 °C; the OP TMF life represented in the image is 29 cycles to failure for this temperature range, and the IP TMF life is 1460 cycles to failure. Comparing the OP and IP loops for each thermal cycle, it is clear that the area of the two loops, as well as the strain ranges and stress ranges are very similar for the two loading cases. The maximum stress is lower in the IP TMF case than the OP TMF case for both thermal cycles.

When considering the thermal cycle 600 to 800 °C, there is no difference in the IP and OP TMF lives, despite the maximum stress being lower in the IP TMF case. This would suggest that the cyclic value of strain range or stress range could be used to correlate with TMF life since the fatigue life is the same for both phasings in this temperature range, and the cyclic quantities are also the same. However, for the temperature range 300 to 800 °C, the cyclic quantities of stress range and strain range are the same for both IP and OP TMF, but the resulting fatigue lives are very different. Thus, the magnitude of the maximum stress seems to affect TMF life when the minimum cycle temperature is lower, at 300 °C.

In this case, it is important to remember that the IP and OP loops occur in an anisothermal cycle, and thus the strength of the material when the maximum stress is applied is also different for the IP and OP cases. Figure 3.5b shows the stress history as a function of temperature for both thermal cycles and phasings. The arrows indicate the initial loading for each cycle that starts at the minimum temperature. By comparing the loops and loading path for both phasings, it becomes clear that the maximum stress in the IP TMF cycle occurs at 800 °C, when the strength is also low. In the OP TMF cycle, the maximum stress occurs at the minimum temperature when the strength of the material is high. Table 3.1 compares the maximum stress σ_{max} at the mid-life cycle with the fatigue strength coefficient σ'_f at the temperature of the maximum stress (see Table 2.3). The ratio of the maximum stress to the fatigue strength coefficient is nearly the same for the four TMF cases. Thus, although the maximum stress is higher in the OP TMF case, the proportion of maximum stress to the fatigue strength is the same for the TMF cases. Therefore, the magnitude of the maximum stress cannot be used to correlate with TMF life without consideration of the anisothermal cycle.

It should also be noted that the effect of the embrittlement has not yet been determined for the case of TMF loading. Based on the observations made in LCF tests conducted at 400 °C, it is expected that the embrittlement occurring at this temperature will also affect the TMF life and failure behavior. Fractographic examination of specimens tested in LCF at a range of temperatures showed that the embrittlement mechanism is active only when the temperature is near 400 °C. Correspondingly, a significant reduction in low cycle fatigue life was observed when the temperature was near 400 °C. A reduction in fatigue life is also seen in OP TMF when the thermal cycle is inclusive of 400 °C (minimum temperature of 300 or 400 °C). However, no reduction in fatigue life is observed under IP TMF loading for the same thermal cycle. Because the temperature for both TMF cases is inclusive of 400 °C, the embrittlement

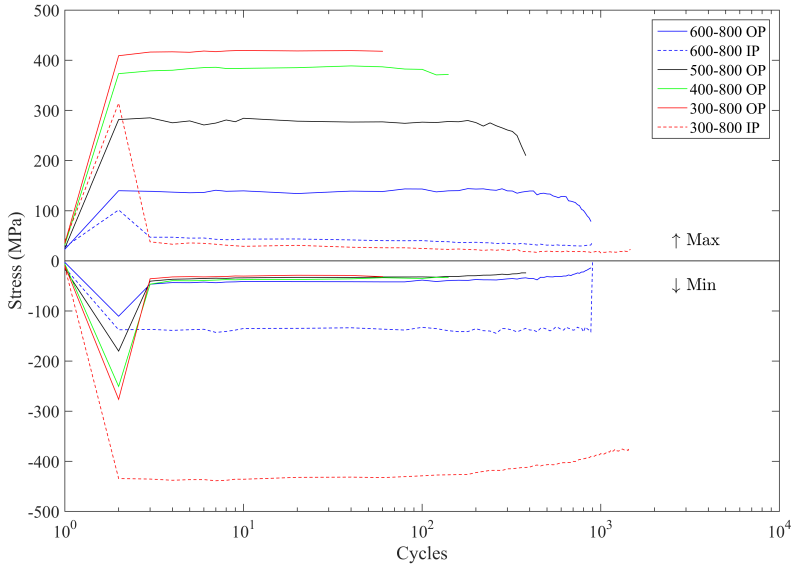

Figure 3.4: Evolution of the maximum and minimum stresses for OP and IP TMF tests conducted with a maximum temperature of 800 °C and minimum temperature of 300 or 600 °C.

mechanism should be *active* in both cases. However, it may not be equally *damaging* in both cases.

It is worthwhile in this case to examine the magnitude of the strains and stresses as they relate to the temperature of embrittlement, rather than the maximum temperature. Under IP TMF, a tensile mechanical strain is applied near 400 °C, and the stress is compressive. Under OP TMF, a compressive strain is applied near 400 °C and the stress is tensile. Thus, if the embrittlement mechanism is contributing to the lower fatigue life in OP TMF, the damage it contributes should be related to the state of stress or strain experienced at the embrittled temperature. Fractographic observations will be made in Section 3.4 to further examine the role of embrittlement in TMF damage for HiSiMo DCI.

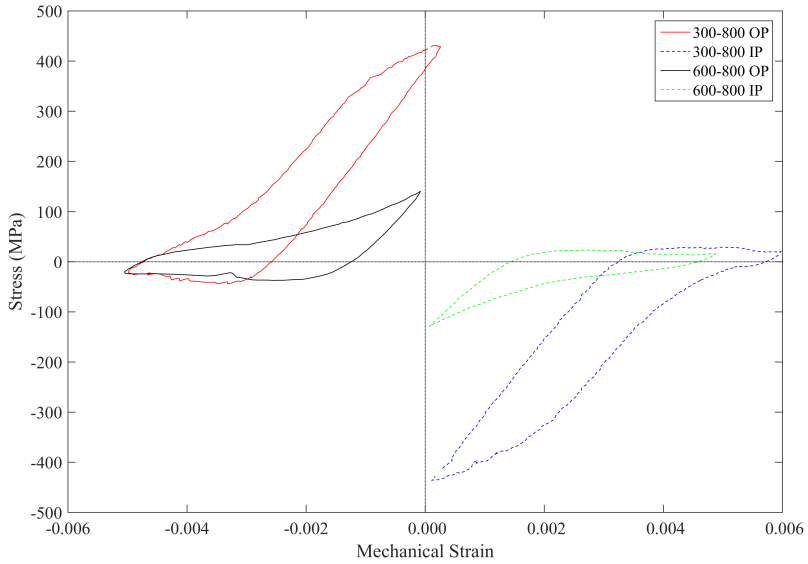

(a)

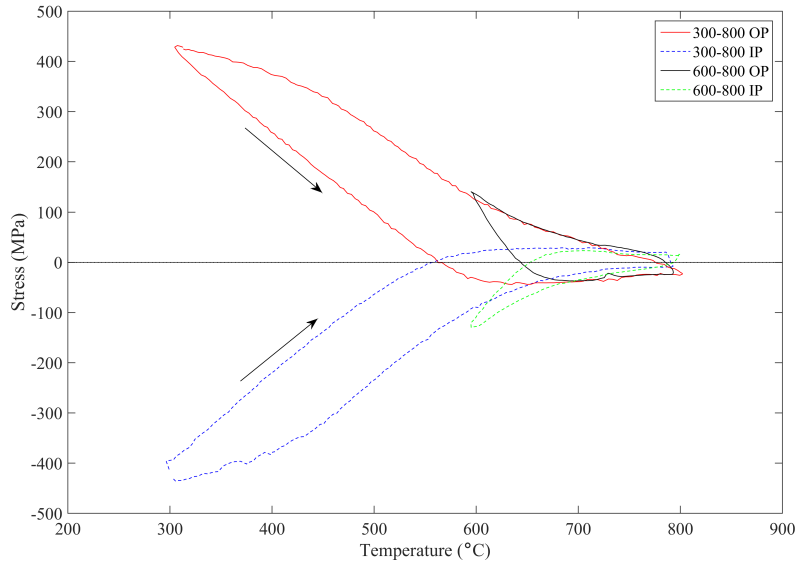

(b)

Figure 3.5: Stabilized loops of IP and OP TMF tests conducted for an applied strain of 0.005 for temperature ranges of 300 to 800 °C and 600 to 800 °C showing the (a) stress-strain hysteresis behavior and (b) stress history during the thermal cycle.

Table 3.1: Comparison of the maximum cyclic stress with the cyclic strength of the HiSiMo DCI at the maximum temperature of the thermal cycle.

Thermal Cycle	σ_{max}	σ'_f **at** T_{max}	σ_{max}/σ'_f
600-800 °C OP	140.7	266	0.53
600-800 °C IP	23.4	51	0.46
300-800 °C OP	431.5	862	0.50
300-800 °C IP	29.1	51	0.57

3.3.2 Effect of Reducing Maximum Cycle Temperature

TMF tests were additionally conducted with the maximum temperature of the thermal cycle reduced by 10 % from 800 °C to 720 °C to investigate the effect on TMF life of varying proportions of high temperature damage mechanisms, including creep and oxidation. Figure 3.6 shows the strain-life curve for tests conducted under both OP and IP TMF conditions when the maximum temperature is 720 or 800 °C. The minimum temperature was either 600 or 300 °C. Examining the OP TMF curves in Figure 3.6, it is clear that reducing the maximum temperature of the thermal cycle does not affect the OP TMF life. The IP TMF life is not changed by reducing the maximum temperature when the minimum temperature is 600 °C. However, when the minimum temperature is 300 °C, a significant improvement in IP TMF life is seen by reducing the maximum temperature.

The HiSiMo DCI was found to be cyclically stable under TMF loading when the maximum temperature was 720 °C, as shown in Figure 3.7. The mid-life hysteresis loops were examined to understand differences in the stress-strain response that could explain the improvement seen in the IP TMF life, and the similarity of OP TMF life when the maximum cycle temperature was reduced. Figure 3.8 shows both OP and IP stress-strain loops for thermal cycles of 300 to 720 °C, 300 to 800 °C, 600 to 720 °C and 600 to 800 °C. The stress range and area of the loops are similar whether the maximum temperature is 720 or 800 °C. There is also no difference in the loops

when comparing the IP and OP cases for the different temperature ranges. The cyclic quantities of strain range and stress range are then similar for either maximum temperature and for both phasings, and the difference in IP TMF life cannot be explained by differences in the cyclic quantities.

Recall that TMF loops occur in an anisothermal cycle, and that the maximum stress occurs at the maximum temperature for IP TMF. In this case, when the same stress is experienced, as shown in the stress-strain loop, a lower temperature is present. The strength of the material is higher due to the lower temperature, and the stress is less damaging. This explanation for the improvement in life is consistent with the observations of the 300 to 800 °C IP TMF tests. However, no change in IP TMF life occurs when the minimum temperature is 800 °C. It is necessary in this case to perform fractography of the tested specimens to understand the differences in the failure modes that might lead to a different influence of the thermal cycle on life.

In the case of the OP TMF, the maximum temperature coincides with a compressive stress. For a minimum temperature of 600 or 300 °C, there is no difference in OP TMF life by reducing the maximum temperature, which suggests that the damage due to a compressive stress is fairly insensitive to temperature for this range. This may be due to the much higher strength that HiSiMo DCI should exhibit in compression than in tension (*Ductile Iron Society*, 1998). Fractography is necessary to confirm the dominant mechanisms which cause failure in OP TMF for various thermal cycles.

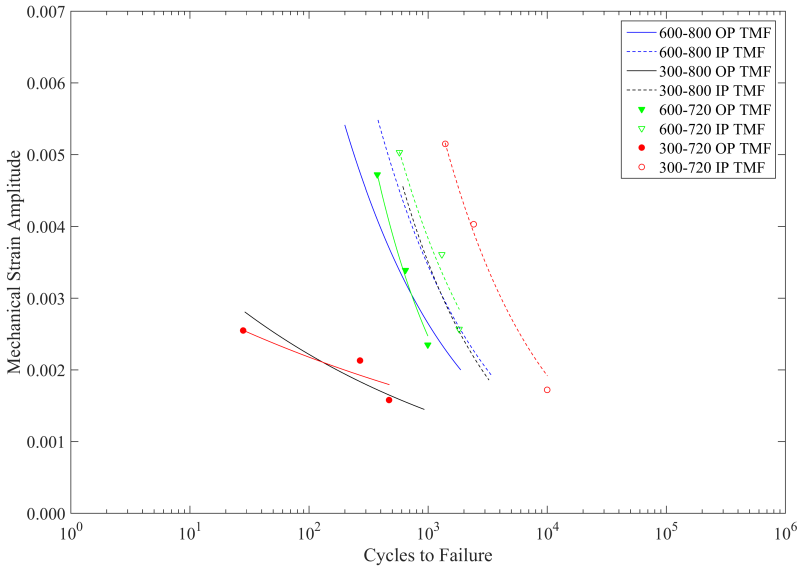

Figure 3.6: TMF life as a function of mechanical strain amplitude for different thermal cycles in in-phase (IP) and out-of-phase (OP) loading.

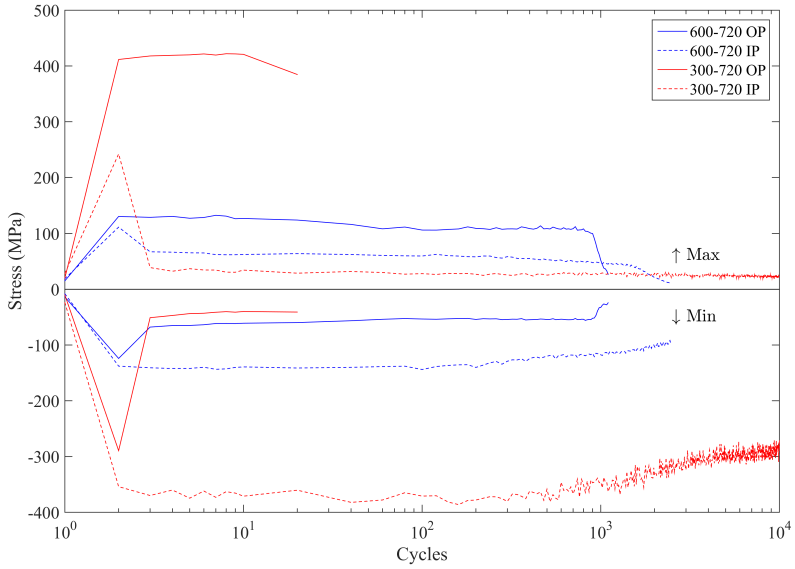

Figure 3.7: Evolution of the maximum and minimum stresses for OP and IP TMF tests conducted with a maximum temperature of 720 °C and minimum temperature of 300 or 600 °C.

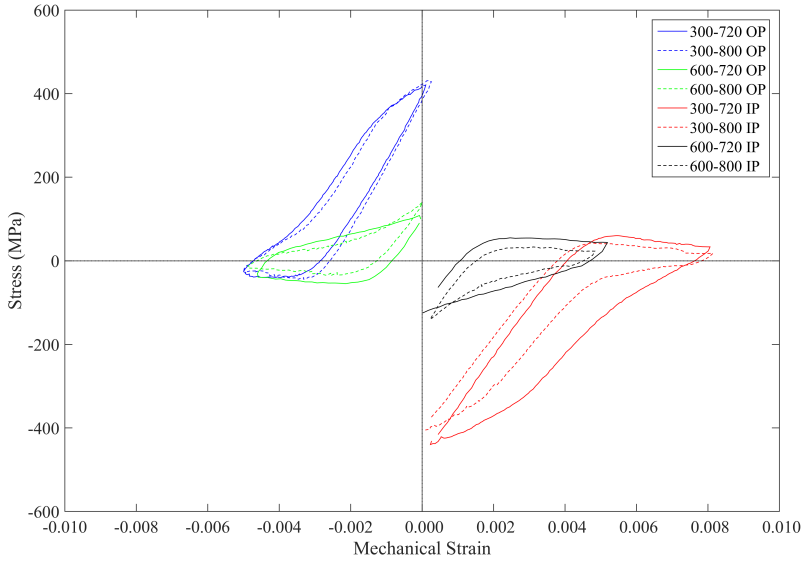

Figure 3.8: Comparison of the stress-strain response under OP and IP TMF for tests conducted with minimum cycle temperatures of 300 or 600 °C, and maximum cycle temperatures of 720 (solid lines) or 800 °C (dashed lines).

3.3.3 Effect of a Strain Hold at the Maximum Temperature

Finally, a limited number of tests were conducted in OP TMF with a strain hold at the maximum temperature to simulate the sustained high-temperature operation of the engine. In general, a strain hold could increase damage and result in shorter life by introducing additional damage due to creep. The duration of the hold was either 60 s or 600 s, and the maximum temperature was 720 or 800 °C. The strain-life data are shown in Figure 3.9 along with the fitted curve for OP TMF without a hold for the temperature ranges 300 to 800 °C to allow comparison of the fatigue lives. However, there is no remarkable difference in fatigue life between tests with and without a hold, regardless of the maximum temperature. Both hold durations resulted in similar TMF life.

Stress relaxation did occur during the hold time. Figure 3.10 shows the stress history over the stabilized TMF cycle. The inset in Figure 3.10 shows a magnified view of the hold period. At both maximum temperatures, the small compressive

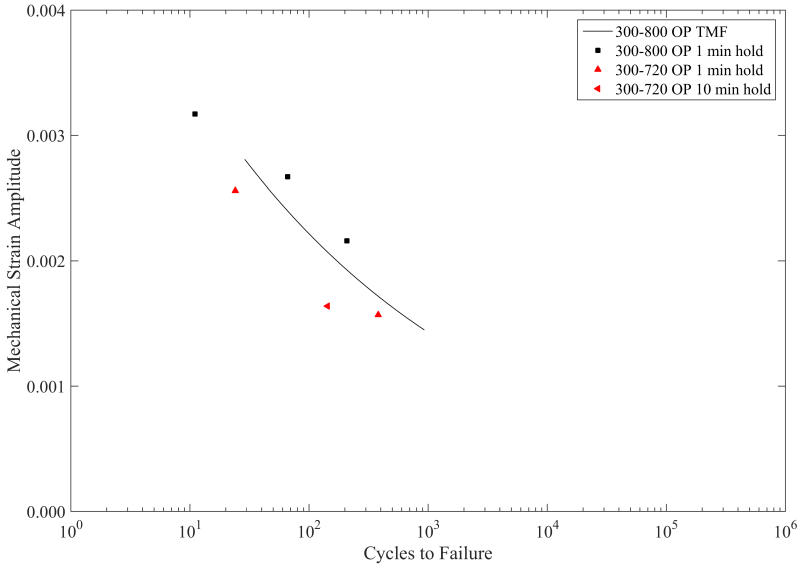

Figure 3.9: TMF life for specimens tested under OP conditions with a strain hold at the maximum cycle temperature. The curves show the trend of the OP TMF data *without* a hold at 300 to 800 °C for reference.

stress relaxes slightly. The extent of relaxation does not change for the two durations of hold considered in this study. Furthermore, because the compressive stress is small in this case, no change is measurable in the mean stress over the duration of the test due to the addition of a hold time. Figure 3.11 shows the evolution of the maximum and minimum stresses for specimens tested at a strain amplitude of about 0.002.

Thus, the addition of a strain hold at the maximum temperature of the OP TMF cycle did not introduce additional damage that reduced the fatigue life.

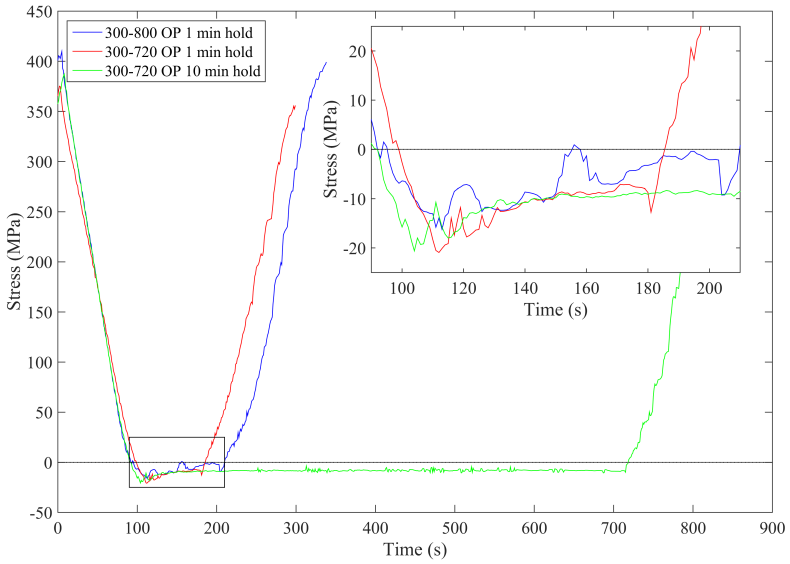

Figure 3.10: Stabilized stress-strain loops for OP TMF tests conducted with a maximum temperature of 720 or 800 °C with a strain hold of 60s or 600s at the maximum temperature.

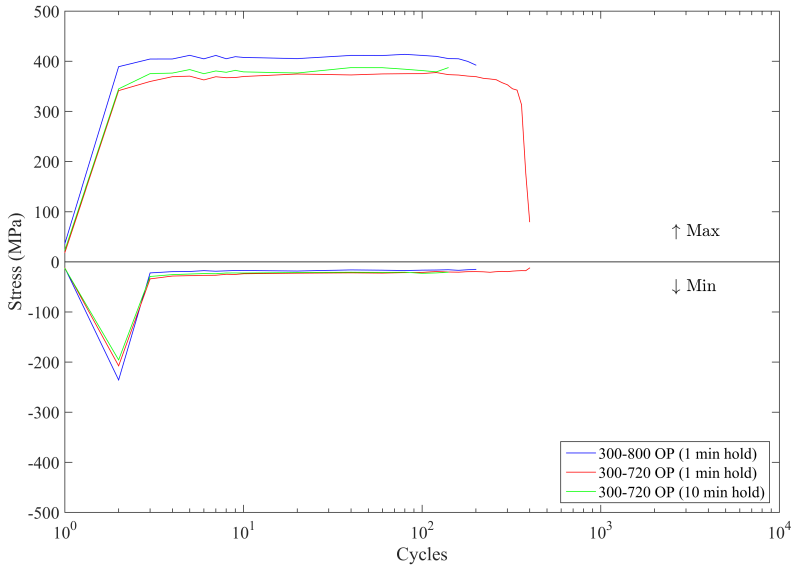

Figure 3.11: Evolution of the maximum and minimum stresses for OP TMF tests conducted with a strain hold at the maximum temperature of 720 or 800 °C, and a minimum temperature of 300 °C.

3.4 Examination of Damage Mechanisms

TMF is a complex process that involves the interaction of fatigue, oxidation and creep. In addition, HiSiMo DCI undergoes a severe embrittlement at 400 °C which has shown to affect the OP TMF, but not the IP TMF life. In general, each damage mechanisms is temperature-dependent and it is not possible to know *a priori* which mechanisms are predominant in an anisothermal cycle. An investigation of the damage mechanisms was conducted to identify the key attributes of failure as the temperature limits and phasing of the TMF cycle change. Examined specimens were tested under various thermal cycles, and at both high and low strain ranges in order to gain a comprehensive understanding of the damage modes active in TMF.

3.4.1 IP TMF

For specimens tested in IP TMF, fracture tended to initiate around the surface of the specimen due to cracks in the oxide layer. Figure 3.12 shows optical microscope images of the surfaces of specimens tested with a maximum temperature of 720 or 800 °C, and a minimum temperature of 300 or 600 °C. The difference in thermal expansion between the oxide layer and the substrate leads to the ribbon-like fracture of the oxide. A lower minimum temperature results in a greater extent of oxide fracture due to the greater difference in thermal strain between the oxide and the substrate, as shown in Figure 3.12a and Figure 3.12c.

Figure 3.13 shows optical microscope images of the fracture surfaces obtained in IP TMF for various thermal cycles which are noted in the individual images. The white dashed lines separate the regions of TMF fracture and final tensile fracture. The flat regions of oxide intrusion where the TMF cracks initiate are evident at the circumference of the fracture surfaces. SEM images of these regions in Figure 3.14 to Figure 3.17 show that thick oxide layer is present which obscures the features of the fracture surface. Despite the broad regions around the specimen surface where the

oxide intrusion nucleates the TMF cracks, failure tends to be dominated by a primary crack.

Longitudinal cross-sections of specimens tested under IP TMF in Figure 3.18 show that oxide intrusion occurs in a transgranular fashion, regardless of the temperature range. The oxide intrusion is fairly narrow, which indicates that when the oxide layer fractures, it does not additionally detach from the substrate. Instead, fresh metal is exposed at the tip of the crack, and this subsequently re-oxidizes. Once the new oxide layer reaches a critical thickness, it fractures again, resulting in a deeper and deeper penetration of the oxide into the substrate. The TMF crack propagates predominantly by the mechanism of oxide intrusion. After the crack front passes, the oxide additionally penetrates the fracture surface, creating a rough profile of the substrate underneath the oxide layer. Based on the penetration of the oxide layer into the fracture surface, the rate of oxidation along the grain boundaries is not significantly faster than the rate of oxidation of the bulk material; this results in a oxidation front that progresses fairly uniformly into the fracture surface.

When the maximum temperature of the IP TMF cycle is 800 °C, decarburization occurs in the graphite nodules which results in an irregular appearance of the graphite nodules in the cross-section. Additionally, grain boundary fracture due to creep deformation is evident in the bulk material when the maximum temperature is 800 °C. However, the intergranular damage appears to be more important to the crack growth process once the TMF crack has already propagated over a significant distance.

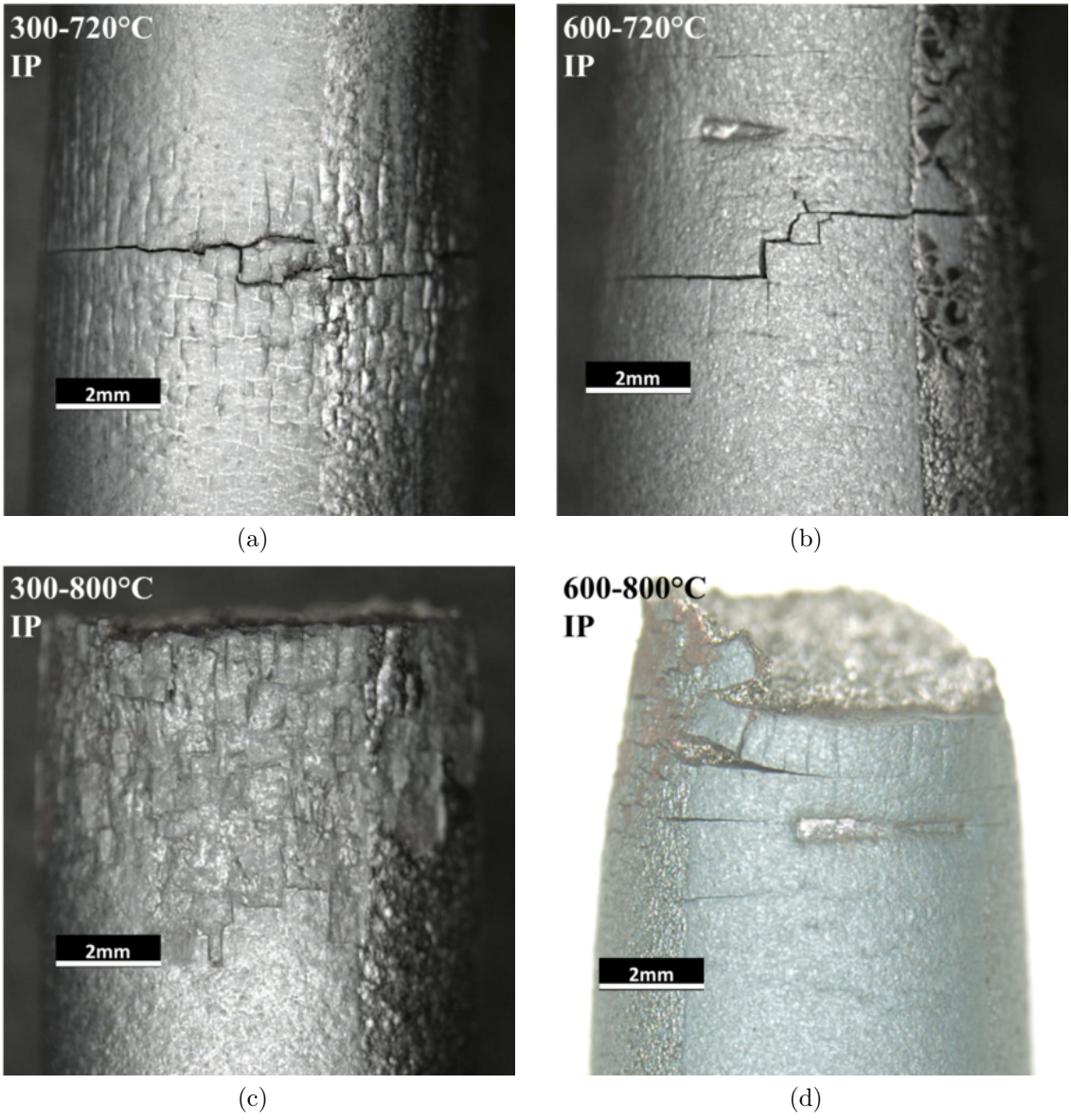

Figure 3.12: Optical microscope images showing the fracture of the surface oxide in specimens tested under IP TMF for the temperature ranges (a) 300 to 720 °C, (b) 600 to 720 °C, (c) 300 to 800 °C, and (d) 600 to 800 °C.

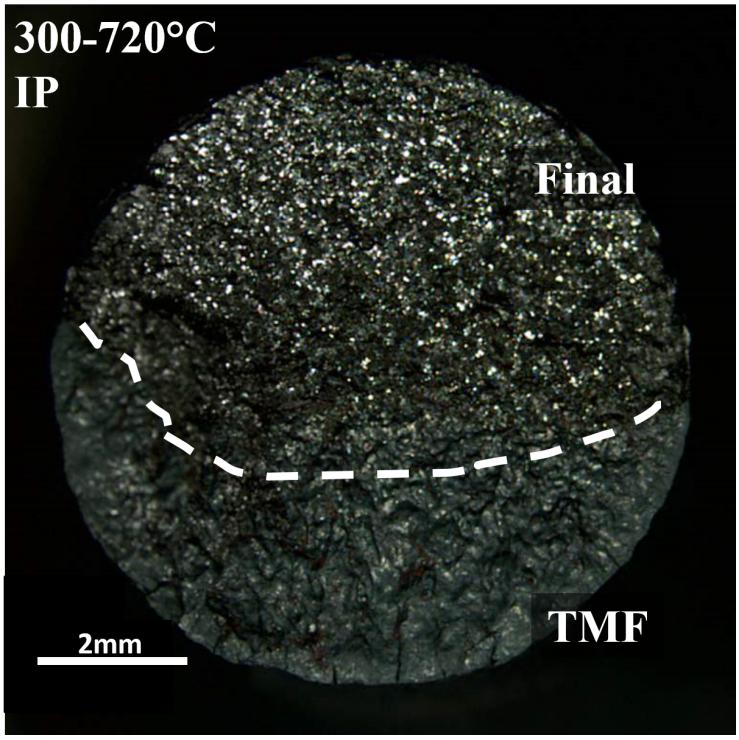

(a)

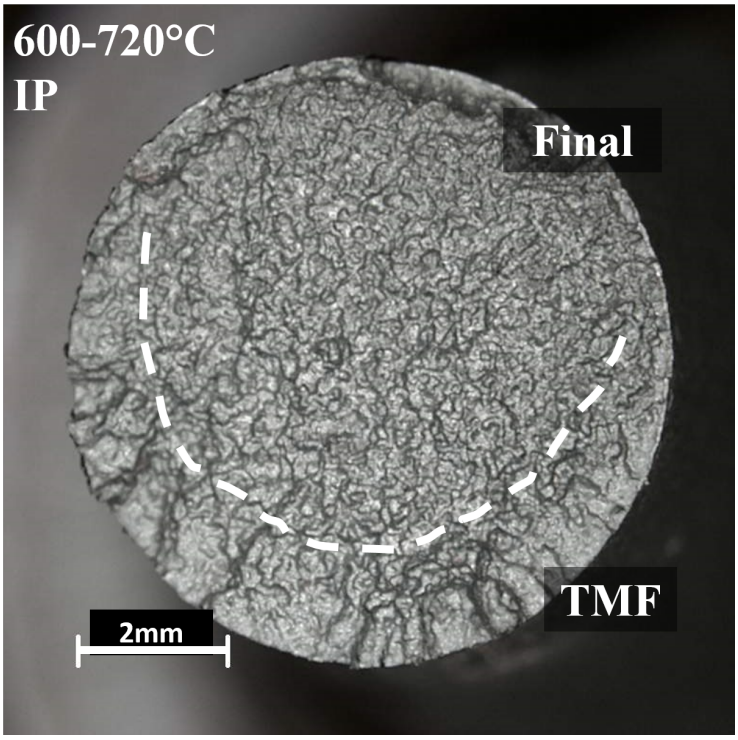

(b)

Figure 3.13: Optical microscope images of the fracture surfaces of specimens tested under IP TMF for the temperature ranges (a) 300 to 720 °C and (b) 600 to 720 °C. Continued on next page, (c) 300 to 800 °C, and (d) 600 to 800 °C.

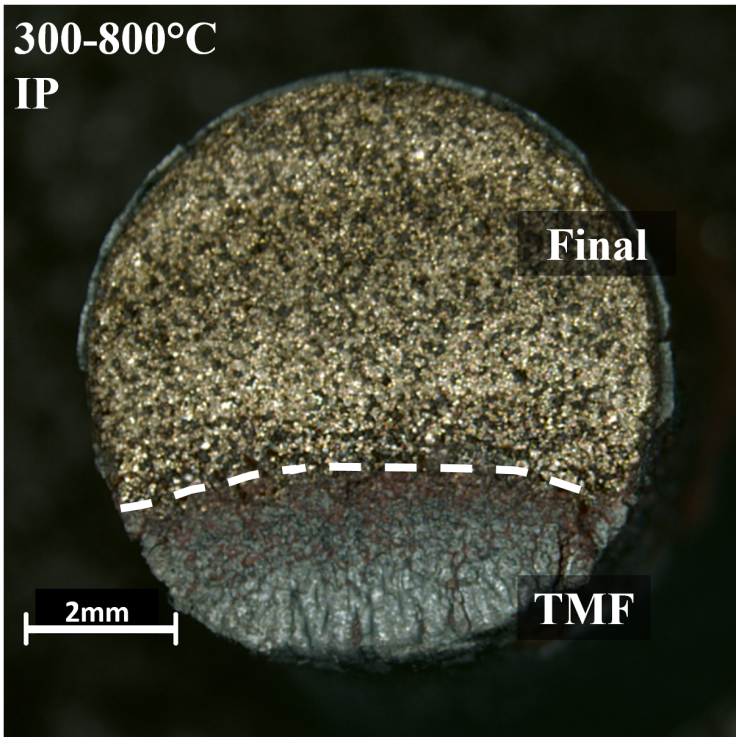

(c)

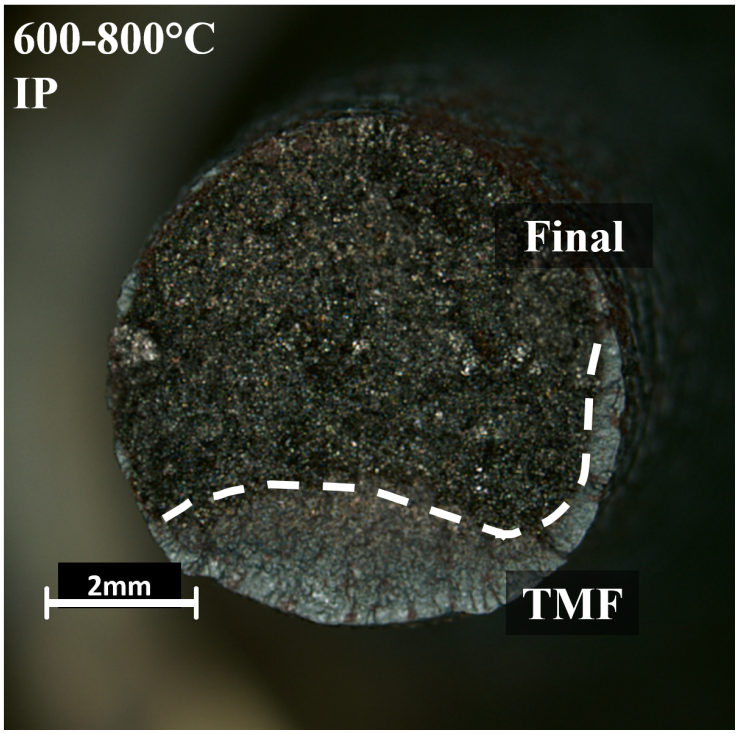

(d)

Figure 3.13: Continued from previous page.

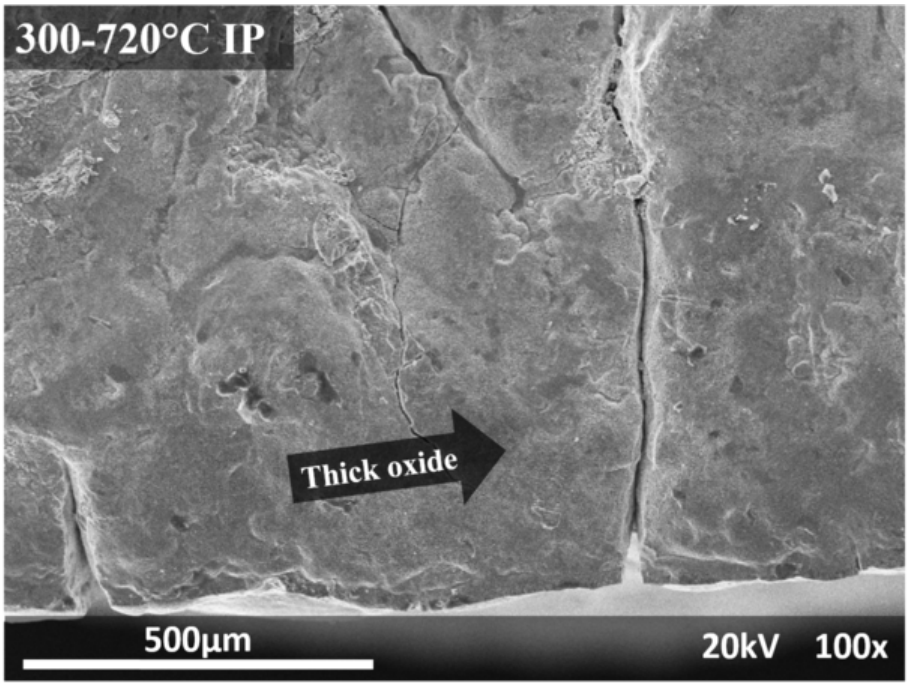

Figure 3.14: SEM images of the fracture surface in the region of TMF crack growth by oxide intrusion for specimens tested in IP TMF for 300 to 720 °C.

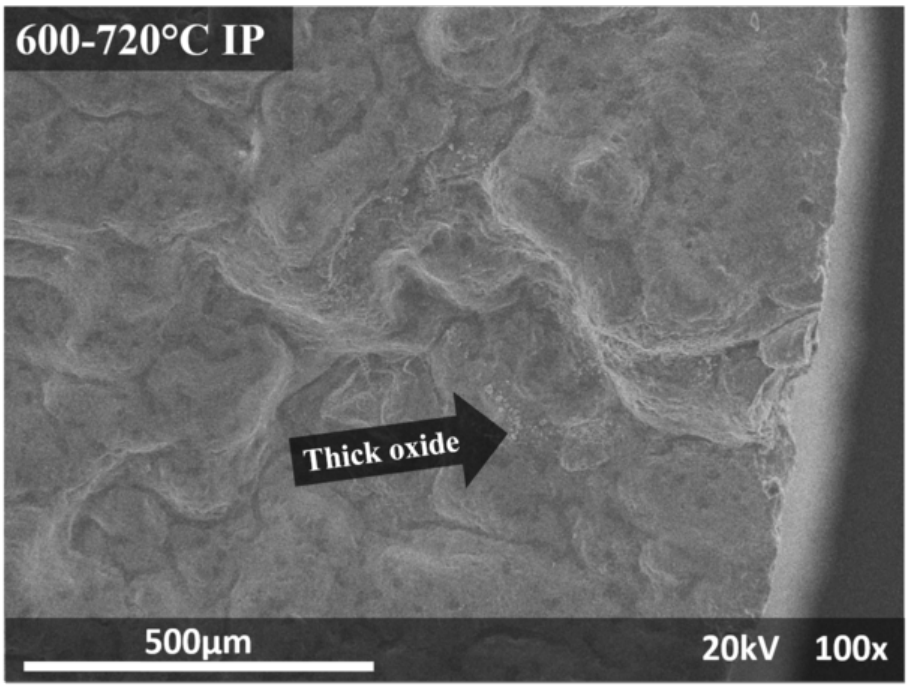

Figure 3.15: SEM images of the fracture surface in the region of TMF crack growth by oxide intrusion for specimens tested in IP TMF for temperature ranges of 600 to 720 °C.

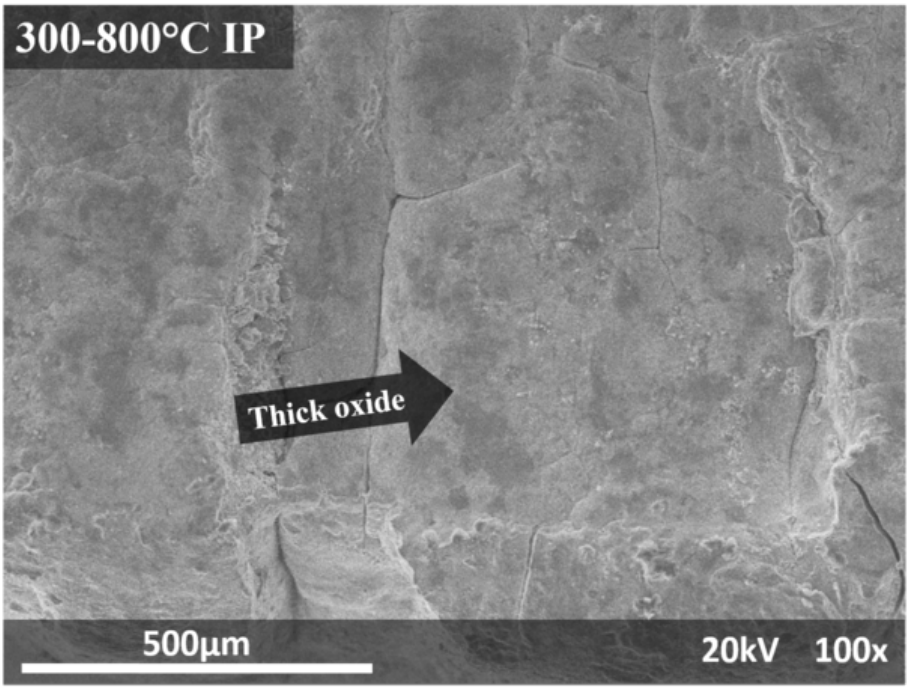

Figure 3.16: SEM images of the fracture surface in the region of TMF crack growth by oxide intrusion for specimens tested in IP TMF for 300 to 800 °C.

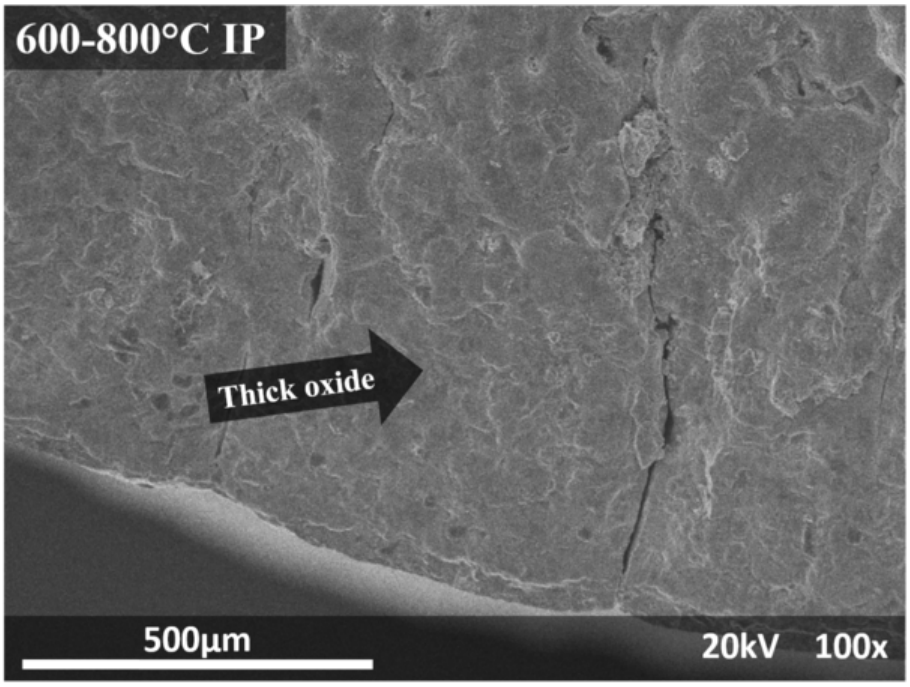

Figure 3.17: SEM images of the fracture surface in the region of TMF crack growth by oxide intrusion for specimens tested in IP TMF for 600 to 800 °C.

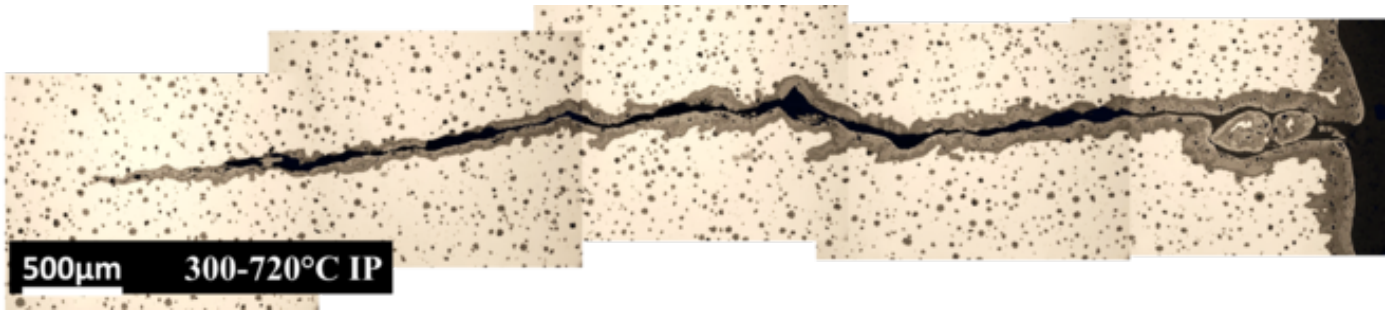

(a)

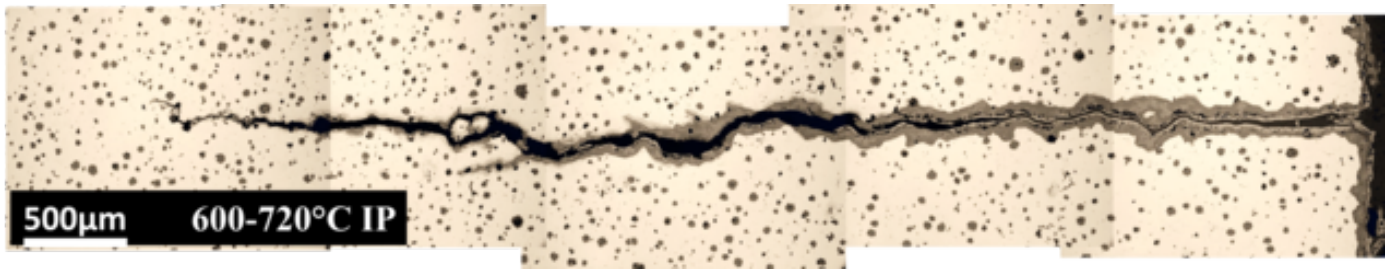

(b)

Figure 3.18: Optical microscope images of the longitudinal cross-section in specimens tested in IP TMF for temperature ranges of (a) 300 to 720 °C and (b) 600 to 720 °C. Continued on next page, (c) 300 to 800 °C, and (d) 600 to 800 °C.

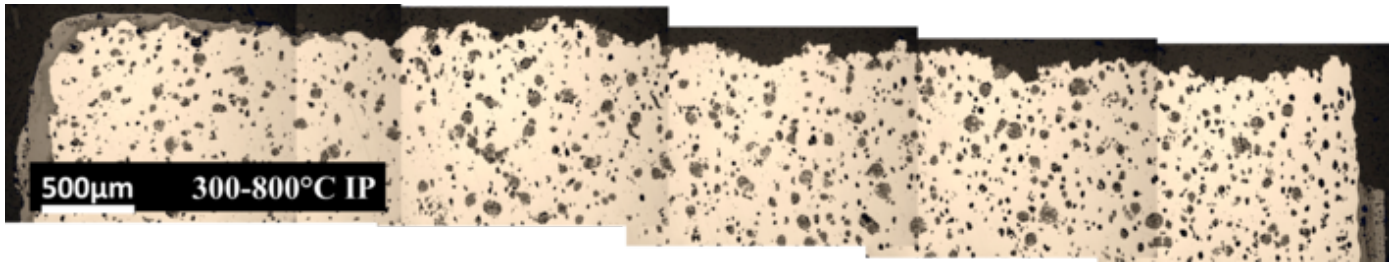

(c)

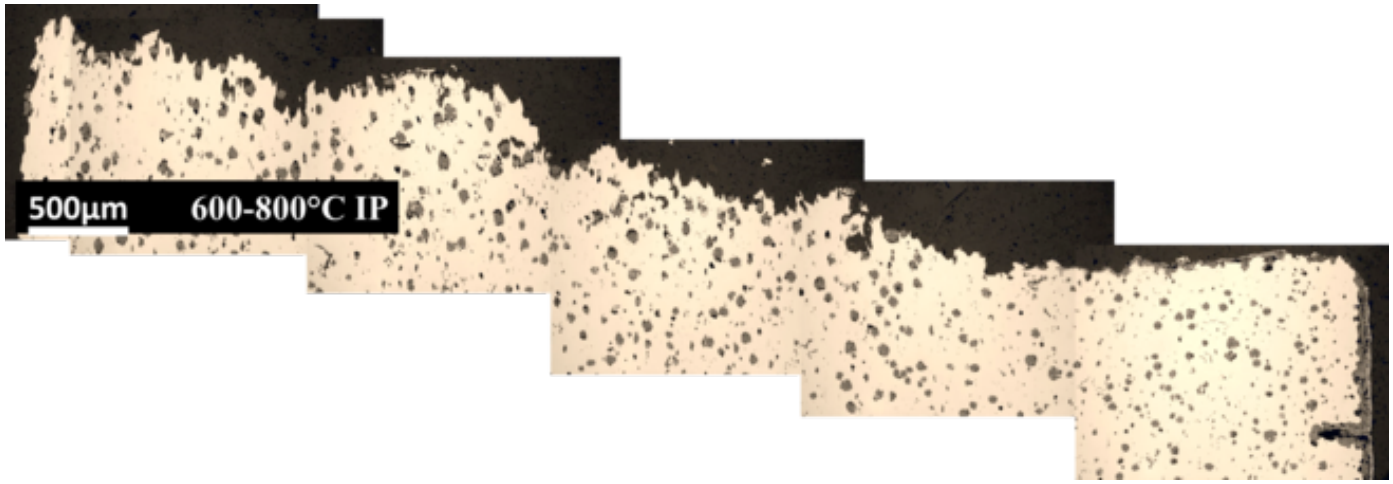

(d)

Figure 3.18: Continued from previous page.

3.4.2 OP TMF

As in the case of IP TMF, OP TMF cracks initiate due to the fracture of a surface oxide which subsequently penetrates the substrate. end to initiate due to fracture of the oxide which grows into the metal substrate. Figure 3.19 shows the surface of specimens tested in OP TMF under various thermal cycles. Many small cracks are present in the oxide layer. When the minimum temperature is 600 °C, the oxide fractures in a ribbon-like pattern, similar to the IP TMF case. However, when the minimum temperature is 300 °C, the fracture of the oxide layer has a more irregular pattern.

The fracture surfaces are examined under optical microscope in Figure 3.20. The white dashed lines separate the regions of tensile fracture from those of TMF fracture. A flat area at the circumference of the fracture surface related to the oxide intrusion is readily evident in specimens where the minimum temperature is 600 °C. Additionally, the depth of the oxide intrusion is greater when the maximum temperature is 800 °C than when it is 720 °C, for either minimum temperature.

When the minimum temperature is 600 °C, the fracture surface is covered with a thick oxide that obscures the features, as seen in Figure 3.22 and Figure 3.24 for maximum temperatures of 720 and 800 °C, respectively. In this case, the predominant mode of TMF crack propagation can be determined from examination of the longitudinal cross-sections in Figure 3.25b and Figure 3.25d, respectively, for the same specimens examined under SEM. From the longitudinal sections, it is evident that the fatigue crack propagates in a transgranular manner for a short distance at the location of an oxide intrusion. As the fatigue crack propagates, failure occurs by mixed transgranular and intergranular fracture.

Similarly, when the minimum temperature is 300 °C, for either maximum temperature, failure occurs predominantly by a mix of transgranular and intergranular fracture as shown in Figure 3.21a and Figure 3.23a. However, intergranular facets, as

seen in Figure 3.21b and Figure 3.23b are far more prevalent on the fracture surfaces for the lower minimum temperature. Chemical analysis performed on the fracture surfaces with EDS shows the presence of small quantities of magnesium for all thermal cycles, confirming the presence of grain boundaries at the fracture surface. In specimens tested with a minimum temperature of 300 °C, the content of magnesium is much higher, which indicates that grain boundary fracture was more extensive for the lower minimum temperature. Examination of the longitudinal cross-sections for a minimum temperature of 300 °C in Figure 3.25a and Figure 3.25c reveals that the fatigue crack initiates at the location of an oxide intrusion. However, when compared to the higher minimum temperature, the extent of oxidation on the fracture surface is far less extensive.

A high content of magnesium on the fracture surface, along with pearlite-promoting elements, is consistent with the fracture surface that was observed in isothermal LCF due to damage caused by 400 °C embrittlement. The content of magnesium at the fracture surface is high when the thermal cycle includes 400 °C, which indicates the embrittlement mechanism was damaging in this case, and contributed to the growth of the TMF crack.

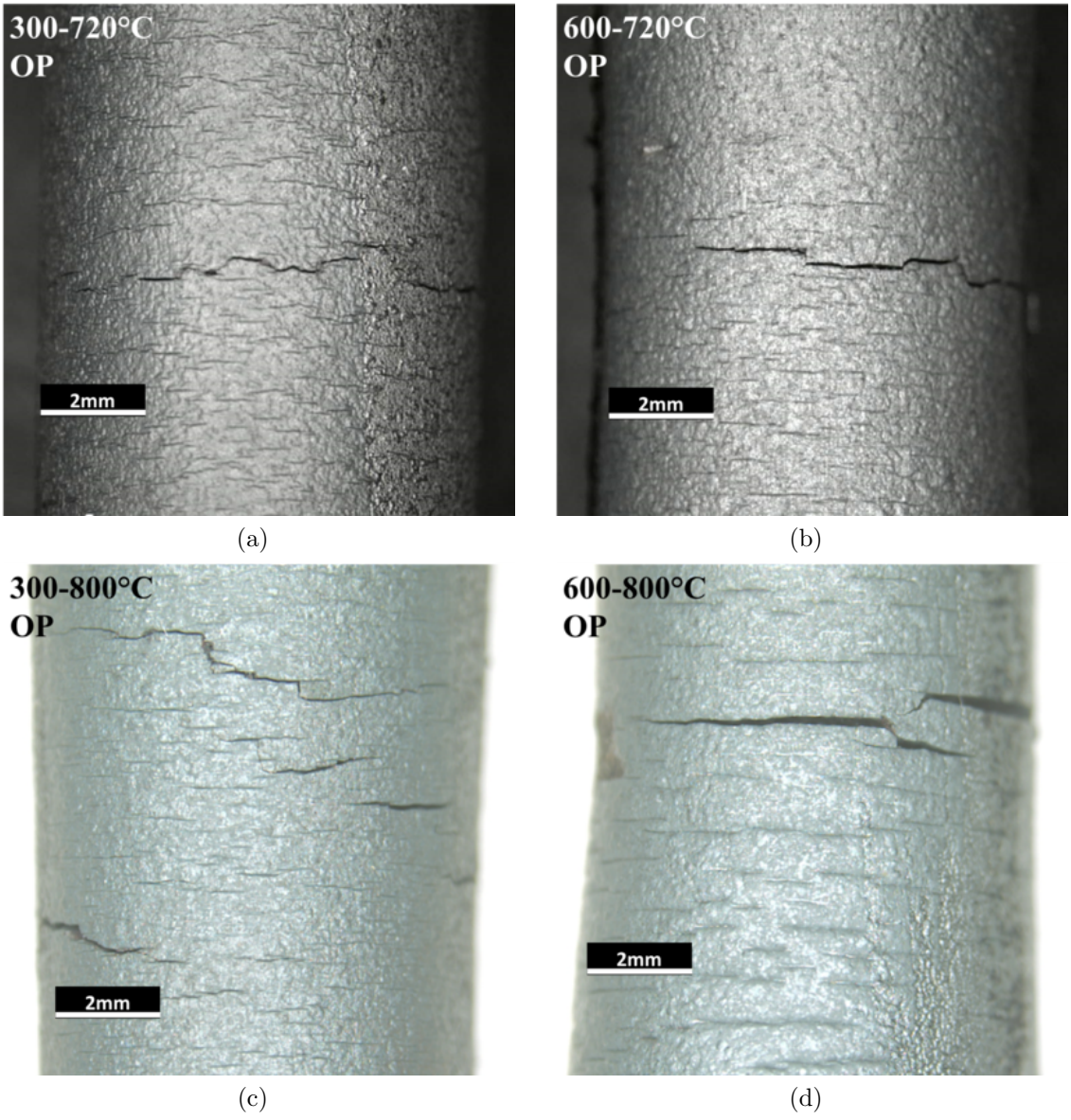

Figure 3.19: Optical microscope images showing the fracture of the surface oxide in specimens tested under OP TMF for the temperature ranges (a) 300 to 720 °C, (b) 600 to 720 °C, (c) 300 to 800 °C, and (d) 600 to 800 °C.

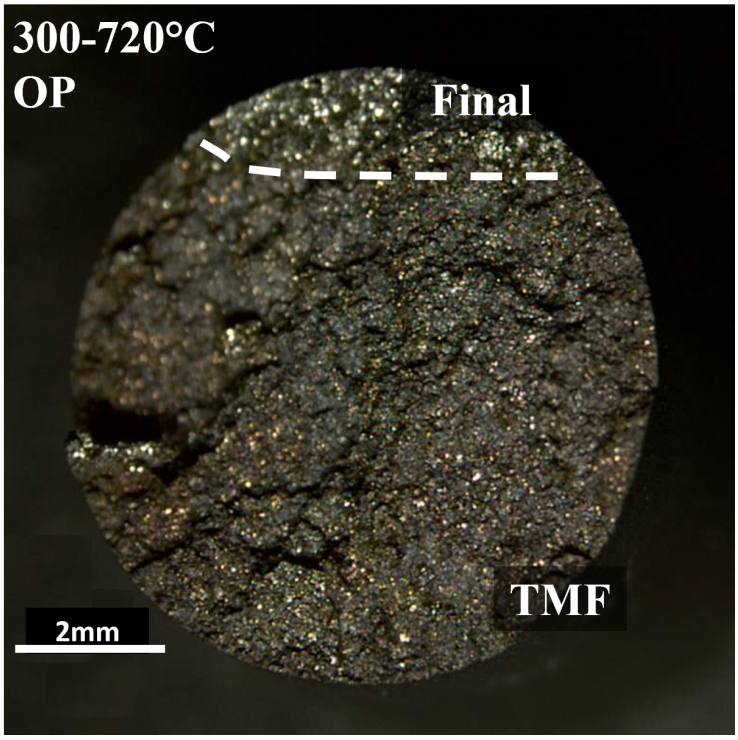

(a)

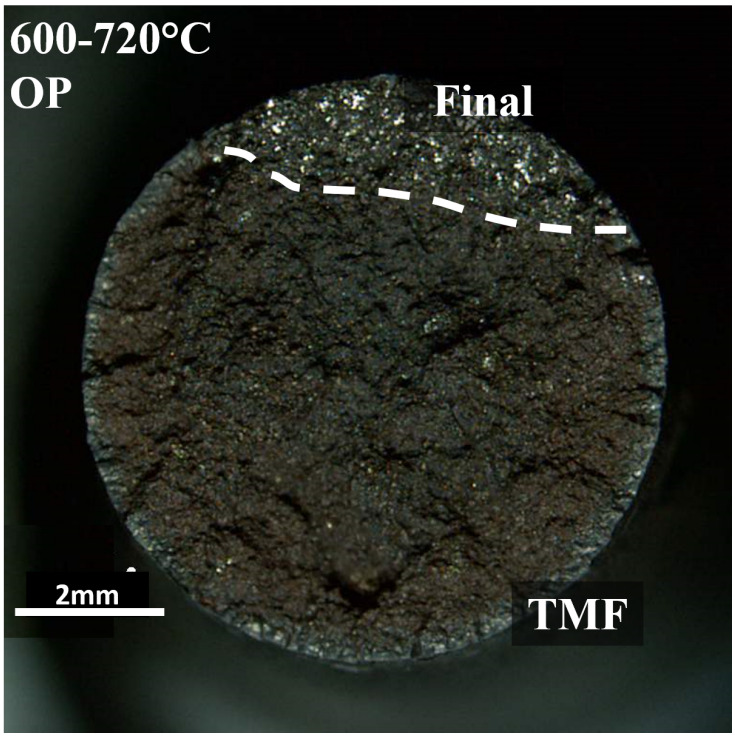

(b)

Figure 3.20: Optical microscope images of the fracture surfaces of specimens tested under OP TMF for the temperature ranges (a) 300 to 720 °C and (b) 600 to 720 °C. Continued on next page, (c) 300 to 800 °C, and (d) 600 to 800 °C.

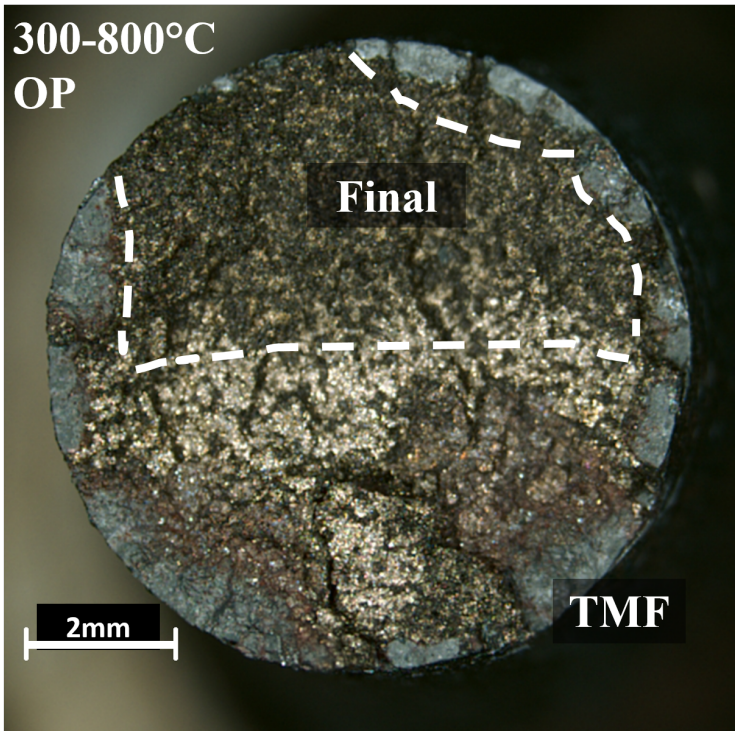

(c)

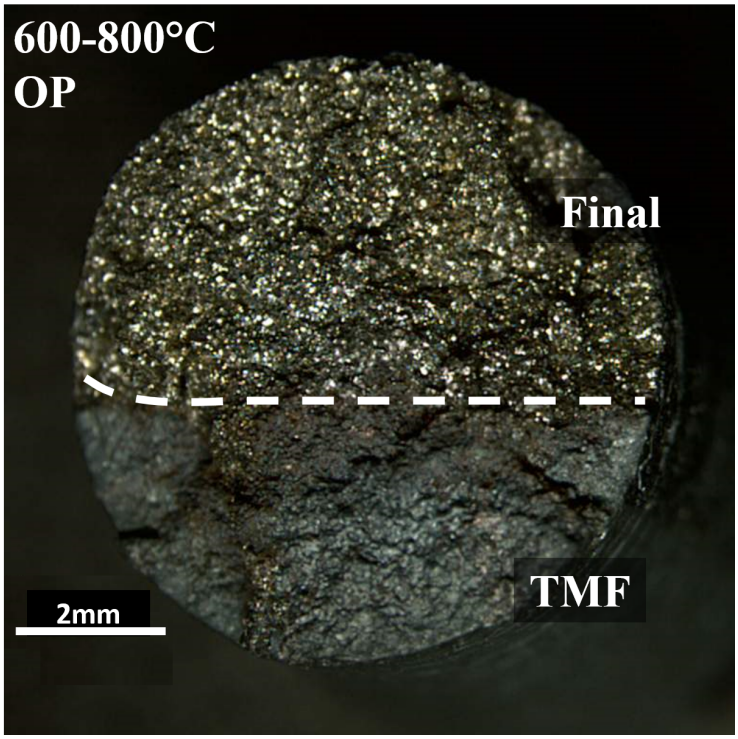

(d)

Figure 3.20: Continued from previous page.

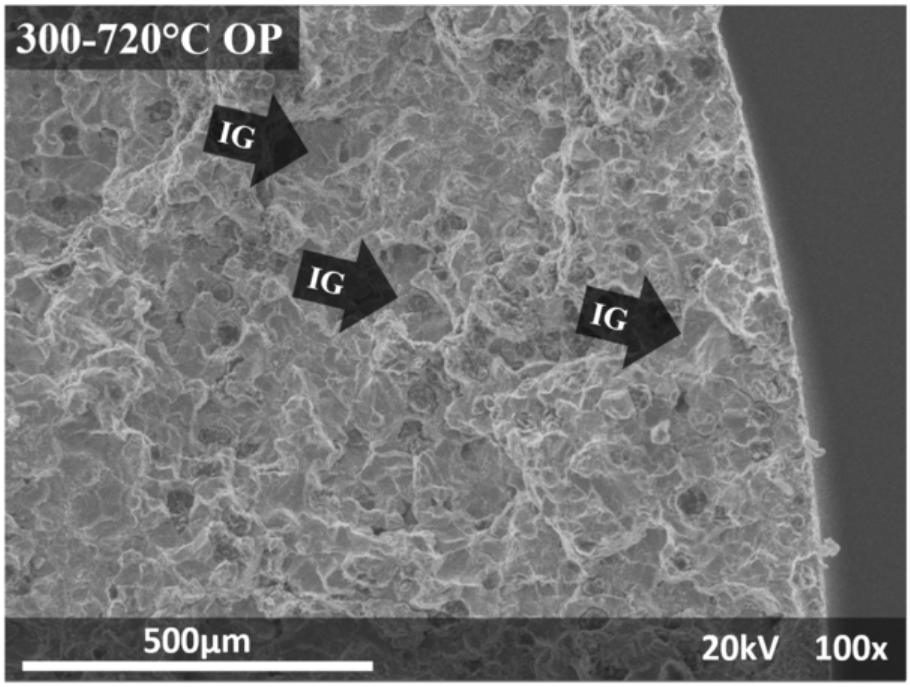

(a)

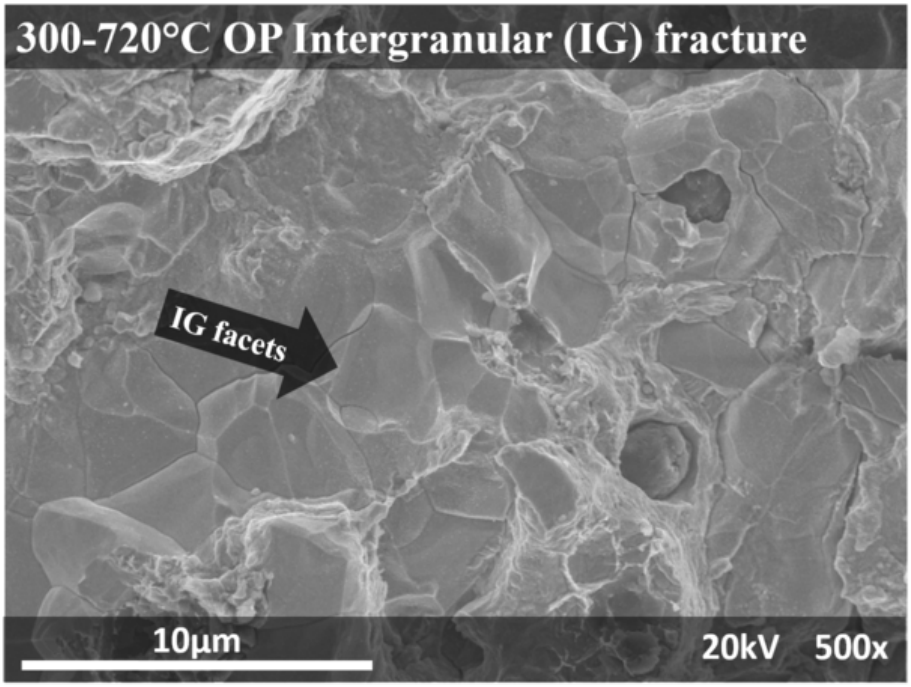

(b)

Figure 3.21: SEM images of (a) the fracture surface in the region of TMF crack initiation for a specimen tested in OP TMF at 300 to 720 °C and (b) intergranular fracture.

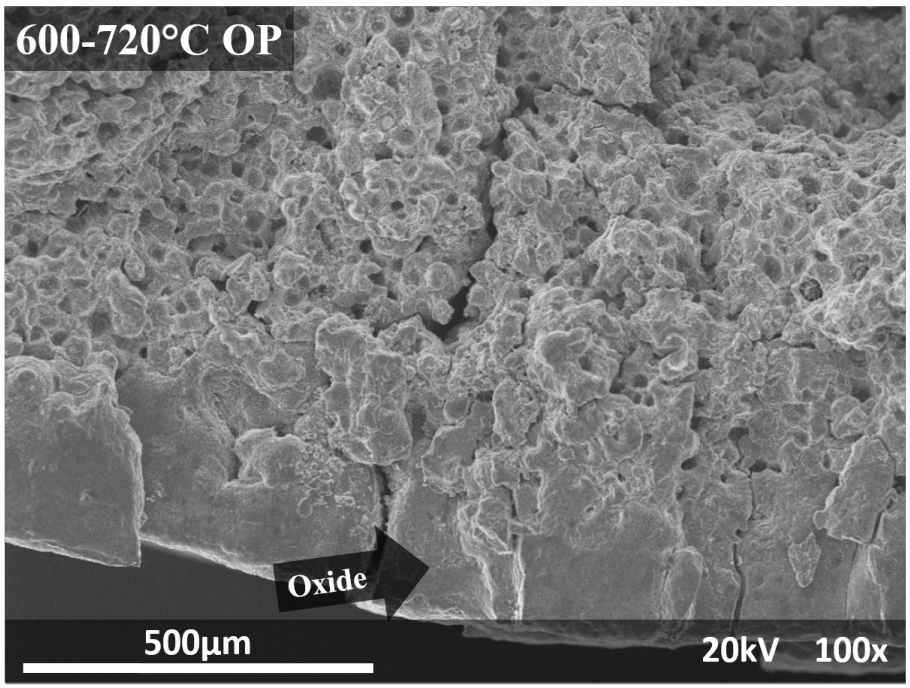

Figure 3.22: SEM image of the fracture surface in the region of TMF crack initiation for a specimen tested in OP TMF at 600 to 720 °C.

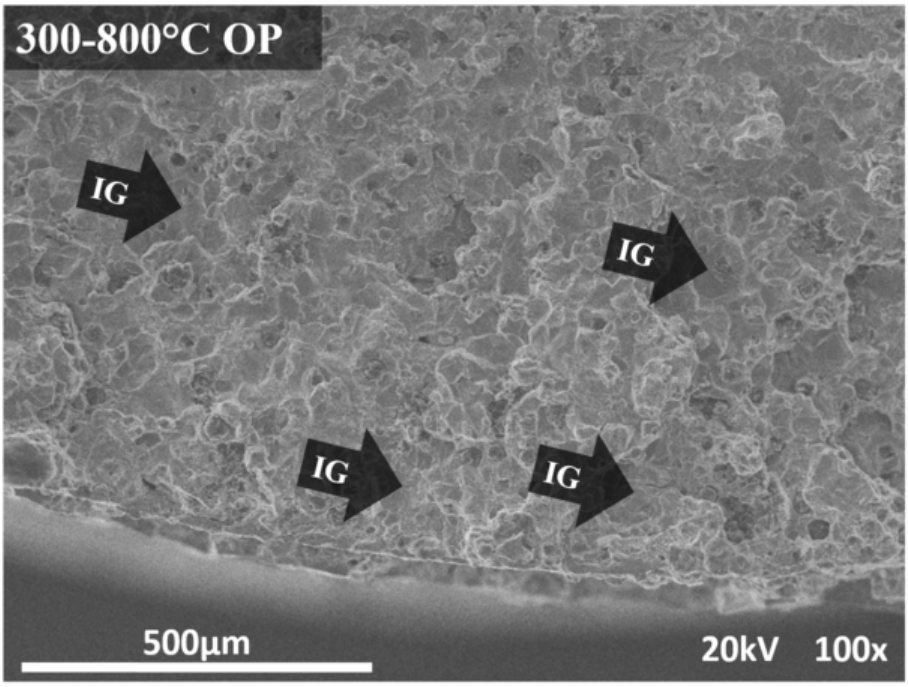

(a)

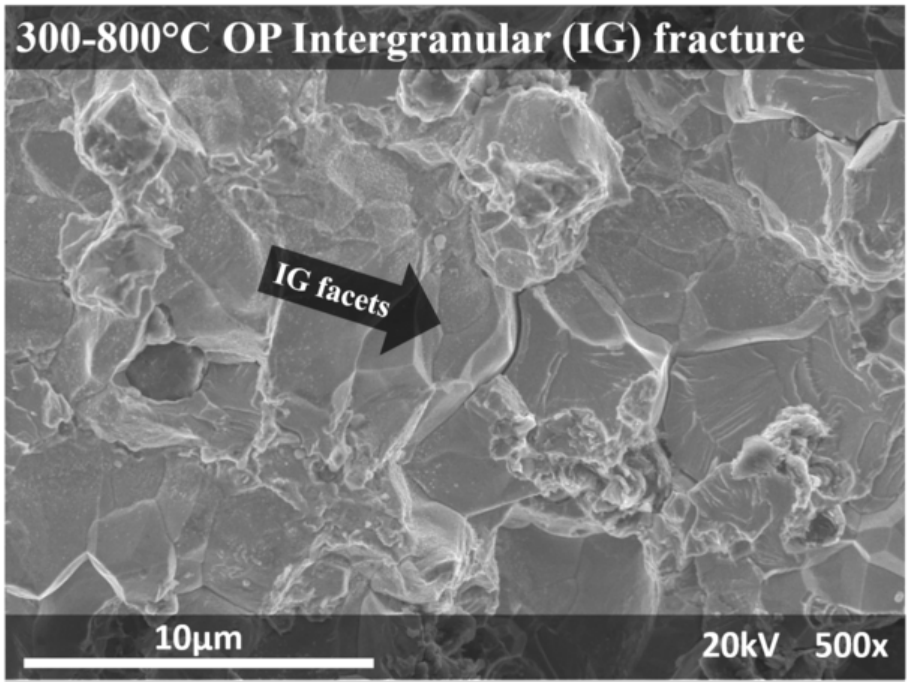

(b)

Figure 3.23: SEM images of (a) the fracture surface in the region of TMF crack initiation for a specimen tested in OP TMF at 300 to 800 °C and (b) intergranular fracture.

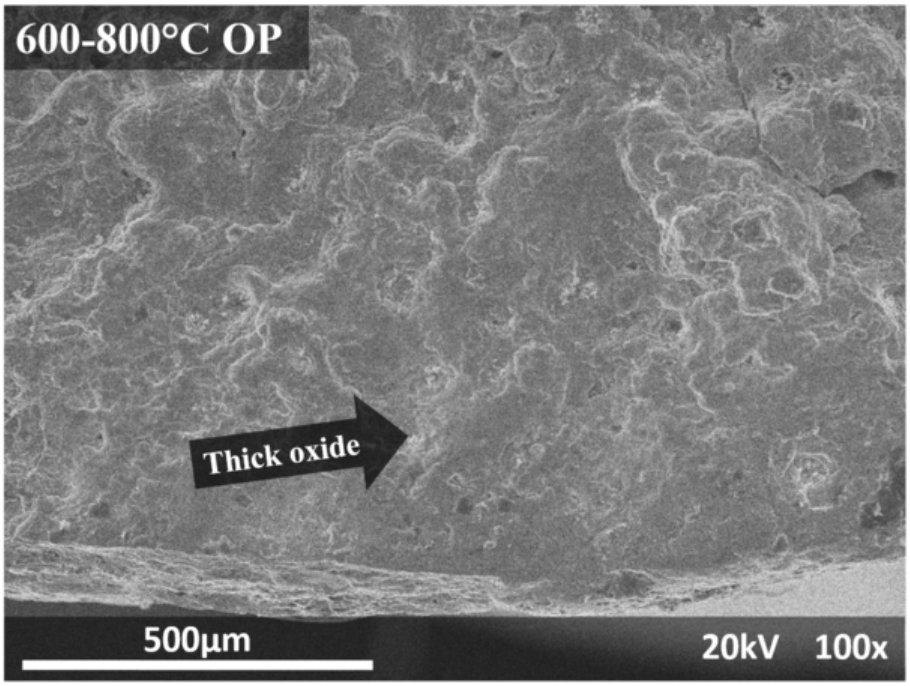

Figure 3.24: SEM image of the fracture surface in the region of TMF crack initiation for a specimen tested in OP TMF at 600 to 800 °C.

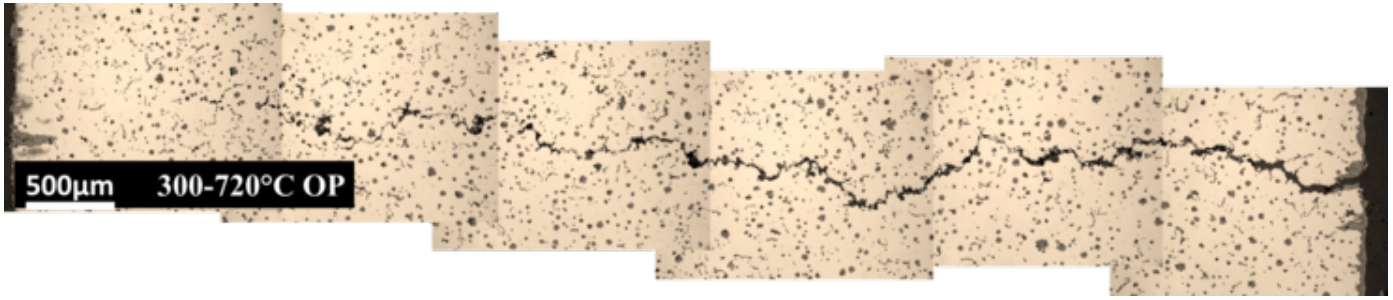

(a)

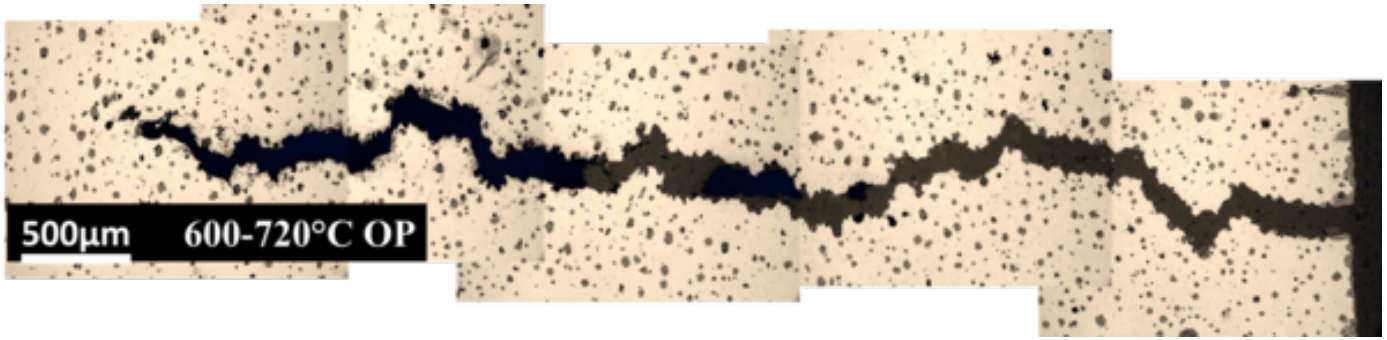

(b)

Figure 3.25: Optical microscope images of the longitudinal cross-section in specimens tested in OP TMF for temperature ranges of (a) 300 to 720 °C and (b) 600 to 720 °C. Continued on next page, (c) 300 to 800 °C, and (d) 600 to 800 °C.

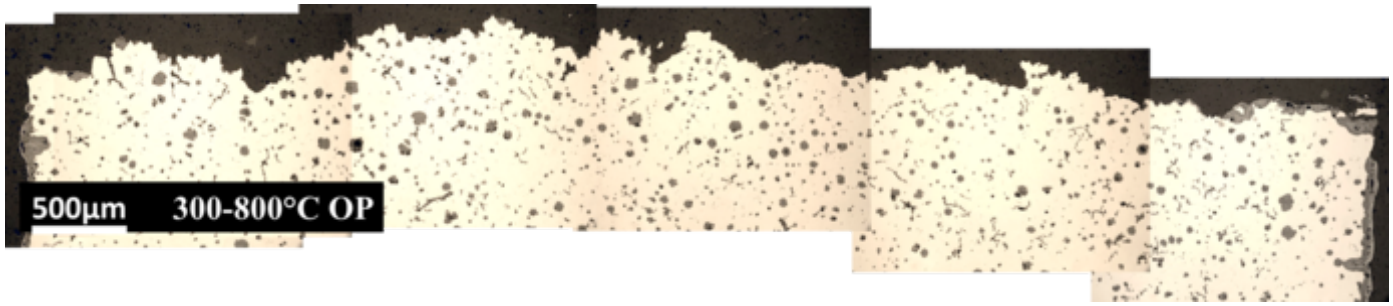

(c)

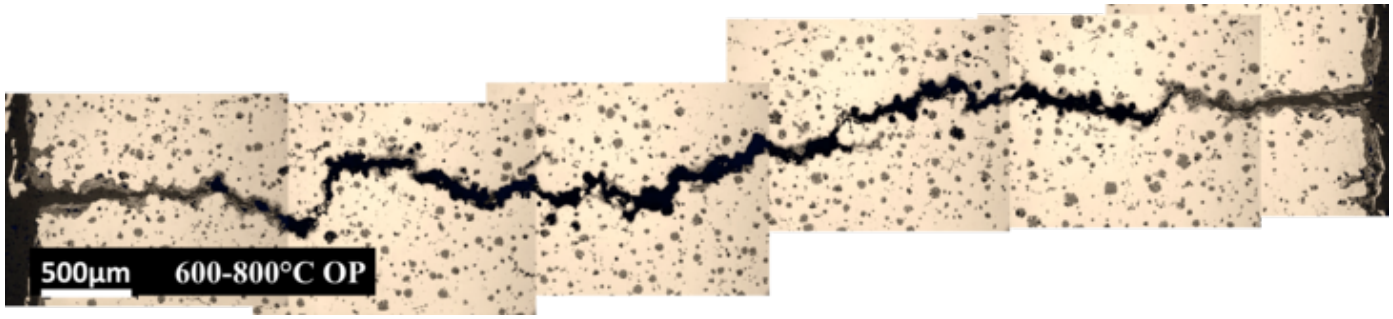

(d)

Figure 3.25: Continued from previous page.

3.5 Discussion

Crack initiation in both phasings occurs by fracture of the surface oxide layer, and subsequent penetration of the oxide into the specimen via repeated fracture and re-oxidation of the fresh metal at the crack tip. In IP TMF, this mechanism dominates the majority of the TMF crack growth process. The IP TMF life is similar for the thermal cycles considered, and a measurable improvement in IP TMF life occurs only when both the minimum and maximum temperature of the thermal cycle are significantly reduced. The rate of oxidation is slower at lower temperatures, and thus it would take more time for the oxide layer at the crack tip to reach the critical thickness.

In OP TMF, the penetration of the oxide contributes far less to the overall TMF damage. While this mechanism causes the initiation of the fatigue crack, the propagation of the crack is significantly influenced by the fracture of both the grain boundaries and the nodules. Particularly when the OP TMF cycle is inclusive of 400 °C, the fracture of embrittled grain boundaries contributes greatly to the TMF damage, as shown by fractographic observations of tested specimens. The TMF life is shorter in this case indicates that the fracture of embrittled grain boundaries occurs more quickly than fracture by either oxide intrusion (in IP TMF) or by transgranular linking of fractured nodules (in OP TMF with high minimum and maximum temperatures).

The embrittled mechanism is active only when the temperature of the test is near 400 °C, as shown by tensile and LCF tests conducted various intermediate temperatures. However, the fractographic findings of this study show that the embrittlement is only damaging in OP TMF. Recall from Section 3.3.1 that the OP TMF loop features a compressive strain and a tensile stress near 400 °C, while the IP TMF loops features a tensile strain and a compressive stress near 400 °C. A tensile stress would result in the opening of the grain boundaries perpendicular to the applied load, and this would be more conducive to the development of a crack than a compressive

stress, which would close a crack. Thus, the application of a tensile stress near 400 °C is necessary for the embrittlement mechanism to be damaging. The application of a compressive stress near 400 °C does not result in damage from the embrittlement mechanism, although it is active at this temperature.

Wu et al. (2015) conducted a study of the TMF life and failure modes of a HiSiMo DCI alloy and concluded that fracture in OP TMF occurred by either plasticity or oxidation when the stress was high. Fracture in IP TMF was attributed to plasticity and the growth of internally distributed damage via creep or 400 °C embrittlement. Tests were conducted with the mechanical strain 180° out-of-phase with the thermal strain for the OP case, and 0° out-of-phase in the IP case, as in the current study. However, the extensive experimental work and fractographic analysis conducted in the dissertation work shows that damage by oxidation contributes more to the growth of the TMF crack in the IP case, and the embrittlement mechanism does not contribute to damage in the IP TMF case. Instead, 400 °C embrittlement is damaging only in the case of OP loading. Furthermore, the authors posited that damage by internally-distributed defects from either creep or 400 °C embrittlement would result in similar rate of damage accumulation, and combined consideration of both mechanisms in their damage model. However, the dissertation work shows that damage by the embrittlement mechanism accumulates at a much faster rate than other modes of damage. This is evidenced by the very short TMF lives observed where the embrittlement was found to be damaging.

Thus, the modes of damage which are found by the dissertation work to be predominant in TMF loading of HiSiMo DCI are not correctly accounted for in the existing models for TMF damage in the material.

3.6 Summary of the Thermomechanical Fatigue Behavior and Failures Modes of HiSiMo DCI

A thorough examination of the thermomechanical fatigue behavior of HiSiMo DCI was conducted to learn the relevant damage modes which influence the strain-life behavior of the material under anisothermal cycling. The key findings of the TMF characterization of the HiSiMo DCI considered in the present study are summarized below:

1. The TMF crack initiates due to fracture of the surface oxide layer for all the thermal cycles considered,
2. IP TMF crack propagation occurs by the cyclic fracture and regrowth of an oxide intrusion, leading to similar IP TMF life for the thermal cycles considered,
3. OP TMF life is generally less than IP TMF life for the various thermal cycles considered,
4. The primary mechanism of crack growth in the OP TMF case depends on the temperature; when the thermal cycle includes 400 °C, the embrittlement of grain boundaries dominates the crack growth process and results in very short TMF lives,
5. The 400 °C embrittlement of HiSiMo DCI is damaging only when a tensile stress is applied.

3.7 Comparison of TMF and LCF Failure Modes

The anisothermal cycling of TMF loading introduces a new form of damage in the cyclic fracture of the surface oxide, and subsequent oxide intrusion, that was not observed in isothermal LCF tests. This occurs due to the mismatch in thermal strains of the oxide layer and the metal substrate. However, comparing the OP and IP TMF life for 600 to 800 °C to the isothermal LCF life at 800 °C in Figure 3.26a, it is clear that the fatigue lives are similar for all three loading cases for the same mechanical strain amplitude. Thus, this introduction of this mechanism does not greatly influence the rate of TMF damage accumulation.

When considering the mechanism of 400 °C embrittlement, which is active in both isothermal and anisothermal cycling, a significant different is found between LCF and OP TMF life. Figure 3.26b compares the isothermal LCF at 400 °C with the OP TMF tests where the thermal cycle includes 400 °C. The OP TMF life is significantly less than the isothermal LCF life for the same mechanical strain amplitude. This suggests that the embrittlement mechanism contributes a greater degree of damage in the OP TMF case than in the isothermal case. Recalling that the 400 °C embrittlement is damaging only when a tensile stress is applied, it is important to realize that half of each LCF occurs during a compressive stress. Thus, less damage by embrittlement can occur in an isothermal, fully reversed cycle.

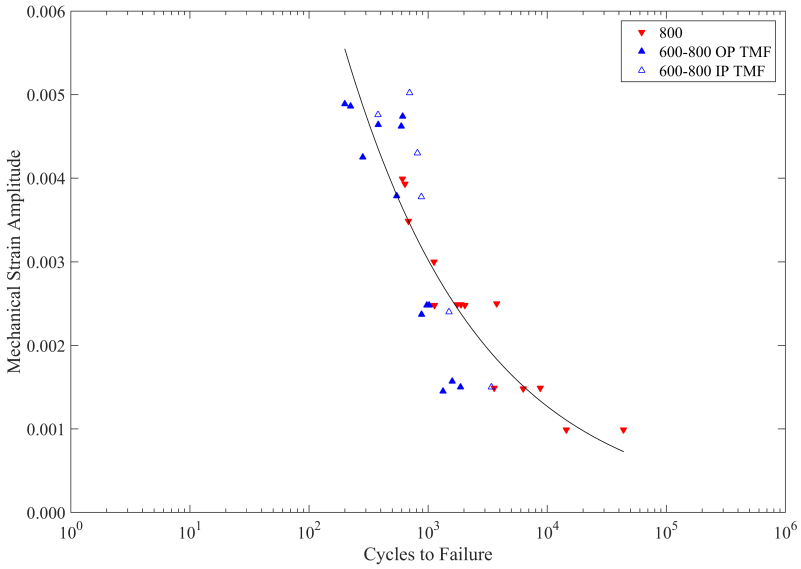

(a)

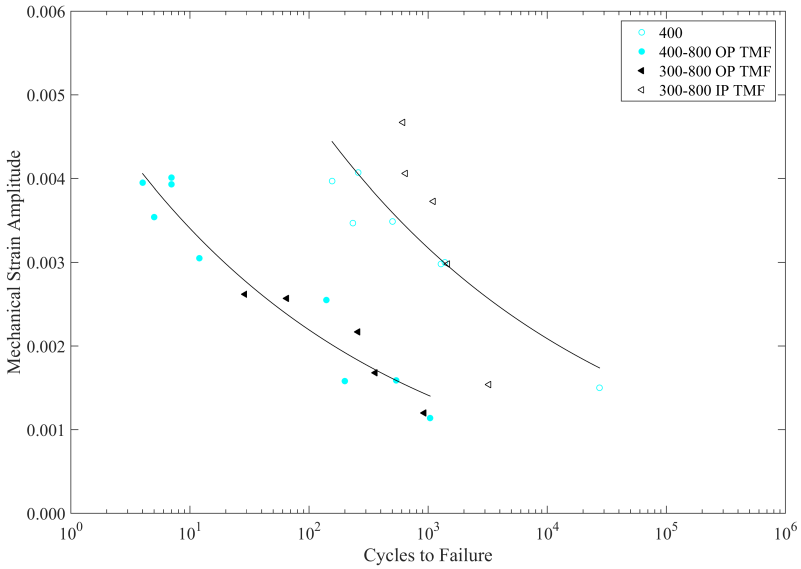

(b)

Figure 3.26: Comparison of the LCF and TMF lives where (a) the LCF cycle occurs at 800 °C and the TMF cycle occurs at 600 to 800 °C, and (b) the LCF cycle occurs at 400 °C and the TMF cycle has a minimum temperature of 300 or 400 °C.

CHAPTER IV

TMF Life Prediction by Linear Damage Summation

A 1991 survey of the evolution of creep-fatigue life prediction models revealed the existence of more than 100 models or variations of models used for cyclic crack initiation life (*Halford*, 1991). However, while each has, to some extent, been successful in predicting fatigue life for a specific set of data, most lack sufficient generality which would allow them to achieve widespread acceptance. According to *Manson and Halford* (2009), the number of creep-fatigue models proposed in the early 1990's increased at an average rate of about 5 per year, though the rate has decreased in more recent years due to a reduction in funding for this area of research in industry and academic settings.

4.1 Review of High Temperature Life Prediction Criteria

Brief descriptions of key models are given below to provide a historical framework for the discussion on a proposed modeling technique that follows later in the chapter.

4.1.1 Coffin-Manson Relation

In the 1950's, *Manson* (1953) in the United States and *Coffin* (1954) in the United Kingdom independently developed a description relating the high temperature fatigue life to the inelastic strain of a material. The so-called Coffin-Manson equation was introduced in Equation 2.1, and is given by

$$\frac{\Delta\varepsilon_{in}}{2} = \varepsilon'_f \left(2N_f\right)^c \tag{4.1a}$$

where $\Delta\varepsilon_{in}$ is the inelastic strain range, ε'_f is the fatigue ductility coefficient, and c is the fatigue ductility exponent.

Coffin (1973) later modified this relationship to a frequency-modified form given by

$$\frac{\Delta\varepsilon_{in}}{2} = \varepsilon'_f \left(2N_f\right) \nu^{k_1} \tag{4.1b}$$

where ν is the frequency and k is a temperature-dependent constant. While the frequency-modified life equation has demonstrated some utility to explain the effect of hold times, strain rate and asymmetric straining on certain materials under isothermal conditions, this model contains inherent ambiguity in identifying the meaning of plastic strain range when both time-independent and time-dependent damage processes are present. Consequently, further models were proposed to account more explicitly for high temperature damage mechanisms.

4.1.2 Time- and Cycle-Fraction Rule

Robinson (1952) proposed that creep damage occurring at a given stress and temperature could be estimated by $^{t}/_{t_r}$ where t is the time duration of an applied stress and t_r is the time to rupture under the given conditions. *Taira* (1962) later proposed a similar relation for the fatigue damage, such that for $^{n}/_{N_f}$, n is the number of applied cycles and N_f is the number of cycles to cause fatigue failure under the

same conditions. The Time- and Cycle-Fraction Rule is then given by

$$\sum \frac{t}{t_r} + \sum \frac{n}{N_f} = K \tag{4.2}$$

where the constant K is a characteristic of a material. The Time- and Cycle-Fraction Rule was adopted by the ASME Boiler and Pressure Vessel Piping Code in 1986 to provide a prediction of fatigue life for nuclear plant components which undergo combined creep and fatigue (*American Society of Mechanical Engineers*, 1986). While this method is generally capable of handling the effect of combined creep and plastic strain on life, the quality of fatigue life prediction varies drastically based on the actual interaction effect of creep and cycling, as shown by the results of *Kitagawa and Weeks* (1973), *Jaske et al.* (1973) and *Manson* (1973). To mitigate this concern, the PVP community codified the use of special creep-rupture and fatigue master curves that are based on a large number of tests to provide routinely conservative life estimates (*American Society of Mechanical Engineers*, 1986). A modified time-cycle fraction rule has also been applied to cumulative damage methods (*Bui-Quoc and Biron*, 1977; *Bernard-Connolly et al.*, 1978; *Lemaitre and Pumtree*, 1979; *Bui-Quoc and Gomuc*, 1983; *Wilshire and Owen*, 1983).

4.1.3 Strain-Range Partitioning

Strain-range partitioning (SRP) further clarifies the high temperature fatigue life prediction by explicitly considering the effect of cyclic creep, and the interaction of creep and plasticity (*Manson et al.*, 1971; *Manson and Halford*, 2009). SRP is based on a generalization of the Manson-Coffin equation where the inelastic strain is divided into four segments: plastic strain reversed by plastic strain (PP), plastic strain reversed by creep strain (PC), creep strain reversed by plastic strain (CP) and creep strain reversed by creep strain (CC). The cycles described by each of these

components is shown schematically in Figure 4.1. Three of the four can be present in any proportion in a given stress-strain cycle, with PC and CP being mutually exclusive. The general form of the strain-life relationships is given by

$$\Delta\varepsilon_{ij} = A_{ij}(N_{ij})^{c_{ij}} \tag{4.3}$$

where ij = PP, PC, CP, and CC. A_{ij} and c_{ij} are material constants which must be determined for each type of cycle.

SRP has shown good applicability to a wide range of materials, including austenitic and ferritic stainless steels, low- and high-alloy steels, various superalloys (nickel-, cobalt- and tantalum-base) and titanium alloys (*Hirschberg and Halford*, 1976; *Halford et al.*, 2000; *Lui et al.*, 2000). While the apparent simplicity of the SRP model is attractive, it is imperative that the experimental characterization accurately distinguish plastic strain from creep strain to allow the determination of the model parameters. The separation of the plastic and creep portions of the inelastic strain is not trivial in the general case. This is one the key difficulties faced when implementing the SRP method for estimating fatigue life.

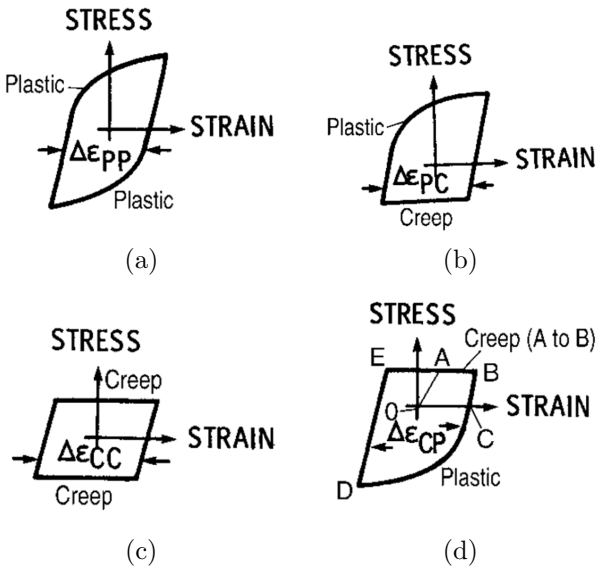

Figure 4.1: Schematic illustrations of the SRP loops described by (a) PP, (b) PC, (c) CC, and (d) CP. From *Manson et al.* (1971).

4.1.4 Damage Rate Accumulation

First introduced in 1976 by *Majumdar and Maiya*, the method of Damage Rate Accumulation, as it was termed by the authors, is based on the treatment of creep-fatigue as a propagation-controlled problem, where creep damage ahead of the fatigue crack affects crack growth rate, and *vice versa*. The researchers experimentally observed that the elevated-temperature failure of austenitic stainless steels resulted in fracture surfaces that exhibited features which depend on strain rate, temperature, environment, hold time and loading sequence. They consequently proposed a generalized damage-rate equation to reflect the interaction between a crack and cavities in a given environment. The recognition and experimental verification of two independent mechanisms of damage accumulation (crack growth and void growth) which evolve simultaneously is of great importance to the development of theories at the time. The original equation was further modified by *Majumdar and Maiya* (1979) to account for creep damage occurring by grain-boundary cavitation (in addition to bulk creep

damage), resulting in the final formulation:

$$\frac{1}{a}\frac{da}{dt} = \text{T or C}\left[1 + \alpha \ln\left(\frac{c}{c_o}\right)\right][|\varepsilon_p|]^m[|\dot{\varepsilon}_p|]^k \tag{4.4}$$

where T and C denote tensile and compressive loading, respectively, α and c_o are material constants, and m and k are constants that do not depend on temperature or strain rate (*Majumdar and Maiya*, 1980). Damage Rate Accumulation was successfully applied to austenitic stainless steels for power plant applications, where grain boundary cavitation is of critical importance to the failure of structural components, and to TMF loading of an austenitic stainless steel where IP TMF was found to be more damaging than any other isothermal or anisothermal condition (*Majumdar*, 1987).

4.1.5 Fracture Mechanics Approaches for Crack Propagation

More recent models for the prediction of high temperature fatigue life have been based on the concept that damage due to creep or oxidation can modify the fatigue crack growth rate. *Wareing* (1977) recognized that high temperature fatigue is bounded by two extremes: in the absence of creep, the rate of damage accumulation is controlled by the size of the plastic zone ahead of the crack tip. However, in the presence of extensive creep, the rate of damage accumulation is commensurate with the rate of creep in the bulk material. When considering both damage mechanisms acting simultaneously in creep-fatigue, the effect of creep cavity growth ahead of the crack tip is similar to using crack tip opening displacement (CTOD). In this case, modified fracture mechanics parameters may be used (*Wareing*, 1977; *Tomkins*, 1981; *Jaske*, 1983). Even when cavities are not present but creep damage is accumulating, the crack tip stress/strain fields are still modified (*Tien et al.*, 1985). For example, intergranular damage and grain boundary sliding are both creep-related damage pro-

cesses which influence the crack tip plastic zone (*Min and Raj*, 1978; *Baik and Raj*, 1982a,b; *Levaillant and Pineau*, 1982; *Rie and Schmidt*, 1987).

Reuchet and Rémy (1979) found that time-dependent bulk damage accumulated in a cobalt-base superalloy at high temperatures which led to a substantial decrease in fatigue life. The decrease in fatigue life at high temperatures was shown to result from quicker fatigue crack initiation due to oxidation damage, and also an increased rate of fatigue crack propagation due to oxidation and creep damage (*Reuchet and Rémy*, 1979).

Saxena and Bassani (1984) proposed an oxidation-modified crack growth law involving the stress intensity factor range (ΔK) for long crack growth where oxidation kinetics were included at the crack tip. Oxidation in this case followed a parabolic relation to the duration of a hold time for the steels and Ni-based superalloys which were studied. *Liu and Oshida* (1986) implemented a similar model based on linear elastic fracture mechanics as modified by grain boundary oxidation. In this case, the fatigue-oxidation crack growth rate was found to increase linearly with hold time or strain rate.

4.2 Predictions of TMF Life

4.2.1 From Isothermal Methods

Halford and Saltsman (1987) attempted to predict TMF life from isothermal data by assuming a time- and temperature-independent failure criterion for three basic prediction models, including total strain range, inelastic strain range, and the Ostergren approach. The Ostergren method, introduced by *Ostergren* (1976), is based on the inelastic strain energy dissipated due to a tensile stress according to

$$W_T = \oint \alpha \left(\sigma - \sigma_o\right) \, d\varepsilon_{in} \tag{4.5}$$

where σ_t is the maximum tensile stress and σ_o is the mean stress. In the study by *Halford and Saltsman* (1987), the inelastic strain range criterion gave the most reasonable interpretation of TMF behavior, while the total strain range and Ostergren parameters required improbable material flow and/or failure behavior to produce numerically correct TMF life predictions due to the unique damage introduced during a TMF cycle by time- and temperature-dependent effects (*Halford and Saltsman*, 1987). *Skelton* (1978) found that isothermal fatigue life at the maximum temperature of the thermal cycle could provide conservative estimates for the OP TMF life in a 0.5Cr-Mo-V steel. Other authors have also attempted to predict the fatigue life from the isothermal fatigue life at a particular temperature in the thermal cycle – use of the maximum, minimum or equivalent temperature of the thermal cycle have all shown some degree of success (*American Society of Mechanical Engineers*, 1984; *Swindeman and Douglas*, 1959; *Taira*, 1973), as has predicting TMF life from the temperature of minimum isothermal fatigue resistance (*Spera*, 1969).

The plurality of TMF life prediction schemes based on isothermal data indicates, as reported by *Karasek et al.* (1988), that the utility of isothermal fatigue life to predict TMF life is highly dependent on the range of the thermal cycle with respect to the activation temperatures of the high temperature damage mechanisms. Thus, the temperature level where isothermal fatigue life predictions could provide satisfactory predictions of TMF life is not known *a priori*. This is because, at elevated temperatures, environmental and creep effects on life can become significant, and both mechanisms are activated simultaneously to lower the fatigue life. These damage mechanisms change with strain range, temperature, phasing between mechanical and thermal strain, and strain rate; in most cases, the strain-temperature variation with time and the material condition will dictate which mechanism is the most damaging (*Neu and Sehitoglu*, 1989b). A general TMF prediction model must not be restricted to a few strain rates, temperatures, or strain ranges.

4.2.2 Neu-Sehitoglu Model (Linear Damage Summation)

Due to the limitations of correlating isothermal temperature performance with non-isothermal durability, it is important to recognize that critical structural components undergo a complicated temperature-strain history which cannot be easily interpreted from an isothermal framework. According to a recent review conducted by *Manson and Halford* (2009), the current state-of-the-art for predicting TMF life is a mechanistic model proposed by Professor Huseyin Sehitoglu and his graduate students at the University of Illinois at Urbana-Champaign (*Neu and Sehitoglu*, 1989a,b). This model is based on physical damage measurements which are identified with measures of lifetime under conditions of interacting oxidation, creep and fatigue. The Neu-Sehitoglu model is based on a linear damage summation of fatigue, creep and oxidation damages as

$$D^{total} = D^{oxidation} + D^{creep} + D^{fatigue} \tag{4.6a}$$

$$\frac{1}{N_f} = \frac{1}{N_f^{oxidation}} + \frac{1}{N_f^{creep}} + \frac{1}{N_f^{fatigue}} \tag{4.6b}$$

where the damage by each mechanism accumulates per cycle. The fatigue damage is given by the strain-life relationship at *room temperature* such that

$$\frac{\Delta\varepsilon_{mech}}{2} = \frac{\sigma'_f}{E}\left(2N_f^{fat}\right)^b + \varepsilon'_f\left(2N_f^{fat}\right)^c \tag{4.7}$$

where $\Delta\varepsilon_{mech}$ is the total mechanical strain range, σ'_f is the fatigue strength coefficient, E is the Young's modulus, b is the fatigue strength coefficient, ε'_f is the fatigue ductility coefficient, and c is the fatigue ductility exponent. None of the fatigue damage parameters vary with temperature.

Oxidation-fatigue damage is considered by *Neu and Sehitoglu* (1989b) to occur in two distinct ways. Type I oxide growth is characterized by a continuous oxide layer

which forms on the metal surface, and ruptures upon reaching a critical thickness, h_{f1}. A new oxide layer forms on the freshly exposed crack tip and fractures again upon reaching a new critical thickness, h_{f2}, and so on. In this way, the crack advance is aided by fracture of the oxide layer. In Type II oxide growth, the fracture of the oxide layer causes it to also detach from the surface, exposing a larger fresh surface for new oxidation, resulting in a wider intrusion. Type II oxidation is characterized by a stratified appearance, while Type I results in a continuous layer of oxidation. *Neu and Sehitoglu* (1989b) proposed a unified oxidation-fatigue damage term to account for either oxidation mechanism that is given by

$$\frac{1}{N_f^{oxidation}} = \left[\frac{h_{cr}\delta_o}{B\Phi^{oxidation}K_p^{eff}}\right]^{-1/\beta} \frac{2(\Delta\varepsilon_{mech})^{2/\beta+1}}{\dot{\varepsilon}^{(1-a/\beta)}} \tag{4.8}$$

where h_{cr} is the critical oxide length up to which crack growth is dominated by environmental attack, $\dot{\varepsilon}$ is the total strain rate, δ_o is a material constant related to the ductility of the oxidized metal, and a, B and β are constants. $\Phi^{oxidation}$ is an experimental parameter that accounts for different mechanical-thermal phasings and is given by the equation

$$\Phi^{oxidation} = \exp\left[-\frac{1}{2}\left(\frac{\varepsilon_{th}/\varepsilon_{mech}+1}{\xi^{oxidation}}\right)^2\right] \tag{4.9}$$

where $\psi^{oxidation}$ is an empirical parameter. A fully-constrained OP TMF test results in a value of $\Phi^{oxidation} = 1$. This represents the most damaging case for oxidation-fatigue damage.

K_p^{eff} is the effective oxidation constant for parabolic growth of an oxide of Type I or Type II. It is assumed in this case that the oxide penetrates the metal substrate

to form a dominant crack. The form of K_p^{eff} is given by

$$K_p^{eff} = \frac{1}{t_c} \int_0^{t_c} D_o e^{(-Q/RT(t))} dt \tag{4.10}$$

where D_o is the diffusion coefficient and Q is the activation energy for oxidation. It is important to note that the use of an effective oxidation constant accounts for the net kinetic resulting from the growth of different oxide layers, as well as the accelerated oxidation rate due to repeated exposure of fresh metal at the crack tip averaged over the duration of the thermal cycle. The effective parabolic constant is consequently larger than would be measured from static oxidation tests.

Finally, creep-fatigue damage is described by

$$D^{creep} = \Phi^{creep} \int_0^{t_c} A e^{(-\Delta H/RT(t))} \left[\frac{\alpha_1 \overline{\sigma} + \alpha_2 \sigma_H}{K} \right]^m dt \tag{4.11}$$

where K is the drag stress in the unified constitutive equation developed by *Neu and Sehitoglu* (1989a), α_1 and α_2 are coefficients accounting for the difference in creep damage occurring in tension and compression, $\overline{\sigma}$ is the effective multiaxial stress, σ_H is the hydrostatic component of stress, ΔH is the activation energy for creep, and A and m are material constants. Φ^{creep} is the mechanical-thermal phasing factor for creep-fatigue damage (similar to that for oxidation), and is given by

$$\Phi^{creep} = \exp \left[-\frac{1}{2} \left(\frac{\varepsilon_{th}/\varepsilon_{mech} - 1}{\xi^{creep}} \right)^2 \right] \tag{4.12}$$

where ψ^{creep} is an empirical constant. Φ^{creep} provides a measure of the relative amount of creep-fatigue damage for different thermal strain ratios. The expression for creep in Neu-Sehitoglu's formulation explicitly accounts for both tensile and compressive creep, and the importance of each is determined by the experimental coefficients α_1

and α_2.

While the Neu-Sehitoglu model relies on the linear summation of each damage mode, it is important to recognize that the interaction of modes is implicitly included in the phasing factors, $\Phi^{oxidation}$ and Φ^{creep}. These factors can be interpreted from experimental data and relate the different rates of damage accumulation due to oxidation and creep that occur in different thermal cycles. The Neu-Sehitoglu model employs a very large number of experimental parameters which should be experimentally determined, and this is the predominant difficulty in applying the Neu-Sehitoglu model for predictive purposes. Nevertheless, it is a sophisticated and thorough model for TMF damage that has been successfully used to predict the TMF life of a high carbon steel for a rail application (*Neu and Sehitoglu*, 1989b) and various aluminum alloys for automotive applications (*Su et al.*, 2002; *Minichmayr et al.*, 2008).

4.3 Prior Work on TMF Life Prediction of HiSiMo DCI

Previous researchers have examined the constitutive and fatigue behaviors of ductile cast iron under conditions of isothermal and thermomechanical cycling. *Charkaluk and Constantinescu* (2000) compared the low cycle fatigue behavior of SiMo cast iron with several measures of fatigue damage, including plastic strain amplitude, the Smith-Watson-Topper parameter, and tensile hysteretic energy, and found that the dissipated energy per cycle provides the best correlation with experimental observations of fatigue life.

Hazime et al. (2003) examined the high temperature fatigue behavior of a HiSiMo DCI exhaust manifold subjected to thermal cycling, and devised a fatigue life prediction scheme based on the Strain Range Partitioning method. In this case, the authors attributed the majority of damage to creep deformation and used a commercially-available constitutive model to distinguish the plastic and creep components of the inelastic strain.

Kim et al. (2009) conducted a study of the high temperature fatigue properties for HiSiMo DCI at room temperature, 600 and 800 °C. The authors found that fatigue failure at high temperatures was influenced by an increased rate of oxidation and cyclic softening of the material, but found that the Coffin-Manson relationship provided a reasonable description of the strain-life behavior at the tested temperatures.

Szmytka et al. (2010) constructed a unified elastoviscoplastic constitutive model for SiMo cast iron based on dislocation theory. The constitutive model was applied by *Benoit et al.* (2012) to predict the TMF life of an automotive exhaust manifold through consideration of energy dissipation due to elastic shakedown, plastic shakedown and ratchetting behaviors. The constitutive model was later revised by *Rémy et al.* (2013) with a flow rule to account for cyclic stress relaxation under a strain hold to improve the fatigue life correlation for OP TMF life.

Seifert and Riedel (2010) devised a viscoplastic model that accounted for porous plasticity to represent the constitutive behavior of DCI. The authors applied a fracture mechanics-based crack-tip blunting model to predict the thermomechanical fatigue life of nodular cast iron (*Seifert et al.*, 2010). *von Hartrott et al.* (2014) later revised the damage model to account for the embrittlement which occurs in HiSiMo DCI and found good correlation with a limited number of TMF tests. *Seifert et al.* (2014) reformulated the damage model for the multiaxial case and found good agreement for the TMF life prediction of a component subjected to transient thermal gradients.

Wu et al. (2015) later conducted a more expansive study of the high temperature fatigue behavior of HiSiMo DCI, including thermomechanical fatigue. The authors implemented an integrated creep-fatigue (ICF) model for the constitutive and damage equations of the DCI. The damage model, which was based on fracture mechanics, accounted explicitly for fatigue, creep and oxidation damage. They also accounted for the embrittlement observed near 400 °C by modifiying the fracture toughness with a temperature-dependent function. The ICF model showed good agreement with a

limited number of TMF tests conducted in the embrittled temperature range.

4.4 TMF Life Prediction of HiSiMo DCI by Linear Damage Summation

Since the Neu-Sehitoglu model provides the most comprehensive description of the TMF failure behavior, it was chosen in the dissertation work to represent the observed isothermal and thermomechanical fatigue behavior for the many tests conducted on HiSiMo DCI. No source in the literature has previously attempted to apply the Neu-Sehitoglu model to the TMF life prediction in this material. The model was implemented for the uniaxial formulation to correlate with the fatigue life resulting from coupon tests.

4.4.1 Determination of Neu-Sehitoglu Parameters

There are 21 empirical parameters in the Neu-Sehitoglu model that must be determined from the isothermal and thermomechanical fatigue data at different temperatures. This section discusses how the data generated in this study were applied to fit the parameters. Many combinations of the isothermal and TMF tests were used to fit the parameters with varying success to achieve a good prediction of the uniaxial fatigue life. The fitting described here represents the best combination to provide the overall best fatigue life prediction for the many tests conducted in the dissertation work.

4.4.1.1 Fatigue Parameters

The Neu-Sehitoglu model has five fatigue parameters which must be determined from experimental data, and they are the coefficients and exponents used in the strain-life equation. The model was developed to consider the room temperature fatigue

behavior as the upper bound for isothermal or anisothermal fatigue life. Thus, σ'_f, E, and b, and ε'_f and c were determined from the elastic and inelastic components of strain of the room temperature fatigue data, respectively. Since the thermal strain is zero in this case, the elastic and inelastic strain amplitudes were calculated as

$$\frac{\Delta\varepsilon_{mech}}{2} = \frac{\Delta\varepsilon^{el}}{2} + \frac{\Delta\varepsilon^{in}}{2} = \frac{\Delta\sigma}{2E} + \frac{\Delta\varepsilon^{in}}{2} \tag{4.13}$$

where the mechanical strain range $\Delta\varepsilon$ is controlled in the tests, and E is the Young‘s Modulus at room temperature. The life data were then fitted against the components of strain. A numerical optimization algorithm was used to minimize the error between the predicted and observed fatigue lives where the error was defined by

$$\text{error} = \left(\frac{\ln(N_f^{\text{observed}}) - \ln(N_f^{\text{predicted}})}{\ln(N_f^{\text{observed}})} \right)^2 \tag{4.14}$$

where ln is the natural logarithm. Figure 4.2 shows the room temperature fatigue data with the curve given by the fitted Neu-Sehitoglu (strain-life) model.

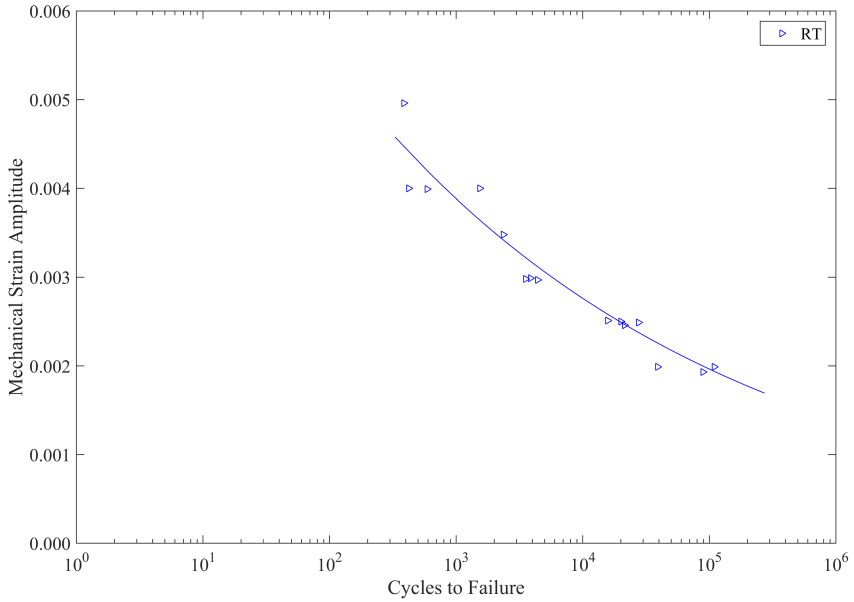

Figure 4.2: Experimental room temperature fatigue data (points) with the fitted strain-life model (curve) for the Neu-Sehitoglu model.

4.4.1.2 Oxidation-Fatigue Parameters

The oxidation-fatigue term of the Neu-Sehitoglu model contains nine parameters which must be experimentally determined. These parameters are D_o, Q^{ox}, $\overline{h}_f$, B, β, δ_o, a, h_{cr}, and ξ^{ox}. Oxidation-fatigue damage was determined for two groupings of the test data: the first grouping was selected without regard to the embrittled behavior and included isothermal tests at 400, 500 and 600 °C, as well as OP TMF tests in the temperature range 500 to 800 °C. The OP TMF test condition was used since the model assumes that oxidation-fatigue damage is higher for OP TMF. OP TMF tests with a minimum temperature of 300 or 400 °C were not used in the second grouping since fractography of the tested specimens did not show significant damage by oxidation-fatigue (recall that these specimens showed extensive damage by the 400 °C embrittlement). The second grouping prioritized the life reduction observed at the embrittled temperature and included isothermal tests at 400 and 500 °C, and OP TMF tests with minimum temperatures of 300 and 400 °C. This was done to try

to force the Neu-Sehitoglu model to represent the loss of isothermal and TMF life seen at these temperatures. To simplify the numerical optimization, h_{cr}, B, D_o and δ_o were combined into a single parameter:

$$\mathbb{C} = \frac{h_{cr}\delta_o}{BD_o} \tag{4.15}$$

so that Equation 4.8 would be simplified as

$$\frac{1}{N_f^{oxidation}} = \left[\frac{\mathbb{C}}{\Phi^{oxidation} K_p^{'eff}}\right]^{-1/\beta} \frac{2(\Delta\varepsilon_{mech})^{2/\beta+1}}{\dot{\varepsilon}^{(1-a/\beta)}}. \tag{4.16}$$

The activation energy Q for oxidation was approximated from tests of static oxidation so that $\mathbb{C}$ was the only unknown to be calculated from $K_p^{'eff}$ according to Equation 4.10.

Interestingly, after optimizing the remaining parameters, it was found that $\Phi^{oxidation} = 1$ would give the best correlation with the experimental data, regardless of the data set used. This means that the oxidation-fatigue damage is comparable for the isothermal and TMF cases for the HiSiMo material.

4.4.1.3 Creep-Fatigue Parameters

The creep-fatigue damage term in the Neu-Sehitoglu model contains seven experimentally-determined parameters: A, ΔH, α_1, α_2, K, m and ξ^{creep}. The activation energy for creep ΔH was estimated from a limited number of creep tests at 650 and 700 °C. The steady-state creep rate was determined at a stress level of 40 MPa and the activation energy was calculated according to

$$\Delta H = \frac{R\ln(\dot{\varepsilon}_1/\dot{\varepsilon}_2)}{(1/T_2) - (1/T_1)} \tag{4.17}$$

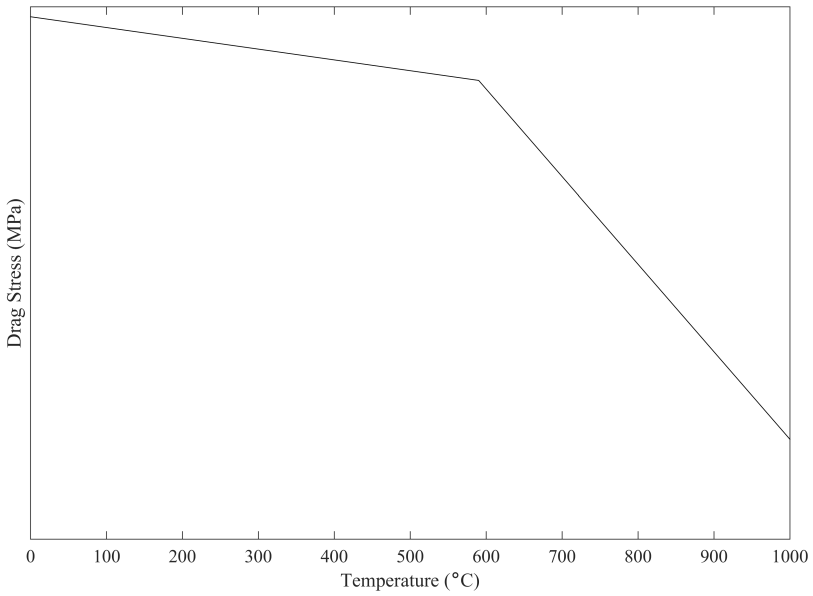

Figure 4.3: A schematic of the temperature-dependent value of the drag stress, K, for the Neu-Sehitoglu damage model. Please note that the ordinate axis is presented without values.

where R is the ideal gas constant. The drag stress, as defined by *Neu and Sehitoglu* (1989b), describes the stress at each temperature at which the deformation becomes dominated by plasticity rather than creep. K can usually only be determined for a few temperatures, and is assumed to be proportional to the temperature-dependent Young‘s Modulus where

$$\frac{K}{E} = \text{constant}. \tag{4.18}$$

The value of the drag stress is shown schematically in Figure 4.3. Please note that the ordinate axis is presented without values in the dissertation work to protect Ford's proprietary information. In this case, one can infer that the HiSiMo material showed minimal strain-rate dependence at temperatures up to the inflection point, around 600 °C. However, about 600 °C, viscous behavior develops and the strength becomes increasingly dependent on the strain rate.

To fit the remaining parameters, A, α_1, α_2, m and ξ^{creep}, tests were conducted

at 800 °C with a slow strain rate of $5 \times 10^{-5}\,\mathrm{s}^{-1}$, and additionally with a ten minute hold time in tension or compression at 800 °C. Other data included in the parameter optimization were cyclic creep tests conducted at 600 °C and IP TMF tests in the range of 600 to 800 °C since the Neu-Sehitoglu model considers this test condition more likely to be damaged by creep. The results suggest that the phasing factor $\Phi^{creep} = 1$, as for oxidation, and that there is no difference in the rate of creep damage accumulation for different phasings of mechanical and thermal strain.

4.4.2 Fatigue Life Prediction

The 400 °C embrittlement experienced in HiSiMo DCI posed a difficult challenge for the Neu-Sehitoglu model. Since the model relies on the linear summation of damage by fatigue, creep and oxidation, it assumes that TMF damage increases monotonically with temperature. However, as observed in isothermal and TMF tests near 400 °C, the fatigue life of HiSiMo DCI is lower at 400 °C than at either 200 or 500 °C. There is no term in the Neu-Sehitoglu model that can account for the non-monotonic increase in TMF damage as temperature increases.

When the embrittled data are not prioritized in the numerical optimization procedure, the strain-life curve at 400 °C is severely over-predicted, as shown in Figure 4.4a, but the high temperature data are well-represented. In this case, the curves from room temperature up to 400 °C are coincident. Conversely, when the embrittled data were prioritized in fitting the model, the Neu-Sehitoglu model can provide a reasonable representation for the strain-life data from room temperature up to 400 °C. However, because damage can only increase with temperature, the fatigue lives at higher temperatures are severely under-predicted. Figure 4.4b shows the strain-life behavior for isothermal tests conducted up to 800 °C.

Similarly, the fatigue life prediction for TMF tests depends strongly on the emphasis placed on the embrittled data during the parameter optimization. The Neu-

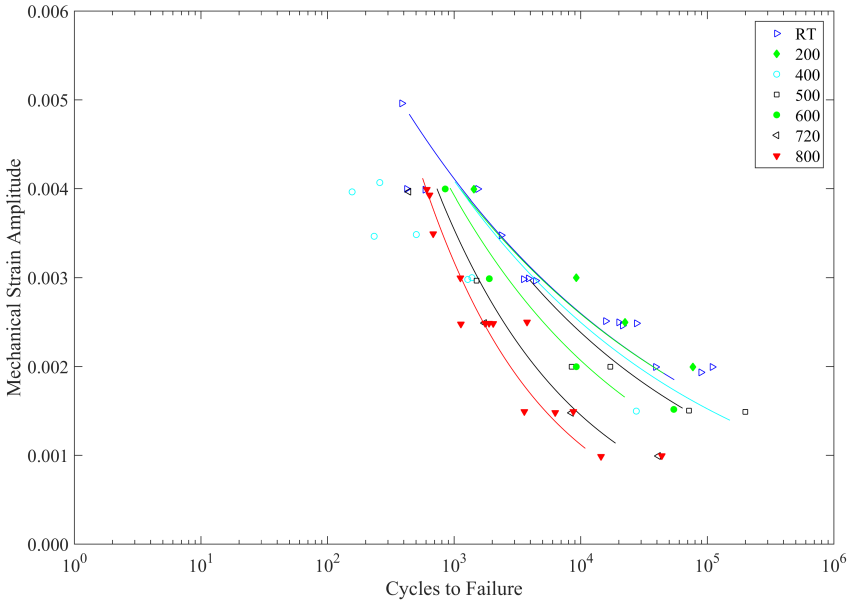

(a)

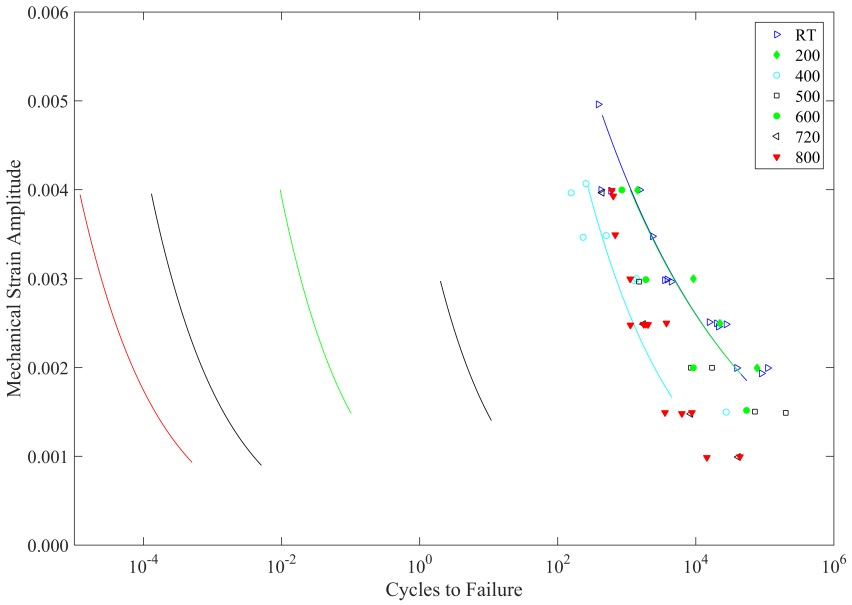

(b)

Figure 4.4: Strain-life curves predicted by the Neu-Sehitoglu model showing that good representation can be achieved for the fatigue performance of either (a) the high temperature data or (b) the embrittled data at 400 °C, but not both.

Sehitoglu model is applied to the more than 120 elevated temperature tests conducted in the course of the dissertation work in Figure 4.5. When the embrittled data are not prioritized in the fitting of the parameters, the Neu-Sehitoglu model can provide a good correlation for fatigue lives above about 100 cycles to failure. Based on the observed fatigue lives, only OP TMF tests with minimum temperatures of 300 or 400 °C are not well-predicted. For these cases, the model estimates fatigue lives up to two orders of magnitude higher than those observed for the very low lives.

However, it is important to remember that very short TMF lives were observed in the accelerated component validation tests conducted via dynamometer for the HiSiMo DCI manifold. Thus, it is important to the design and validation process to have the capability to predict TMF lives even at low numbers of cycles to failure.

When the embrittled data are prioritized in the fitting of the model, an interesting result occurs, as shown in Figure 4.5b. In this case, the isothermal data at 400 °C, and the OP TMF data with minimum temperatures of 300 or 400 °C were used the only terms used to fit the oxidation parameters of the Neu-Sehitoglu model. This was done in an attempt to force the model to account for the loss of fatigue performance observed in these tests. While the isothermal data at 400 °C are well-represented by the model, the OP TMF lives of the embrittled tests are poorly represented, with the shortest lives being severely over-predicted, and the longer lives being severly under-predicted. Furthermore, the fatigue lives resulting from higher temperature tests are under-predicted by many orders of magnitude, to the extent that the predicted fatigue lives are unrealistic.

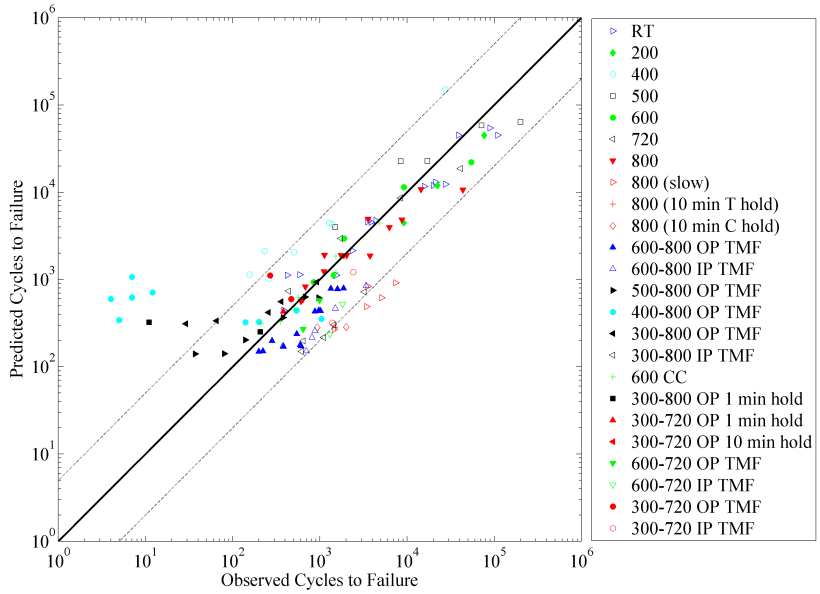

(a)

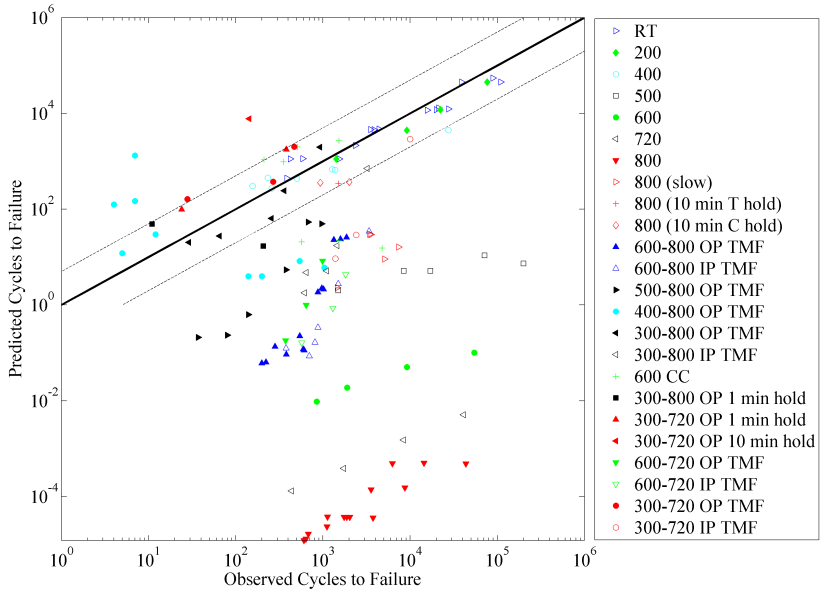

(b)

Figure 4.5: Comparison of the observed fatigue lives with those predicted by the Neu-Sehitoglu model showing that (a) the fatigue lives of the embrittled TMF conditions are over-predicted when the high-temperature data are well-represented; however, even forcing the model to account for the short life (b) results in a poor prediction of the fatigue lives.

4.4.3 Discussion

The Neu-Sehitoglu model has not been widely employed in the literature, presumably due to the vast amount of experimental data which must be generated to fit all the empirical and material constants. Even with the many tests conducted in this study, it was necessary to resort to numerical optimization of some of the parameters. When the parameters were fitted for the isothermal and TMF data, any tests involving the temperature of embrittlement, which corresponds to drastically reduced isothermal and TMF durability, were non-conservatively predicted.

It is important to recognize that the Neu-Sehitoglu model considers the room temperature fatigue to be the upper bound on TMF performance, and that additional damage due to oxidation and creep only serve to reduce the fatigue life. This implies that the damage done by the combination of creep, fatigue and oxidation increases monotonically with temperature. However, the fatigue life of HiSiMo DCI does not always change monotonically with temperature. As discussed in Chapter II, the low cycle fatigue life is significantly shorter at 400 °C at high strain ranges, but some improvement in performance is seen when the temperature is increased further. There is no mechanism built-in to the Neu-Sehitoglu model that can account for this manner of temperature-dependence of damage accumulation.

4.5 Conclusions

The Neu-Sehitoglu model, which employs a linear summation of the damage mechanisms which contribute to TMF failure, is considered the state-of-the-art for TMF life prediction. In the dissertation work, the Neu-Sehitoglu model was applied to predict the TMF life of HiSiMo DCI. A comprehensive database of isothermal and anisothermal tests was used to optimize the many empirical and material parameters of the model. The Neu-Sehitoglu model did well to predict the TMF life of HiSiMo

DCI when the fatigue life exceeded about 100 cycles. Unfortunately, it also provided a severe overprediction of the fatigue life when the number of cycles to failure was less than about 100. In general, these short lives were observed for OP TMF tests where the minimum temperature of the thermal cycle was 300 or 400 °C. Forcing the model to represent the embrittled data did not result in an improvement of the prediction. Despite the comprehensive nature of the Neu-Sehitoglu model, it cannot account for the embrittlement damage that occurs in HiSiMo DCI when a tensile stress is present near 400 °C, as in the case of OP TMF.

CHAPTER V

Development of a Model for TMF Life Prediction

Out-of-phase (OP) TMF is considered the most representative loading case for the manifold application, where the cooler sections constrain the hotter volumes of material, so it is of critical importance to provide an accurate estimate of OP TMF life. Additionally, OP TMF is greatly affected by the intermediate temperature embrittlement of HiSiMo DCI when the thermal cycle is inclusive of 400 °C.

The failure modes which contribute to the thermomechanical fatigue failure of HiSiMo DCI have been shown in the dissertation work to be multifarious. The damage done by the high temperature mechanisms of oxidation and creep increase monotonically, but the interaction of these damage modes with the fatigue cycling depends on the TMF phasing and the limits of the thermal cycle. An additional damage mechanism by embrittlement of the grain boundaries is activated in HiSiMo DCI near 400 °C, but is not active at lower or high temperatures, and it is only damaging when a tensile stress is present. When the embrittlement mechanism is damaging, it dominates the failure mode, even considering fatigue, creep and oxidation. Thus, the mechanistic description of TMF failure in HiSiMo DCI is complex.

The embrittled isothermal and TMF life was examined extensively in Chapter II and Chapter III, respectively. The fractographic observations made of these loading cases highlight the differences in the microscopic damage mechanisms that contribute

to failure in various combinations of thermal and mechanical loading. The comprehensive, mechanism-based model developed by *Neu and Sehitoglu* (1989b) was applied to the TMF life of HiSiMo DCI which required extensive testing data to fit the 21 empirical and material parameters of the model. Despite its complexity, the Neu-Sehitoglu model failed to provide a good representation for OP TMF life when the thermal cycle was inclusive of 400 °C because it could not account for the unique trend of temperature-dependence of the embrittlement mechanism that occurs in HiSiMo DCI .

To be practical to implement in an industry setting, the predictive framework should rely more on global, macroscopic measures of damage. Thus, the dissertation work revisits the phenomenological descriptions of TMF damage in an attempt to build, from the ground up, a robust and suitable description of the TMF life for HiSiMo DCI that is mechanistically-informed, but does not require the generation of such extensive testing data to be applied. In this chapter, various measures of high temperature fatigue damage will be used to interpret the test results for elevated temperature fatigue and thermomechanical fatigue of HiSiMo DCI in an effort to find a suitable measure of damage.

5.1 Macroscopic Measures of Damage

As a first approximation of the high temperature damage occurring in HiSiMo DCI, the mechanical strain is assessed as a damage parameter in Figure 5.1a for the more than 120 cyclic tests conducted in the dissertation work. As seen in the figure, the slope of the strain-life data is small, which indicates that the fatigue life has poor sensitivity to changes in the mechanical strain amplitude. Furthermore, the dispersion band is wide, and the scatter for a given mechanical strain amplitude is nearly two orders of magnitude of fatigue life. Thus, mechanical strain is not likely to provide a good correlation of damage and observed fatigue life.

By considering only the inelastic component of mechanical strain, the Coffin-Manson equation is assessed for the prediction of isothermal and TMF life of HiSiMo DCI. Recall that *Kim et al.* (2009) found that the Coffin-Manson relationship did well to collapse the isothermal fatigue life of HiSiMo DCI for tests at room temperature, 600 and 800 °C. When applied to the extensive testing data considered in the dissertation work in Figure 5.1b, the inelastic strain does not appear to give a suitable measure of the fatigue and TMF life. Due to the wide dispersion of the isothermal and TMF tests which represent the embrittled performance of HiSiMo DCI, the fatigue life varies about two orders of magnitude for a given inelastic strain amplitude. The Coffin-Manson relationship is thus shown to provide a poor representation of the fatigue life of HiSiMo DCI. However, the slope of the strain-life relationship is increased by considering only the inelastic component of strain.

It is important, at this point, to recognize that no additional benefit can be derived from distinguishing the plastic and creep components of the inelastic strain. The method of Strain Range Partitioning distinguishes the damage done by the plastic strain from that done by the creep strain. This method has shown good applicability to various materials for very high temperature applications where creep is of critical concern to the performance of structural materials. However, the purposeful addition of creep damage in tests of this HiSiMo DCI has had very little influence on the fatigue life. For example, tests were conducted at 800 °C at a slow strain rate of $5 \times 10^{-5}\,\mathrm{s}^{-1}$ (two orders of magnitude slower than the LCF tests), and with the addition of a 600 second (10 minute) hold time at the maximum tensile or compressive stress to greatly increase the degree of creep damage in the LCF cycle. As shown in Figure 5.2, there was no significant difference in the Coffin-Manson plots for the difference conditions, despite the vastly different proportions of creep and plastic damage occurring in these cycles. Additionally, cyclic creep tests, appropriate for use with the Strain Range Partitioning method, were conducted at 600 °C using a

waveform shown in Figure 5.3a. The Coffin-Manson plot is shown in Figure 5.3b, and there is no difference in the strain-life behavior of LCF and cyclic creep tests at 600 °C. Thus, partitioning of the inelastic strain is not necessary in this case, since there is no difference in the lives from considering either plastic or creep damage.

From these findings, it is clear that strain is not a suitable indicator of damage in HiSiMo DCI at high temperatures. Other potential indicators include the maximum stress in Figure 5.4a or stress range in Figure 5.4b, both of which give poor correlation with the experimentally observed values of life. Furthermore, when the strain level or temperature is high, stress can give an imprecise measure of damage due to the flatness of the stress-strain curve as inelastic strain increases.

The Smith-Watson-Topper parameter P_{SWT} was proposed by *Smith et al.* (1970) to account for the mean stress which can effect the fatigue life. P_{SWT} has been successfully used to correlate the TMF life in a titanium aluminide alloy by *Heckel and Christ* (2010) and *Roth and Biermann* (2008), and in a vermicular cast iron by *Eichlseder et al.* (2008). The Smith-Watson-Topper parameter is given by

$$P_{SWT} = \sqrt{\sigma_{max} \frac{\Delta\varepsilon}{2}}. \tag{5.1}$$

where σ_{max} and $\Delta\varepsilon$ are cyclic quantities. The Smith-Watson-Topper parameter was calculated for the stabilized cycle for each test conducted on the HiSiMo DCI and the result is shown in Figure 5.5. While the value of P_{SWT} is underestimated for the critical OP TMF data that are inclusive of the embrittled temperature, P_{SWT} shows generally better correlation with the experimental values of fatigue life. The slope is moderate and the dispersion band is fairly narrow. Thus, the Smith-Watson-Topper parameter serves as a better indicator of damage than the other cyclic quantities considered. However, this parameter, which relies on the cyclic values of stress and strain, is not well-suited to implementation for complex loading histories. Further-

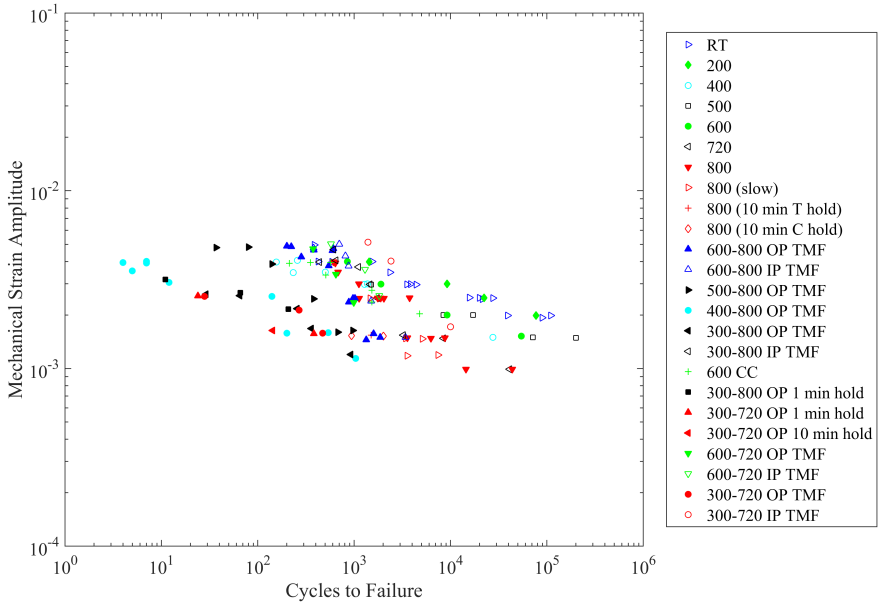

(a)

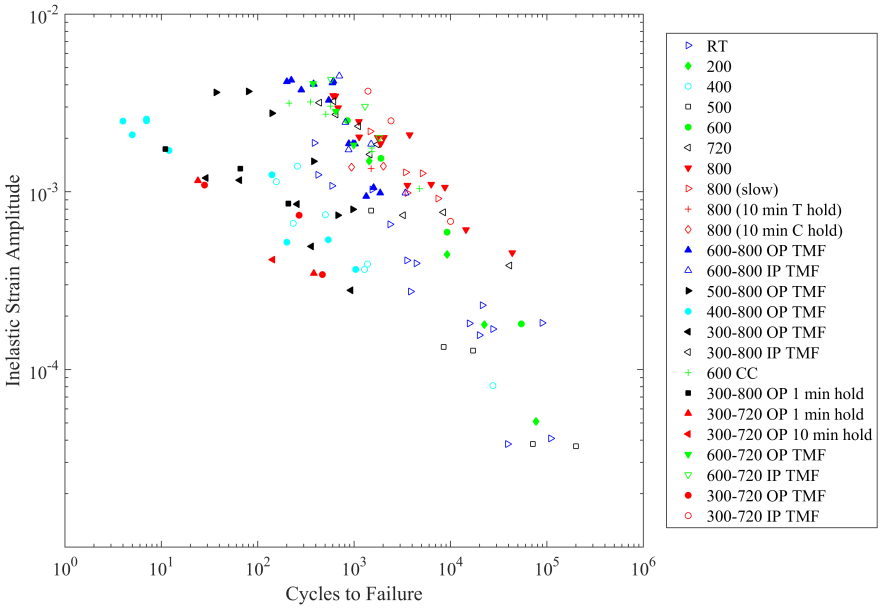

(b)

Figure 5.1: Plots of the (a) mechanical strain amplitude and (b) inelastic strain amplitude against measured life for all the uniaxial high temperature fatigue tests conducted on HiSiMo DCI.

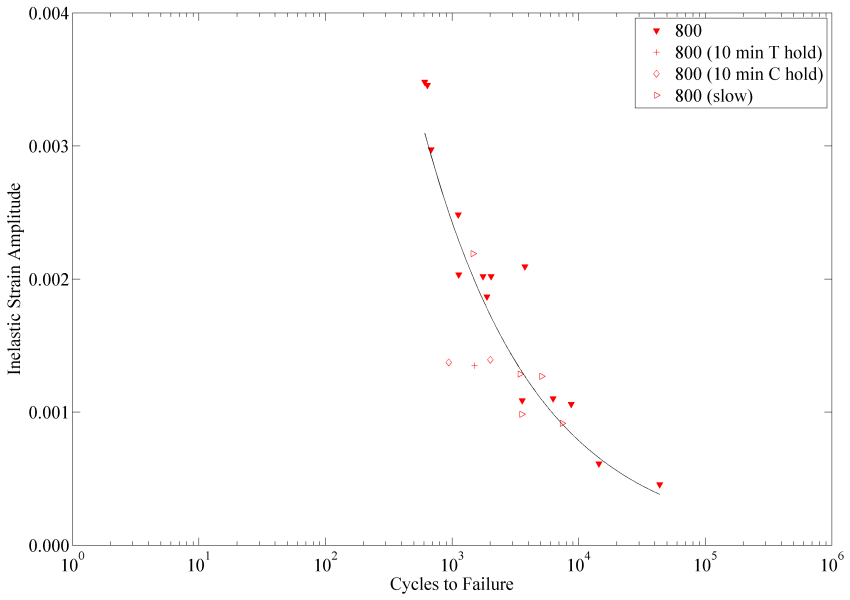

Figure 5.2: Coffin-Manson plot for LCF tests conducted at 800 °C at various strain rates and with hold times showing no difference in fatigue life.

more, since the stresses and strains develop in an anisothermal cycle in TMF, the damage accounted for by the maximum stress must considered relative to the strength of the material at the temperature where the maximum stress is experienced. This is not accounted for in the Smith-Watson-Topper parameter, and seriously reduces its utility in the case of TMF life prediction.

However, P_{SWT} did show better correlation with the TMF life than the other damage parameters considered. Recognizing that the multiplication of stress and strain give a measure of the strain energy dissipated by the material, an effort was made to determine an energy criteria that would be suitable for use with complex loading histories in a multiaxial formulation.

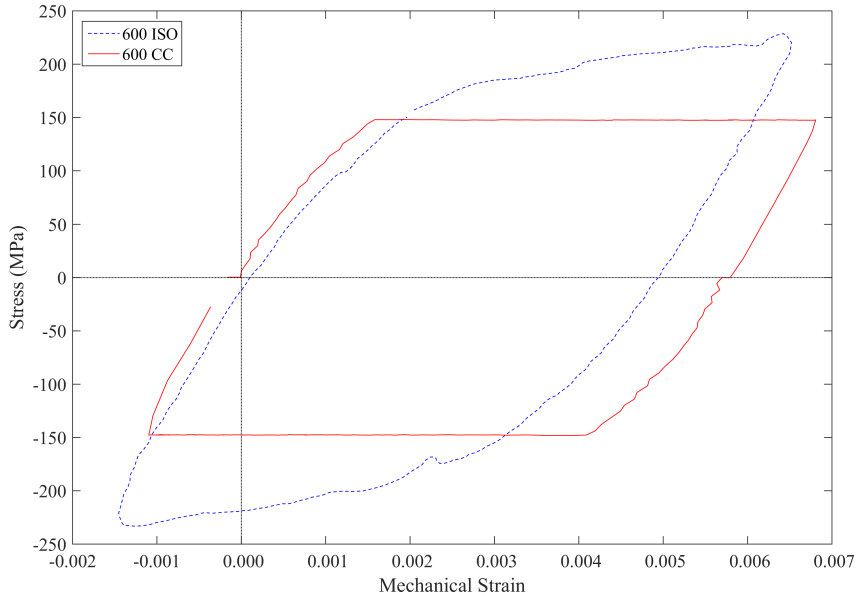

(a)

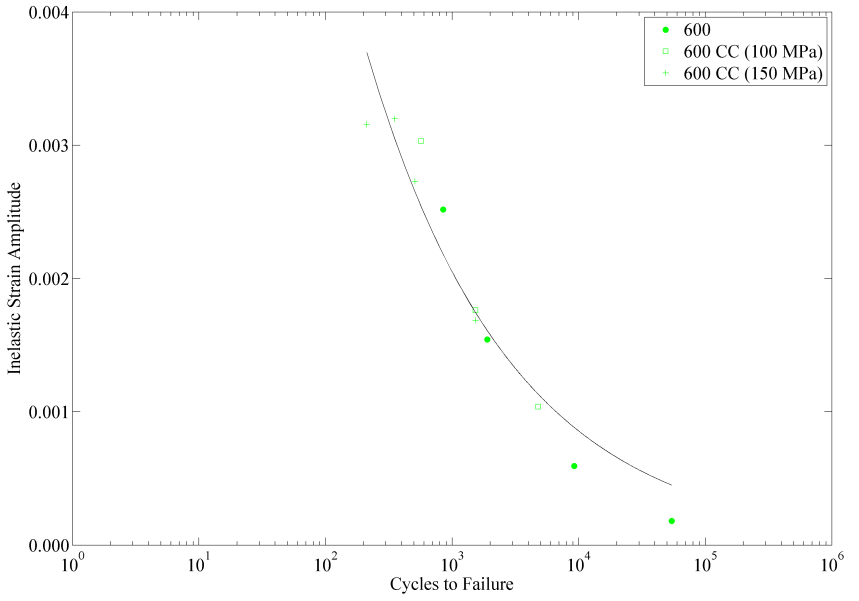

(b)

Figure 5.3: For isothermal tests conducted at 600 °C under LCF and cyclic creep; (a) a comparison of the stress-strain loops, and (b) the Coffin-Manson plots which show no difference in fatigue life.

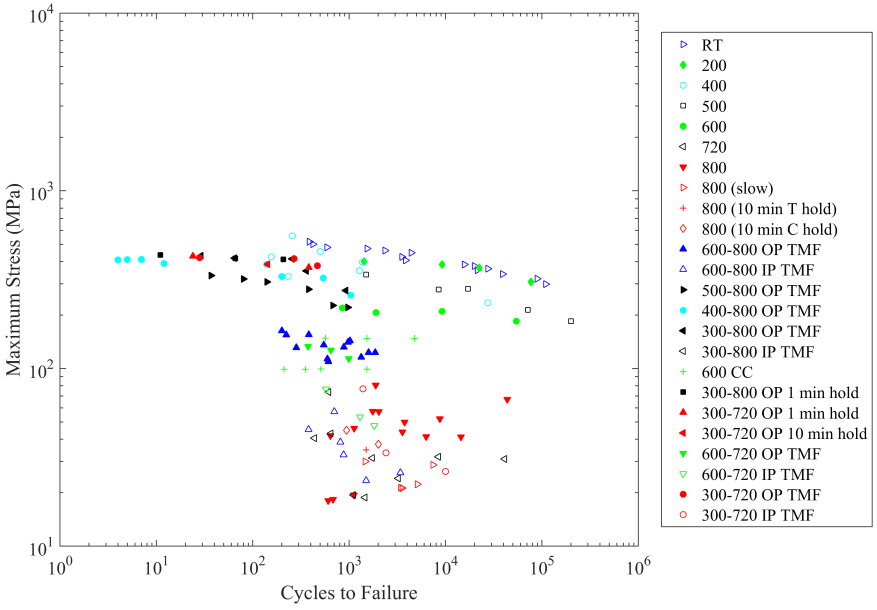

(a)

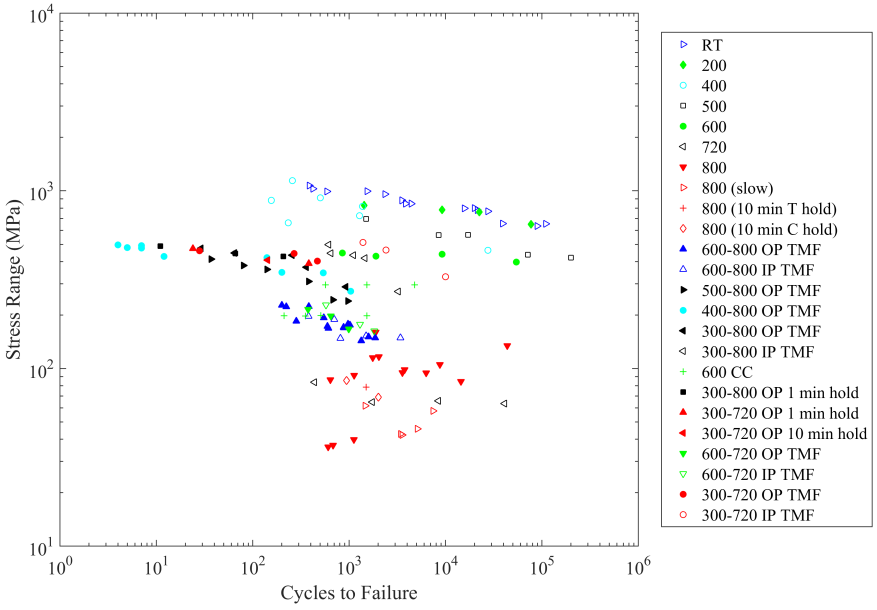

(b)

Figure 5.4: Plots of the (a) maximum stress and (b) stress range against measured life for all the uniaxial high temperature fatigue tests conducted on HiSiMo DCI.

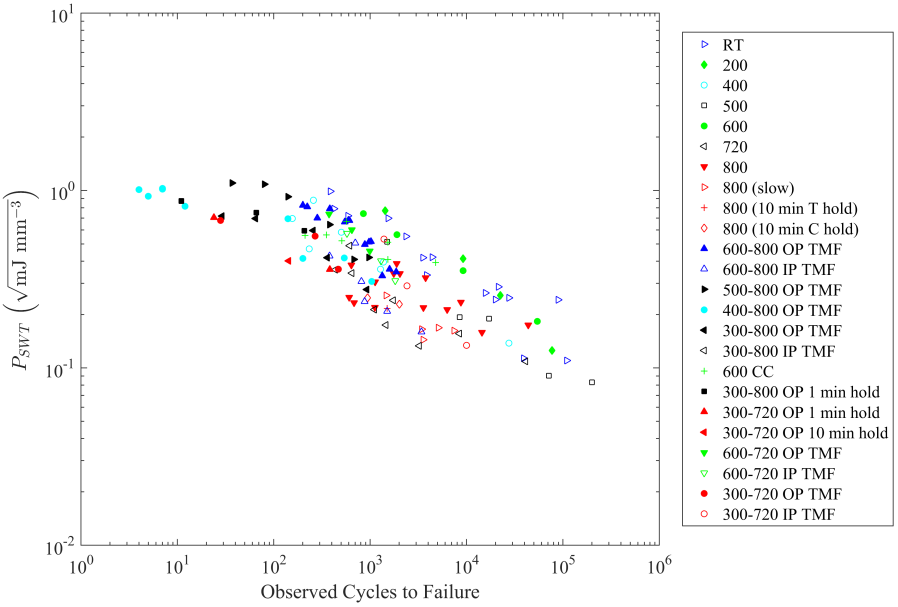

Figure 5.5: Plot of the Smith-Watson-Topper Parameter of the mid-life cycle against measured life for all the uniaxial high temperature fatigue tests conducted on HiSiMo DCI.

5.2 Background of Energy Approaches

Energy approaches precede many of the life prediction formulations employed in modern analysis techniques. The energy approach to fatigue life prediction is based on the physical understanding that when irreversible changes occur to a material, irrecoverable energy is dissipated. The amount of dissipated energy (regardless of the type of system or energy) can be quantified from the hysteresis behavior between the input and output states of the process that causes the irreversible change. In materials, some sources of hysteretic energy dissipation include ferromagnetism, ferroelectricity, phase changes, elastic and plastic deformation, and viscous behavior.

Inglis (1927) first discovered the connection between cyclic fatigue damage and the total energy dissipated by the stress-strain hysteresis behavior of a low carbon steel subjected to rotating bending stresses. *Hanstock* (1947) later proposed a measure of total energy dissipation in a fatigue cycle which consists of a damaging part that

contributes to fracture, and a non-damaging part that did not contribute to the fracture process. *Enomoto* (1955) advanced the hypothesis by proposing the existence of a critical value to which damaging energy must accumulate to cause failure.

Feltner and Morrow (1961) postulated that a constant total amount of *plastic* strain energy is required to cause fatigue failure, and that inelastic, non-recoverable, strain would contribute to fatigue failure. The authors assumed that the strain energy dissipated by a specimen via plastic strain hysteresis would increase with each cycle until the capacity of the material to convert damaging energy was exceeded, at which time fracture would occur (*Feltner and Morrow*, 1961). The capacity of the material was considered to be approximately constant, and the maximum amount of cyclic plastic strain energy dissipated, W_{in}, that could be converted was equivalent to the strain energy dissipated to fracture in a static tension test, U. The strain energy dissipated by a specimen via plastic strain hysteresis was then written as

$$W_{in} = \oint \sigma d\varepsilon_{in} \approx U \tag{5.2}$$

where σ is the applied stress and $d\varepsilon_{in}$ is the increment of plastic strain range. *Ostergren* (1976) introduced a measure of tensile energy by assuming the fatigue crack can initiate only under tensile loading, and compressive loads neither advance nor heal the crack. The Ostergren Energy (also in Equation 4.5 of Chapter IV) is

$$W_T = \oint \alpha \left(\sigma - \sigma_o\right) \, d\varepsilon_{in}. \tag{5.3}$$

Energy-based methods have shown difficulty to handle a wide range of loading scenarios which can be encountered by real components, including stress holds, compressive holds and varying sensitivity to waveform (*Manson and Halford*, 2009). Furthermore, since energy methods require that a material be fairly cyclically stable to bring a strong predictive capability, they lack ease of use for cases where the hysteresis

loop changes with time. However, they are strongly appealing for their simplicity and straightforward implementation for multiaxial cases.

5.2.1 Application of Energy Approaches to High Temperature Fatigue

Many authors have attempted to use energy dissipation as a measure of isothermal and anisothermal fatigue damage. As emphasized by *Thomas et al.* in a 2004 review of the state-of-the-art of thermomechanical fatigue design and life prediction methods, the use of energy dissipation per cycle overcomes the limitations of classical methods which rely on maximal and minimal values of the fatigue cycle, which occur at different temperatures in TMF loading. The energy dissipation approach has three primary advantages for anisothermal loading of components:

1. The energy dissipation can be easily generalized to multiaxial situation,
2. The method of determining energy dissipation is independent of the temperature and therefore allows calculations with anisothermal loading, and
3. The energy dissipated in each cycle is representative of the cyclic behavior of materials.

Skelton (1991) notably applied the strain energy density to predict fatigue life for high temperature low cycle fatigue with the assumption that the volume element ahead of the crack tip will fail when a threshold energy is accumulated, and that the rate of energy dissipation can be related to the bulk fatigue behavior of a material. The method was later revised to predict the thermomechanical fatigue life from the isothermal hysteresis loops for a wide range of phasings for nickel-based (*Skelton et al.*, 2000) and Cr-Mo alloys (*Skelton*, 2004).

The use of energy for anisothermal thermomechanical fatigue loadings was expanded by *Charkaluk and Constantinescu* (2000; 2002) and *Constantinescu et al.* (2004), who utilized the stabilized plastic strain energy criteria to predict the anisothermal fatigue life of a SiMo cast iron manifold. It should be noted that *Charkaluk and*

Constantinescu (2000) observed a loss of LCF life at 350 and 400 °C where the embrittlement mechanism is active, but did not explicitly account for it in the fatigue life prediction. Instead, the loss of fatigue life was attributed to the so-called dynamic strain aging of cast irons that was reported by *Bastid* (1995) under conditions of static loading. The fatigue life was consequently over-predicted at these temperatures (*Charkaluk and Constantinescu*, 2000). Similarly, *Lederer et al.* (2000) related the thermomechanical fatigue life of a nodular cast iron to the accumulated dissipated plastic strain energy with good correlation for isothermal results, although thermal fatigue results in the temperature range of ambient to 700 °C were slightly non-conservative.

Various researchers have proposed methods to refine the prediction of damage by partitioning the strain energy into its elastic and plastic components (*Nissley*, 1995; *Christ*, 2007), and applying the partitioned strain energy to the growth of short and long fatigue cracks (*Miller et al.*, 1993; *Maurel et al.*, 2009). *Korsunsky et al.* (2007) compared the macroscopic and microscopic energy dissipation criteria to classical fatigue life criteria and found that both measures of energy dissipation compared well with other established parameters for isothermal loading cases. Still others have implemented modification factors based on frequency (*Nagesha et al.*, 2009), observations of monotonic hysteretic energy (*Lee et al.*, 2008), peak cyclic tensile stress and strain (*Huang et al.*, 2006), or mean stress *Gocmez et al.* (2010). *Gosar and Nagode* (2012) applied a Prandtl-type operator to give an analytical estimate of the rate-independent hysteretic energy of a thermomechanical cycle.

5.3 Modeling Framework

The present study attempts to apply the energy approach to the thermomechanical fatigue of HiSiMo DCI by building on the work of *Charkaluk and Constantinescu* (2000) and *Lederer et al.* (2000). In the dissertation, a more comprehensive range of

test conditions is considered, and modifications on the method are implemented to account for the effect of intermediate temperature embrittlement. The operation of real components dictates the importance of obtaining an accurate life prediction for thermal cycling through 400 °C where the embrittlement is active, and so an accurate representation of the accumulated damage must be determined.

The inelastic strain energy dissipation is first calculated for the HiSiMo DCI considered in the dissertation work. The inelastic strain energy dissipated W_{in} was calculated by integrating the stress and inelastic strain over the stress-strain loop as

$$W_{in} = \oint \sigma d\varepsilon_{in}. \tag{5.4}$$

The inelastic strain energy is plotted against the observed fatigue life in Figure 5.6. The slope of the data is comparable to that given by the Coffin-Manson plot, which indicates the potential for good sensitivity of the fatigue life to changes in the inelastic strain energy dissipation. While the dispersion band is nearly the same as that obtained from the inelastic strain amplitude, there is less distinction between the bands of embrittled and non-embrittled data through consideration of the inelastic strain energy. Most importantly, however, the strain energy dissipation was integrated over the entire anisothermal cycle, which allows consideration of the changing capacity of the material to dissipate energy.

The relation between the inelastic strain energy dissipation and the fatigue life is given by

$$W_{in} = \oint \sigma d\varepsilon_{in} = W_f \left(2N_f\right)^m \tag{5.5}$$

where W_f is a temperature-dependent coefficient that represents the net ability of the material to dissipate energy in a fatigue or TMF cycle. W_f is also the intercept of the strain energy-life curve. Given that the fatigue data in Figure 5.6 have approximately the same slope, it is clear that the value of the ordinate intercept, W_f, will vary based

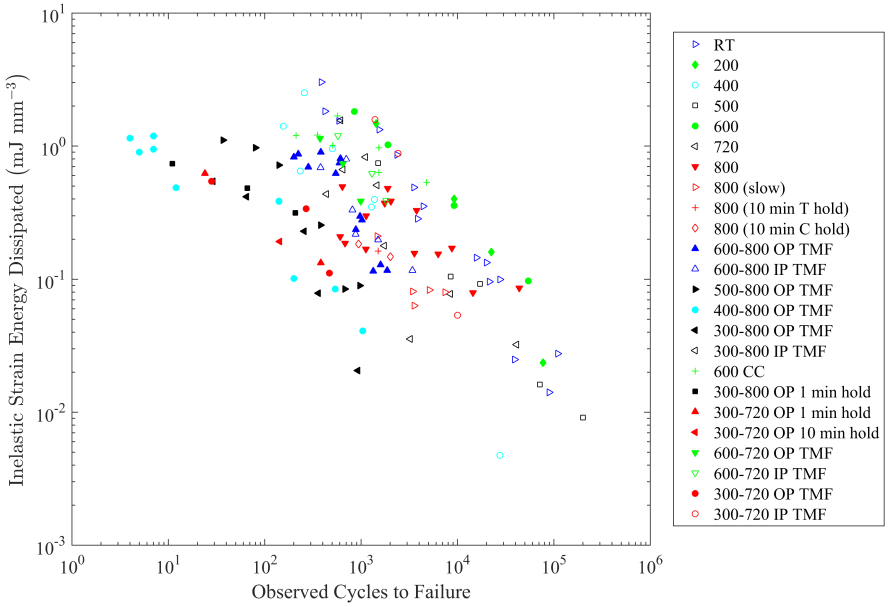

Figure 5.6: Plot of the inelastic strain energy dissipated in the mid-life cycle against measured life for all the uniaxial high temperature fatigue tests conducted on HiSiMo DCI.

on the test temperature, the limits of the thermal cycle, and the TMF phasing (which is related to the temperature at which the strain energy is dissipated). It is important to note that, since changing the proportions of creep and plastic damage in the cycle do not affect the fatigue life for this material, W_f will not additionally vary with strain rate.

The ability of the material to dissipate strain energy will be well-represented by W_f, with consideration only of temperature. Therefore, W_f is not constant over an anisothermal cycle, and it is taken inside the integral of Equation 5.5 to become

$$\oint \frac{\sigma d\varepsilon_{in}}{W_f} = (2N_f)^m \tag{5.6}$$

To develop a useful model which can correctly interpret a value for W_f that accounts for the effect of embrittlement, recall from Chapter III that the 400 °C embrittlement reduces the ability of the material to undergo plastic tensile deformation when the

temperature is near 400 °C. When a compressive stress is present near 400 °C, the embrittlement does not serve to reduce the ability of the material to dissipate inelastic strain. This idea is similar to the approach taken by *Wu et al.* (2015), wherein the authors accounted for the effect of embrittlement as it reduced the fracture toughness of the material near 400 °C. The observed value of W_f then implicitly includes the effect of embrittlement when the temperature is near 400 °C, and represents the weighted-averaged ability of the material to dissipate tensile and compressive strain energies. To further develop a description of damage in HiSiMo DCI which accounts explicitly for embrittlement, it becomes necessary to distinguish between the apparent tensile and compressive capacities of the material. Thus, Equation 5.6 is rewritten as

$$\oint \frac{\sigma d\varepsilon_{in}}{W_f} = \int\limits_{tensile} \frac{\sigma d\varepsilon_{in}}{W_f^T} + \int\limits_{compressive} \frac{\sigma d\varepsilon_{in}}{W_f^C}. \tag{5.7}$$

where W_f^T and W_f^C are similar in meaning to W_f, and represent the ability of the material to dissipate inelastic strain energy in tension and compression, respectively. A higher value of the parameter indicates a greater capacity to dissipate strain energy. Both W_f^T and W_f^C are temperature dependent.

Since the ability of the HiSiMo DCI is reduced by embrittlement only for tensile stresses, with the greatest reduction occurring near 400 °C, W_f^T should be at a minimum when the temperature is near 400 °C. However, W_f^C should decrease only monotonically with temperature, since the embrittlement does not reduce the ability of the material to dissipate compressive inelastic strain energy. It is important to note that when the temperature is much higher or lower than 400 °C such that the embrittlement is not affecting the material, W_f^T and W_f^C should be nearly equivalent. This is substantiated by comparison of the IP and OP TMF life for thermal cycles in the range of 600 to 800 °C where the embrittlement is not active. Revisiting Figure 3.5 in Chapter III, it is clear that the OP loop for 600 to 800 °C dissipates roughly

the same amount of strain energy due to a tensile stress as the IP loop dissipates due to a compressive stress. The total area of the loops, which gives the strain energy dissipation per cycle, is similar for both phasings, and the TMF life is similar for both phasings. Thus, when the embrittlement is not active, the HiSiMo DCI can dissipate a similar amount of energy under tensile or compressive loads prior to failure. W_f^T and W_f^C are related according to

$$W_f^T < W_f^C \text{ when } T \approx 400, \text{ and}$$
$$W_f^T \approx W_f^C \text{ when } T \gg 400 \text{ or } T \ll 400.$$

Furthermore, when the embrittlement is not active, the values of W_f^T and W_f^C can be determined directly from a fully-reversed isothermal test where

$$W_f^T \approx W_f^C \approx W_f \text{ when } T \gg 400 \text{ or } T \ll 400.$$

Since W_f^C is not affected by the embrittlement at any temperature, a temperature-dependent variable, Θ is introduced to relate W_f^T to W_f^C:

$$W_f^T = \frac{W_f^C}{1 + \Theta(T)} \tag{5.8}$$

where Θ is a continuous function of temperature that is zero when the temperature is far from 400 °C, and greater than zero when the temperature is near 400 °C. Substituting Equations 5.8 and 5.7 into Equation 5.4 and rearranging yields

$$\oint \frac{\sigma d\varepsilon_{in}}{W_f} = \int_{tensile} \frac{(1+\Theta)\,\sigma d\varepsilon_{in}}{W_f'} + \int_{compressive} \frac{\sigma d\varepsilon_{in}}{W_f'} \tag{5.9}$$

where W_f' is measured from the isothermal, fully-reversed tests for temperatures where the embrittlement is not active, and is interpolated between measured values for tem-

peratures where the embrittlement would significantly influence the direct measurement. Recognizing that Equation 5.9 integrates the energy over the entire cycle, and that both the tensile and compressive terms are normalized by the same coefficient, Equation 5.9 can be simplified as

$$\oint \frac{\sigma}{W_f} d\varepsilon_{in} = \oint \frac{\sigma + \Theta\{\sigma\}}{W'_f} d\varepsilon_{in} \tag{5.10}$$

where the Macaulay brackets $\{\}$ describe the function

$$\{x\} = \begin{cases} x & \text{when } x \geq 0, \\ 0 & \text{when } x < 0. \end{cases} \tag{5.11}$$

Substituting the modified term for the inelastic strain energy back into the fatigue life relationship in Equation 5.5 yields

$$\oint \frac{\sigma + \Theta\{\sigma\}}{W'_f} d\varepsilon_{in} = (2N_f)^m \tag{5.12}$$

where $W'_f = W_f$ for temperatures where the embrittlement is not active.

The variable Θ in Equation 5.12 must have a maximum, positive value when the temperature is near 400 °C to correctly account for the reduction in the ability of the material to dissipate the inelastic strain energy. Elsewhere, the value of Θ should be zero. Θ is assigned a temperature-dependent function of the form

$$\Theta(T) \ = \alpha \ exp\left[-\beta \left(\frac{T_{emb} - T}{T_{emb}}\right)^2\right] \tag{5.13}$$

where α is an empirical constant that controls the magnitude of the reduction in toughness due to embrittlement, and β is an empirical parameter that controls the temperature range over which the embrittlement is damaging. Note that this function represents a symmetric normal distribution that is a maximum at T_{emb}. Since

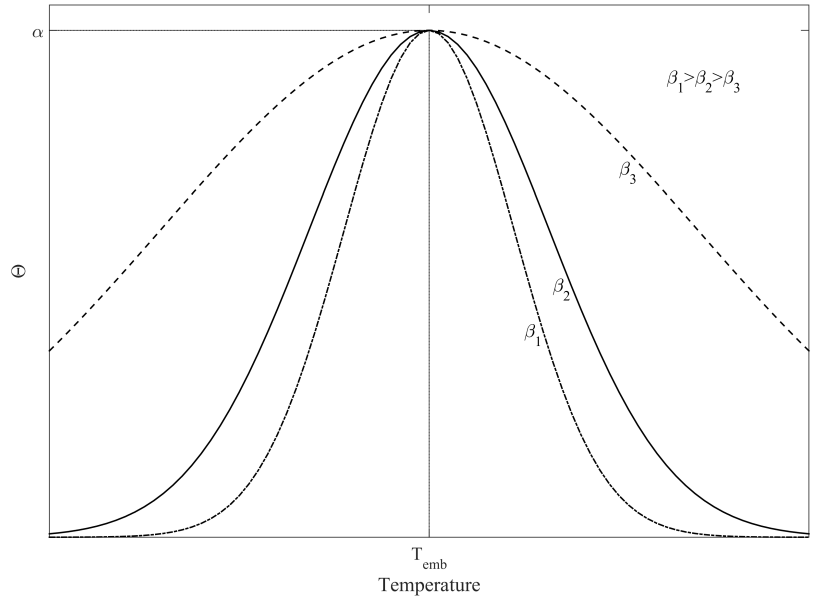

Figure 5.7: Plot of Θ represented by a symmetric normal distribution of temperature for different values of β.

Kobayashi et al. (1998) found that the temperature of maximum embrittlement can vary with strain rate and alloy composition, T_{emb}, the temperature of maximum embrittlement, is left as a parameter which must be defined in Equation 5.13. The value that $\Theta(T)$ assumes as a function of temperature is shown schematically in Figure 5.7 for different values of β.

The modified inelastic strain energy dissipation criterion given by Equation 5.12 has only four parameters that must be experimentally determined, and they are W_f', T_{emb}, α and β. It is important to reiterate that W_f' can be determined directly from cyclic fatigue tests where $\Theta \approx 0$, and is interpolated when $\Theta > 0$.

5.4 Application to Uniaxial Fatigue and TMF Tests

The modified inelastic strain energy dissipation criterion given in Equation 5.12 was applied to the more than 120 uniaxial high temperature and thermomechanical

fatigue data generated for HiSiMo DCI. The parameter

$$\oint \frac{\sigma + \Theta(T)\ \{\sigma\}}{W_f'(T)} d\varepsilon_{in} \tag{5.14}$$

was calculated from the stabilized stress-inelastic strain loop for each test. The value of W_f' is shown schematically in Figure 5.8. Please note that the ordinate scale is presented without values to protect the proprietary information of Ford. T_{emb} was assigned a value of 400 °C, though the actual temperature of the maximum embrittlement effect may be slightly higher or lower for this alloy. The value of β was adjusted to achieve the best correlation with the physical observations of temperature-dependent embrittlement damage. The value of β used in the life prediction resulted in nearly zero embrittlement damage for temperatures greater than about 550 °C and less than about 250 °C. This range of active temperatures, and the implied extent of embrittlement damage, is in good agreement with fractographic observations of specimens tested under isothermal fatigue at 200, 400, 500 and 600 °C. The parameter α was optimized for the entire dataset of more than 120 high temperature and thermomechanical fatigue tests, including varying strain rates and tests with hold times. The optimization process minimized the error between the predicted and observed fatigue lives where the error was previously defined in Equation 4.14.

The modified inelastic strain energy dissipation criterion is plotted against the observed fatigue life in Figure 5.9. The parameter shows good correlation with the observed fatigue lives for all conditions. In particular, good correlation is shown for the OP TMF tests including the embrittled temperature for which the Neu-Sehitoglu model over predicted the fatigue lives.

Finally, a fatigue life prediction was made for the uniaxial tests using the modified inelastic strain energy dissipation parameter according to Equation 5.12. The slope of the relationship, given by exponent m was found to be independent of temperature

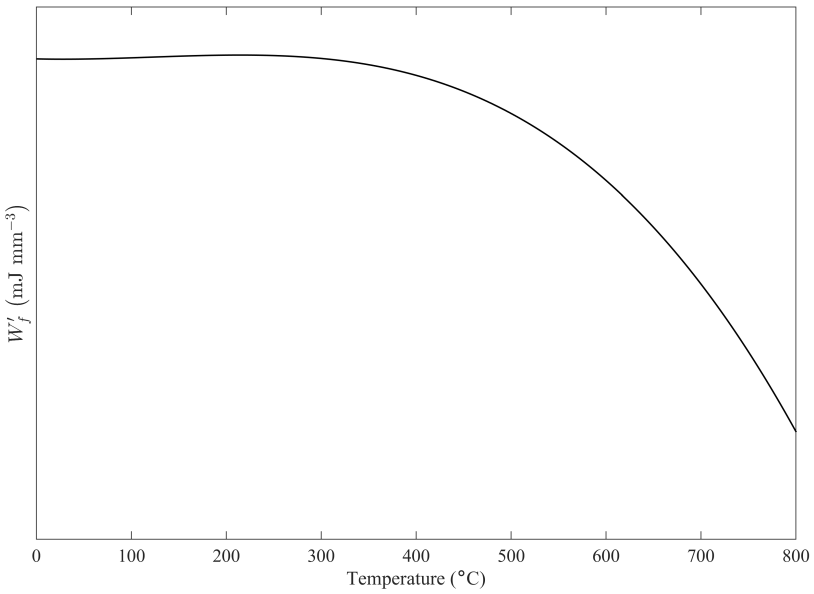

Figure 5.8: Schematic illustration of W_f' as a function of temperature. Please note that the ordinate scale is presented without values.

or test type, and a value was selected based on the data correlation presented in Figure 5.9. The comparison between predicted and observed fatigue lives is shown in Figure 5.10. Good correlation is seen between the predicted and measured lives, with 65 % of tests falling within a factor of two of the observed life, and 95 % of tests falling within a factor of five of the observed life (as represented by the solid lines in Figure 5.10).

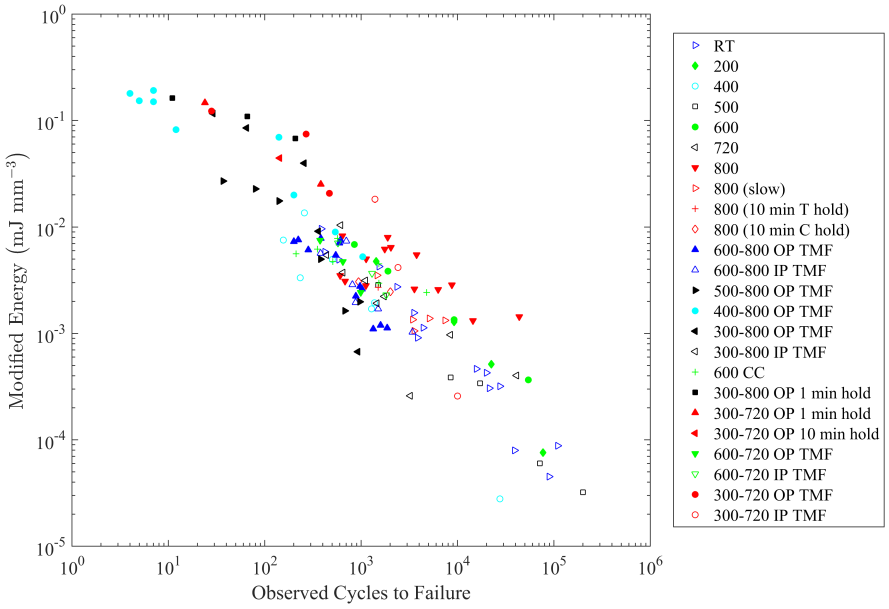

Figure 5.9: Modified energy dissipation criterion applied to the mid-life cycle as compared to the elevated temperature fatigue and TMF tests of HiSiMo DCI.

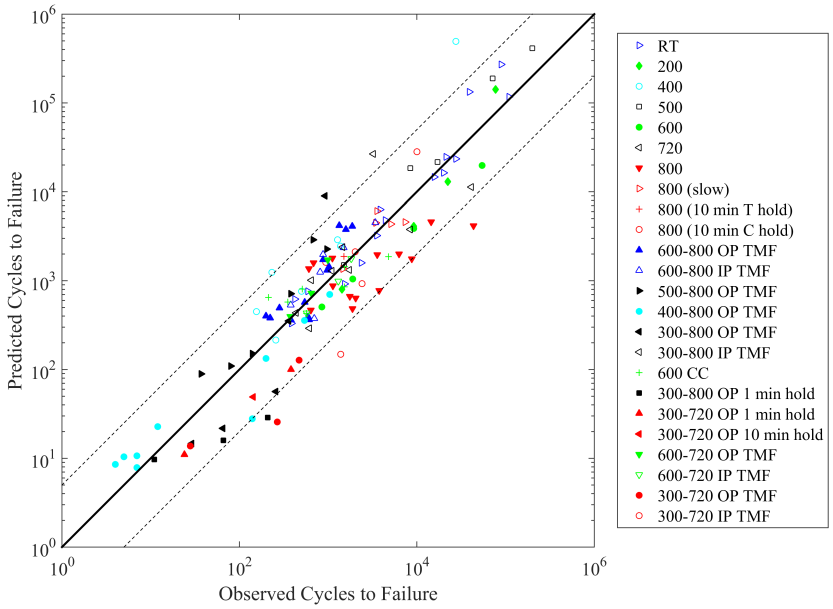

Figure 5.10: Comparison of the life predicted by the modified energy dissipation criterion and the measured life. Band is 5x.

5.5 Application to TMF Life Prediction of Exhaust Manifold Component

The modified inelastic strain energy dissipation framework was then applied to predict the TMF life for an exhaust manifold subjected to a complex thermal cycling history. The physical manifold was subjected to thermal cycles in a dynamometer test which was intended to simulate a severe use case. This manifold was constructed from the same HiSiMo alloy considered in the dissertation work. It suffered catastrophic failure after 12 thermal cycles. The primary crack location is shown in Figure 5.11. This crack propagated through the entire thickness of the manifold wall during the test, causing an exhaust gas leak. The test was stopped when the leak was detected. Upon closer examination, several other small cracks were found which started at the outer wall of the exhaust manifold. The locations of the additional cracks are indicated in Figure 5.12.

(a)

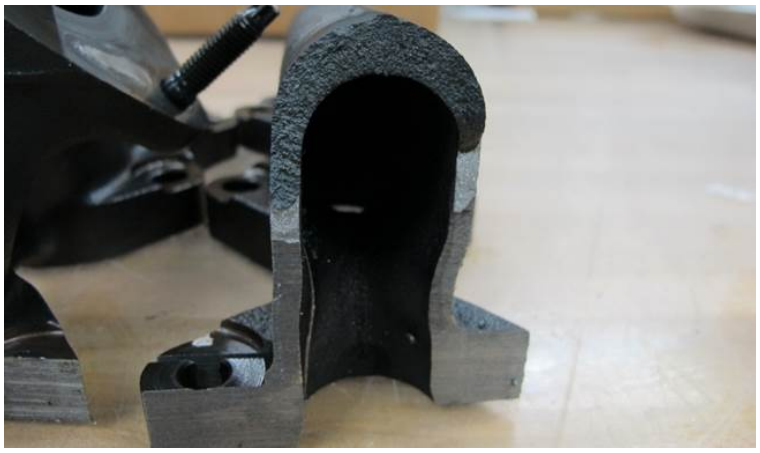

(b)

Figure 5.11: (a) Through-crack detected in a cast manifold due to the application of severe thermal cycles. (b) Fracture surface of the through-thickness crack.

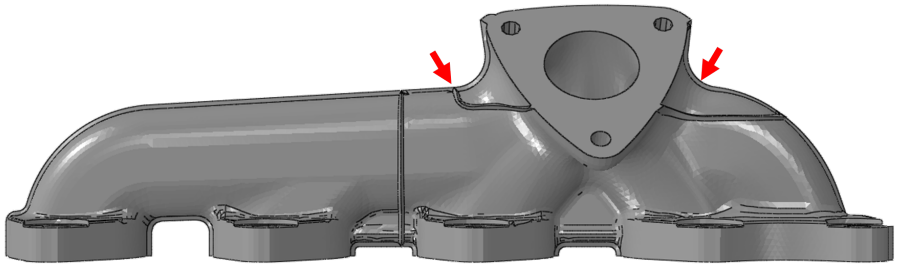

(a)

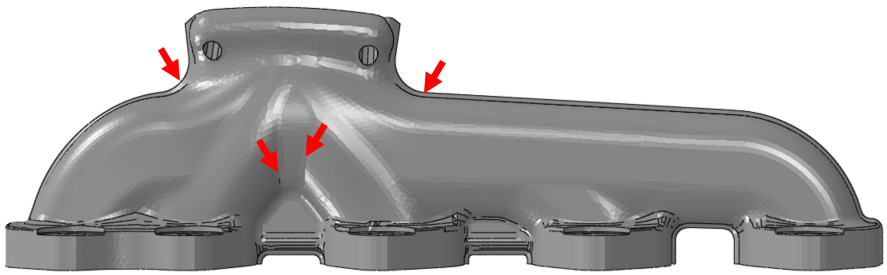

(b)

Figure 5.12: Locations of additional cracks detected upon examination of the exhaust manifold from (a) the top view and (b) the bottom view.

5.5.1 Transient Thermal Analysis

A transient thermal heat transfer analysis was conducted with Abaqus. The temperature distribution at the interior of the manifold wall was determined by a computational fluid dynamics (CFD) analysis of the exhaust gas flow through the manifold. Thermal boundary conditions for the heat transfer analysis included the forced convection of exhaust gas on the internal surface of the manifold, natural convection on the outside surfaces, and conduction through thermal contact with the cooled cylinder head. The thermal analysis simulated five cycles of the dynamometer test. The resulting temperature history at a node located near the critical location from the physical test is shown in Figure 5.13. During a heat-up and cool-down cycle, the manifold can experience temperatures as high as 753 °C at the critical location, and as low as 67 °C. It is clear from Figure 5.13 that the material is initially heated very quickly in each cycle. The resulting temperature profile of the manifold indicates the severity of the transient thermal gradients to which the manifold is subjected as a result of the cyclic application of temperature. The profile is shown in Figure 5.14 at the start and end of the heat-up cycle.

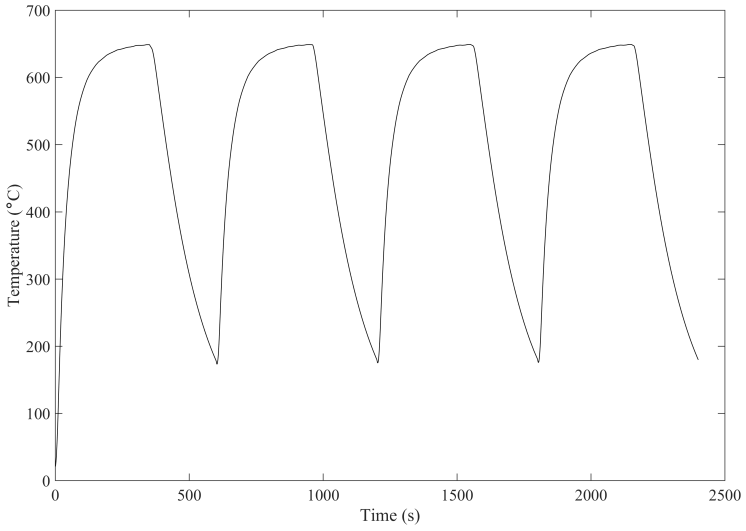

Figure 5.13: Temperature history at a critical node.

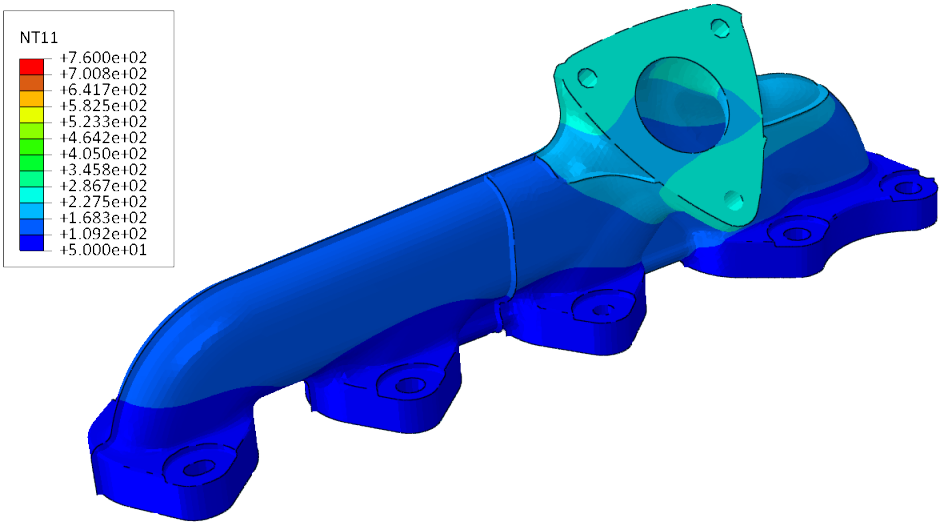

(a)

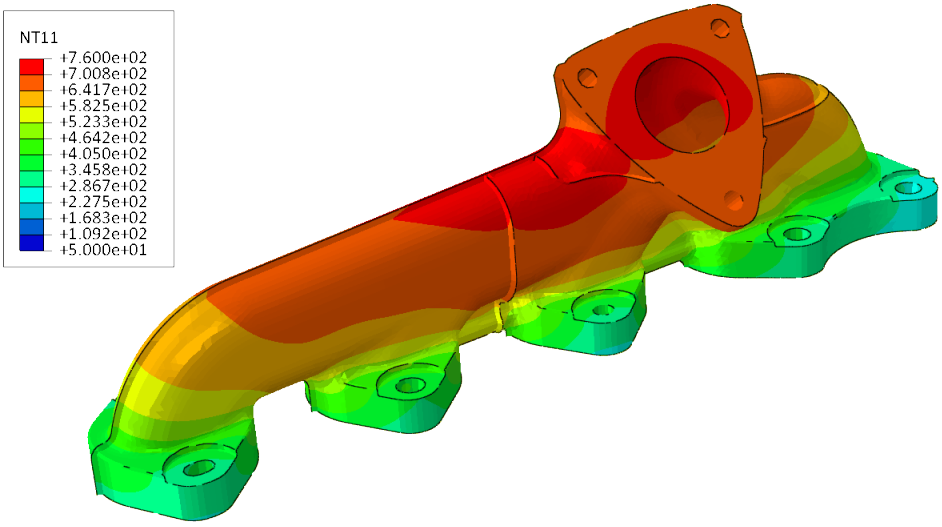

(b)

Figure 5.14: Temperature profile at (a) the start and (b) end of the heat-up cycle.

5.5.2 Stress-Strain Analysis

The applied temperature fields result in thermally-generated mechanical strains due to the thermal expansion of the material. To determine the stresses and strains which result from the cyclic application of temperature, a stress-strain analysis was then conducted in Abaqus using the temperature field generated from the heat transfer analysis. The material model that was used in the analysis was that proposed by *Chaboche* (1989), which accounts for the temperature- and strain-rate dependency of viscoplastic behavior in a material. The constitutive model was implemented as a user subroutine (UMAT) in Abaqus. The implementation and fitting of the parameters is described in more detail by *Mao et al.* (2015). The model parameters were determined for HiSiMo DCI from isothermal cyclic tests under various combinations of temperature and strain rate. Figure 5.15 shows a comparison of the experimental, isothermal stress-strain loops at various strain rates with those fitted by the Chaboche constitutive model.

The transient temperature field was applied as a field input at each node for the stress-strain analysis. Additional boundary conditions simulated the bolted connections to the cylinder head and turbocharger housing through use of friction and surface contact. The distribution of stresses and strains was calculated over five thermal cycles to obtain the stabilized transient response of the manifold. To illustrate the magnitude and distribution of the stresses that result from the application of temperature via the exhaust gas, Figure 5.16 shows the von Mises stress distribution after cooling. It is important to note that the locations of the Mises stresses do not coincide with the critical crack location.

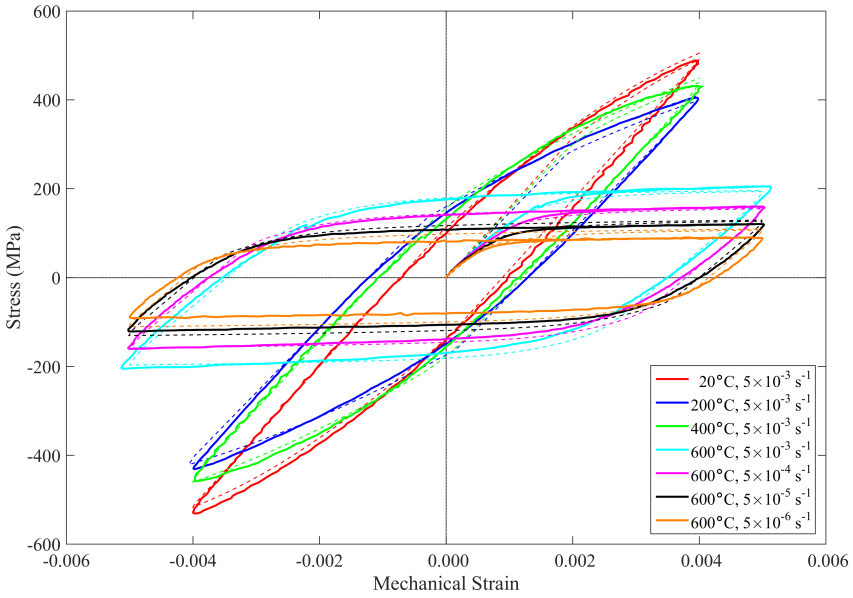

(a)

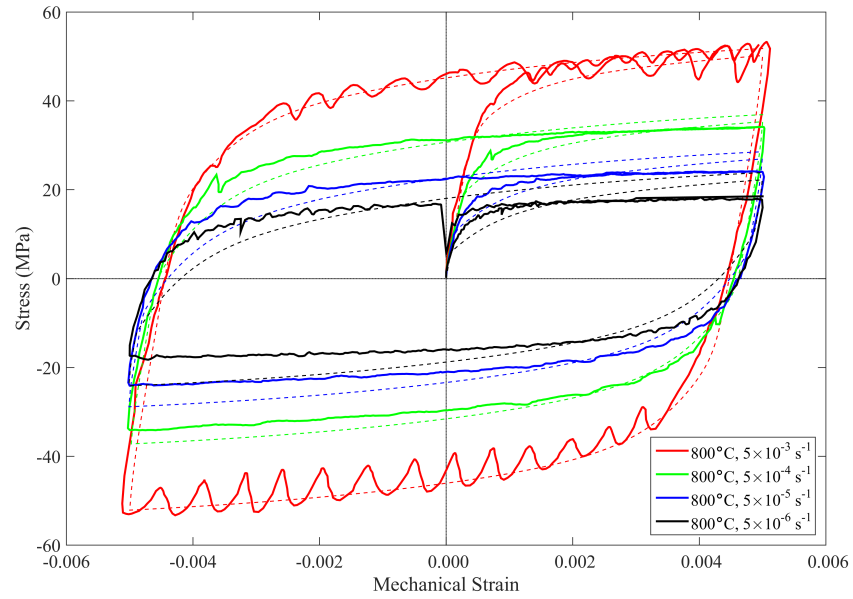

(b)

Figure 5.15: Comparison of the experimental stress-strain loops compared to the fitted Chaboche constitutive model for (a) room temperature up 600 °C, including loops at different strain rates, and (b) 800 °C at different strain rates.

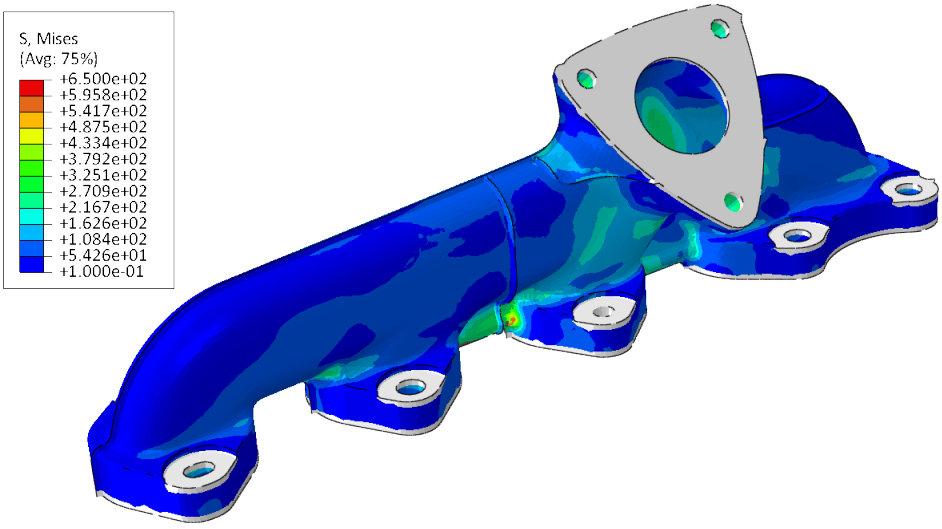

(a)

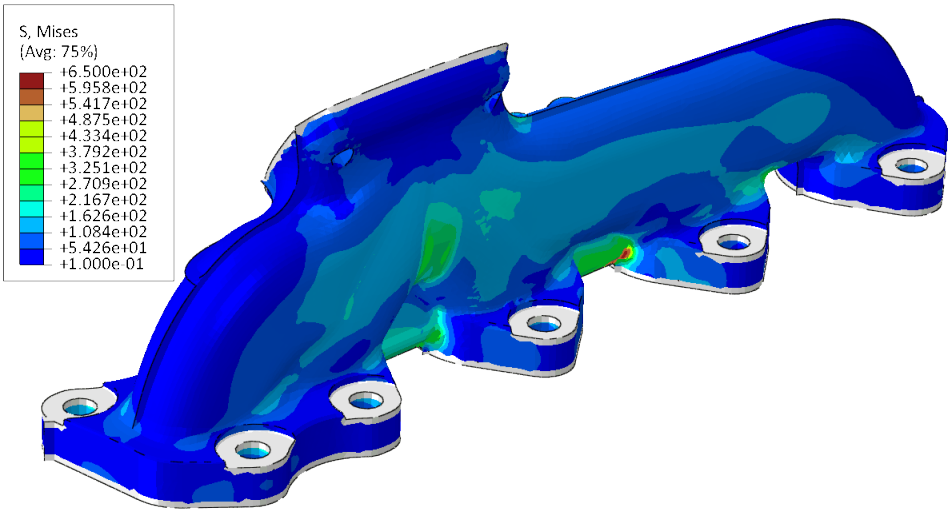

(b)

Figure 5.16: Von Mises stress distribution at the end of a thermal cycle at the (a) top and (b) bottom of the manifold.

5.5.3 Damage Calculation and Life Prediction

The TMF damage was then calculated by the modified inelastic strain energy dissipation model proposed in Chapter IV. A multiaxial formulation of Equation 5.12, given by

$$\oint \frac{\sigma_{ij} + \Theta(T)\{\sigma_{ij}\}}{W_f'(T)} d\varepsilon_{ij}^{in} = (2N_f)^m \tag{5.15}$$

where each component of stress and strain is given by ij for $i, j = 1, 2, 3$, was implemented in Fortran. A numerical integration procedure was used to the find the total modified inelastic strain energy dissipated over the stabilized thermal cycle due to the thermally-generated stresses and strains. The coefficients for the damage model are the same as those determined for the uniaxial tests in Chapter IV. The TMF life was calculated at each node, and the distribution of the predicted TMF life is shown in Figure 5.17. The critical location, where the shortest TMF life was predicted, is shown at location "A". This location is in excellent agreement with that observed from the physical test. Furthermore, the TMF life predicted at this location is only 27 cycles, which is in good agreement with the observed number of cycles to failure. The other crack locations in the physical manifold were also highlighted as critical locations by the modified inelastic strain energy dissipation model. The number of cycles to failure predicted at each location is shown in Table 5.1. The magnitude of the predicted TMF lives are appropriate when considering the extent of each crack when the physical test was halted.

Table 5.1: TMF life predicted at the critical locations by the modified inelastic strain energy dissipation model.

Location	**Predicted Cycles to Failure**
A	27
B	30
C	35
D	41

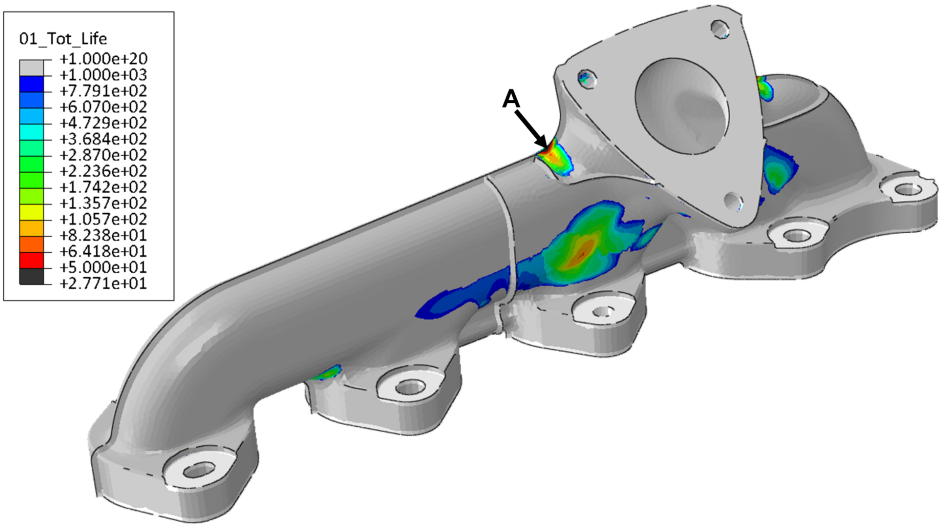

(a)

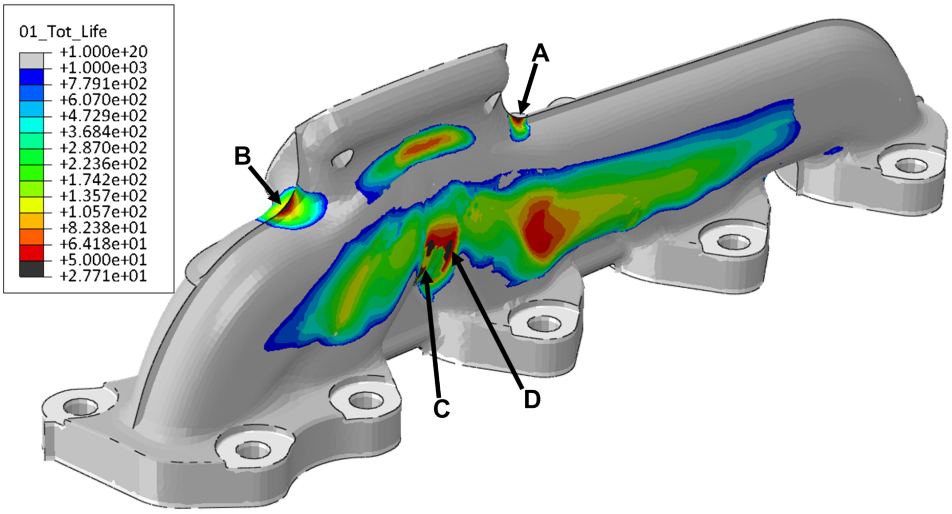

(b)

Figure 5.17: Distribution of TMF life predicted by the modified inelastic strain energy dissipation for the exhaust manifold as seen in the (a) top and (b) bottom views.

5.6 Potential Limitations of the Proposed Model

The modified inelastic strain energy dissipation criterion developed in the dissertation work shows good agreement with uniaxial tests conducted on the elevated temperature and thermomechanical fatigue of HiSiMo DCI, including LCF, cyclic creep, tests with slow strain rates, IP and OP TMF for varying minimum and maximum temperature, and isothermal and TMF tests with a hold time. Such an extensive experimental correlation has not been found in the literature for a HiSiMo alloy. The wide range of experimental data which the model was been able to represent the fatigue life of HiSiMo DCI suggests that it is a fairly general model of elevated temperature damage in this material. However, some comments must be made on the to address potential limitations of the method.

5.6.1 Determination of Parameters

The measurement and interpolation of W_f', and the determination of m, α and β, present some challenge since the values must be established empirically. In the dissertation work, extensive isothermal and anisothermal tests were conducted which facilitated the determination of the parameter values. However, it is worthwhile to estimate the minimum conditions which should be experimentally tested to inform the values of W_f', β, and m. Ideally, few experimental tests would be needed for any method employed in an industry setting.

In the dissertation work, the range of temperatures where the embrittlement was active was determined from tensile tests conducted at increments of 100 °C and simple observation of the stress-strain behavior. As reported by *Kobayashi et al.* (1998), the temperature of maximum embrittlement can vary with strain rate and alloy composition. However, it is well-established by various authors that the embrittlement occurs near 400 °C. Thus, by performing tensile tests over a narrower range of temperatures centered at 400 °C, it would be possible to more accurately determine the range of

temperatures where embrittlement is active for a particular alloy. This should inform the value of β, and will give the range of temperatures where W_f' should be interpolated.

The value of W_f', and ultimately m, can determined directly from isothermal tests conducted outside the range of embrittlement. In this case, isothermal LCF tests should be conducted to failure and the stress-strain history recorded. The calculation of the inelastic component of strain additionally requires a good measurement of the Young's modulus at the tested temperatures. This can pose experimental challenges at high temperatures where creep can occur quickly. It is recommended in this case to determine the Young's modulus from fully-elastic cycles conducted at 1 Hz or higher, rather than using the linear slope of a tensile stress-strain curve.

For values of W_f' at intermediate temperatures where the embrittlement is active, a parabolic interpolation scheme was used in the dissertation work, which required at least three measured points, with at least one above and below the interpolation range. The values of W_f' measured from isothermal tests at room temperature and 200 °C were very similar, while those measured from tests at 720 and 800 °C were also similar. The value measured at 600 °C, where embrittlement was not found to be damaging in the dissertation work, provided the additional resolution needed to fit a smooth, monotonic curve through the intermediate temperatures. If the range of embrittled temperatures were known more precisely, a linear interpolation could be used. However, it would still be necessary to find the maximal and minimal values of W_f' (at low and high temperatures, respectively), and the shape of the intermediate curve.

Finally, cyclic tests must be conducted in the embrittled temperature range to numerically optimize α, which represents the severity of the damage due to the embrittlement of HiSiMo at 400 °C. In the dissertation work, similar values for the parameter were found whether numerical optimization was performend with the em-

brittled isothermal data alone or in conjunction with the embrittled TMF data, or if the TMF data was used alone. Therefore, at a minimum, isothermal LCF tests near 400 °C would be suitable to determine the value of α. Additional TMF tests conducted in the embrittled temperature range would be useful to validate the model parameters.

As a general guideline, it is recommended that the following tests be conducted to determine the parameters of the modified inelastic strain energy dissipation model:

1. Load-controlled cyclic tests to measure the Young's modulus at elevated temperatures,
2. Tensile tests between 250 and 550 °C to determine the temperature range where embrittlement is active,
3. Isothermal LCF tests at room temperature and the maximum temperature of consideration,
4. Isothermal LCF tests at an intermediate temperature outside the embrittled temperature range (preferably at a higher temperature),
5. Isothermal LCF tests at/near the temperature of maximum embrittlement,
6. Validation tests of anisothermal cycles.

Many commercial testing houses and university researchers now have the capability to perform high temperature isothermal tests. At present, few of these sources are able perform TMF tests; however, many are currently building capabilities in this area. Bithermal tests, and other anisothermal loading cycles, have been widely employed in the literature and could similarly be used for validation purposes.

5.6.2 Assumptions About W_f'

W_f' is a coefficient that was introduced in Equation 5.9 to distinguish the differing effects of embrittlement which occur under tensile and compressive stresses. It is identical in meaning to W_f, which is the ordinate intercept in a plot of inelastic strain energy dissipated verses cycles to failure. In fact, the value of W_f' is assumed

to be equivalent to the value of W_f when the embrittlement is not active. This assumption was preliminarily justified by comparing the values of W_f for IP and OP TMF loading at 600 to 800 °C where the embrittlement is not active. In this case, the values of W_f are similar, and the conclusion is made that the ability of the material to dissipate energy due to tensile and compressive stresses are similar.

In the case of the IP and OP TMF tests for 600 to 800 °C, fractographic analysis of the tested specimens in Chapter III revealed many similarities in the failure modes. In particular, both conditions led to failure by propagation of a primary crack which initiated in a transgranular manner due to an oxide intrusion, and crack growth under both conditions was dominated by the linking of graphite nodules. The similarity of failure modes is important because the active failure mechanism is a key factor in the rate of damage accumulation. The second key factor is the temperature at which the failure mechanism is occurring. In this case, the temperature range is fairly narrow between 600 and 800 °C, and so the rates of damage due to the dominant mechanisms are similar.

If the TMF cycle were to occur entirely below the embrittled temperature, a significant difference may result in the IP and OP TMF lives due to the different strengths of ductile cast iron in tension and compression. In some cases, the compressive yield strength of a DCI can be up to 20 % higher than the tensile yield strength due to the reinforcing nature of the graphite nodules under compressive loads (*Ductile Iron Society*, 1998). In this case, the capacity of the material to dissipate energy due to tensile and compressive loads would not be equivalent, despite the inactivity of the embrittlement mechanism. Thus, Θ in its current form would not do well to represent the asymmetry of the dissipation capacity and a different function should be introduced. A thermal cycle within this temperature range was not considered of primary concern for the exhaust manifold application and so was not studied in the dissertation work. However, it could be relevant to other industries where HiSiMo DCI is

applied, or at certain locations in an exhaust manifold. Further experimentation by IP and OP TMF should be conducted in this case.

It is important to recognize that the model given by Equation 5.12 does not attempt to distinguish the phasing between the thermal and mechanical strains since this is, in a sense, a cyclic quantity. It only recognizes the instantaneous temperature at which a stress is applied, and the sign and magnitude of the stress. Thus, it should be similarly applicable for different phasings of the thermal and mechanical strains without significant modification to the form of Equation 5.12.

5.6.3 Influence of Creep Damage

Recall from Section 5.1 that no attempt was made to distinguish the plastic and creep components of the inelastic strain for this HiSiMo DCI. This is because a reasonable attempt was made in the dissertation to introduce significant creep damage to the HiSiMo material, but the material showed good resistance to creep under the conditions studied. Tests conducted at 800 °C at a slow strain rate of $5 \times 10^{-5}\,\mathrm{s}^{-1}$, and with the addition of a 10 minute hold time at the maximum tensile or compressive stress showed no significant difference in the Coffin-Manson plots when compared to the LCF tests (conducted at $5 \times 10^{-3}\,\mathrm{s}^{-1}$), despite the vastly different proportions of creep and plastic damage that should occur in these cycles. Similarly, there was no difference in the Coffin-Manson plots for cyclic creep and LCF tests conducted at 600 °C. Thus, the value of W_f' does not vary with strain rate or hold time, since these did not greatly influence either the stress-strain cycle nor the number of cycles to failure for the HiSiMo DCI.

It is important to note that creep damage was observed in fractographic observations of tested specimens in Chapter II and Chapter III. This mechanism, along with fatigue, oxidation and embrittlement, likely contributed to failure under isothermal and TMF conditions, even if it was not found to be predominant in this HiSiMo alloy

for the conditions studied. In fact, previous work on a similar DCI alloy by *Hazime et al.* (2003) considered creep to be the primary mode of damage which contributed to elevated temperature failure.

However, despite the lack of creep damage that was observed in the wide range of elevated temperature tests conducted in the dissertation work, it is hypothesized that no modification would be needed to the form of Equation 5.12 if it were applied to a HiSiMo alloy for which creep damage were more prevalent. Consider, for example, the IP and OP TMF tests for 300 to 800 °C. The damage mechanisms described in Chapter III for these tests were vastly differently: for the OP tests, intergranular fracture due to embrittlement was the predominant mode of crack growth, while for the IP tests, TMF damage occurred predominantly by intrusion of a cyclically fractured oxide layer. Because the failure modes were very different, the TMF lives were correspondingly different. However, the effect of each failure mode was captured by the magnitude of W_f' (or W_f' modified by Θ) since it influenced the TMF life, and the TMF lives were well-predicted.

Similarly, the effect of creep, should it be found to influence the fatigue life or stress-strain behavior, would additionally influence the value of W_f' at high temperatures. Given the severe conditions which were employed in the dissertation work to introduce creep damage to this HiSiMo alloy, it would likely be necessary to utilize a different alloy composition for further experimentation to explore the suitability of the modified inelastic strain energy density model for cases where creep is a predominant factor in the TMF failure. In this case, it should be sufficient to follow the experimental testing scheme outlined in Section 5.6.1 to determine the temperature-dependent coefficient W_f' to account for the increased creep damage.

5.6.4 Use of a Representative Constitutive Model

The method proposed in the dissertation shows good correlation for uniaxial tests where the stress-strain behavior was measured directly from the experiment, and additionally for a component-level validation. However, the accuracy of a component-validation depends strongly the modeling strategy and quality of the different finite element analysis steps which contribute to the final prediction of fatigue life. In the dissertation work, it was necessary to conduct a computational fluid dynamics analysis, correlated to physical measurements of exhaust gas and wall temperatures, as well as a heat transfer analysis, a stress-strain analysis, and finally, a damage calculation. Additionally, it is imperative to use a constitutive model that is representative of the real material behavior for the loading cases and temperature considered. Particularly at high temperatures, it may be necessary to use a constitutive model that accounts for the viscoplastic behavior of the material, such as the *Chaboche* (1989) model employed in the dissertation work. Without an appropriate model to calculate the stresses and strains, the fatigue life prediction becomes meaningless. This limitation applies to all predictive methods, in the general case.

In particular for the dissertation work, it was necessary to use a constitutive model that could provide not only good accuracy of the stress-strain calculation at high temperatures, but also good representation for the small values of inelastic strain that were present in the component. Because the critical locations in the exhaust manifold experienced primarily plastic strains, due to the expansion and constraint of the material subjected to severe thermal gradients, it was not necessary to consider an additional expression for the elastic strains. However, in other industries, the conditions on HiSiMo components may be such that the loading is primarily elastic at high temperatures. In this case, a first approach would be to use the modification proposed by *Golos and Ellyin* (1988) to account for finite fatigue life occurring due to the energy dissipated by elastic strains.

CHAPTER VI

Conclusions and Future Work

The use of predictive technologies that can accurately represent the detrimental effect of transient thermal gradients can significantly reduce the time and expense needed to achieve a durable design. As reported in a 1991 literature review by *Halford*, a plethora of models exist in in the literature for predicting the high-temperature fatigue, fatigue-oxidation and creep-fatigue performance of engineering materials. Nearly all proposed models have shown applicability to a specific data set; however, most lack the generality that could allow them to be accurately employed outside the range of conditions or materials for which they were developed. Further challenges are presented by attempting to generalize an isothermal damage criterion to conditions of thermal cycling due to the unique and additional forms of damage that anisothermal cycle introduces. It is not a trivial process to resolve the challenges.

Many authors have attempted to apply isothermal fatigue life prediction to ansiothermal cycles with varying strategies – some have found good correlation by considering the maximum temperature of the thermal cycle, while others consider the minimum, or even average temperature of the cycle. Unfortunately, many previous works on fatigue life prediction under anisothermal conditions have failed to acknowledge that the cyclic quantities of stress and strain range develop under varying temperatures in an anisothermal cycle, where the strength and ductility of the material

is constantly changing. In an anisothermal cycle, these quantities are meaningless as measures of damage without reference to the temperature at which they develop.

The main contributions of this dissertation serve to partially overcome the challenges faced in predicting the high-temperature and thermomechanical fatigue life of a high silicon molybdenum (HiSiMo) ductile cast iron (DCI) for an automotive exhaust manifold application.

The first contribution of this dissertation is the generation of the most comprehensive, single-source database of high temperature durability data on HiSiMo DCI, including elevated-temperature tensile tests and low cycle fatigue tests at various strain rates, with and without hold times; creep tests; cyclic creep tests; and thermomechanical (TMF) tests. TMF tests were conducted for both in-phase (IP) and out-of-phase (OP) conditions. Different thermal cycles were used, and some TMF tests were additionally conducted with a hold time. More than 130 high temperature isothermal thermomechanical fatigue tests were conducted. The experimental work is reported in Chapter II for isothermal tests and Chapter III for TMF tests. These results indicate that the isothermal and thermomechanical fatigue lives are severely reduced in HiSiMo DCI when the temperature is near 400 °C. Thus, the embrittlement phenomenon, which was been extensively discussed in this dissertation, does not impact the IP TMF life. It was also determined that creep does not significantly influence the stress-strain behavior or the strain-life behavior of this HiSiMo alloy for conditions of isothermal or ansiothermal fatigue.

The second contribution of the dissertation is a thorough and detailed investigation of the physical mechanisms which cause damage in high temperature isothermal and thermomechanical fatigue of the HiSiMo DCI. For the isothermal tensile and fatigue tests, results are reported in Chapter II. In this work, the mechanisms of fatigue crack initiation and propagation were found to depend on temperature and strain range, and the observations were related to phenomenological behavior of the material where

the fatigue lives tend to converge at a high inelastic strain range. Particular attention was paid to the embrittled temperature, where it was clear from fractographic analysis that the embrittlement which occurs in HiSiMo significantly impacts the low cycle fatigue performance of the alloy, particularly when the strain (or stress) is high.

Similar observations were made in Chapter III for TMF tests with varying thermal range, phasings of the mechanical and thermal strains, and hold times. For TMF, the failure mode depended strongly on the temperature range and phasing of the mechanical and thermal strains. The observations made confirmed the embrittlement was only damaging in the application of a *tensile* stress, and discovery later informed the model to predict the fatigue life based on the different rates at which damage accumulates in tension and compression.

The third contribution of this dissertation is a robust method to predict the TMF life of the candidate material under conditions of severe thermal cycling. First, the state-of-the-art Neu-Sehitoglu model (1989b) was applied to the more than 130 uniaxial fatigue and TMF tests conducted for the dissertation work in Chapter IV. After careful fitting of the many experimentally-determined parameters, it was found that the Neu-Sehitoglu model was not well-suited for use with HiSiMo DCI because damage in this material accumulates non-monotonically with temperature, and the model has no term that can account for such behavior. Therefore, a new predictive framework was developed which was based on consideration of inelastic strain energy dissipation, and is described in Chapter IV. This new model, which accounts for different rates of damage accumulation in tension and compression, includes a temperature-dependent term that modifies the tensile portion of the energy dissipation to account for the 400 °C embrittlement of HiSiMo DCI. It provides good correlation with uniaxial tests, as well as a component-level validation for a HiSiMo manifold design that had been subjected to dynamometer testing. The model and validation cases are presented in Chapter V.

Together, these contributions provide a significant development in the understanding of the high temperature isothermal and thermomechanical fatigue behavior of high silicon molybdenum ductile cast iron. Furthermore, they establish a general criteria for predicting the TMF life of HiSiMo DCI that is informed by the real behavior of the material.

6.1 Future Work

Further work is recommended to develop the generality of the modified inelastic strain energy dissipation approach for fatigue life prediction under anisothermal conditions. In particular, the limitations addressed at the end of Chapter V are proposed for further study.

6.1.1 Application of Model to Creep-Dominated Failure

The HiSiMo DCI considered in the dissertation work did not tend to fail by creep-dominated effects under the conditions considered in the present study, although tests were conducted at slow strain rates and with hold times at 800 °C, and cyclic creep tests were conducted at 600 °C. In general, these tests could be expected to greatly increase the proportion of creep damage in the fatigue cycle. However, they failed to show a difference in life from the LCF tests. It is recommended that the model be applied to a different HiSiMo alloy, or to specific tests conditions where creep has been experimentally shown to contribute meaningfully to failure. The test temperature should not be greatly increased, since HiSiMo DCI undergoes a phase transformation near 810 to 840 °C (*Sponseller et al.*, 1968). However, a suitable alloy with a lower content of molybdenum (0.48 % was used in the present study) could be more susceptible to creep damage.

In an effort to extend the use of the model to other materials, an interesting future study would include a material where compressive stresses are found to be more

damaging than tensile stresses, whether the damage occurs by creep or some other mechanism. Since the contribution of damage is determined separately for tensile and compressive stresses, it should be able to represent damage in those materials where compressive loads cause a greater loss of isothermal or thermomechanical fatigue performance.

6.1.2 Application to Realistic Thermal Cycles

Future work should include an effort to reduce the minimum temperature of the TMF cycle to near ambient conditions. This represents a more realistic use case, since the temperature at the critical crack location in Chapter V was found to vary between about 60 °C and 750 °C. In particular, an interesting aspect of the work would consider the difference in an IP and OP TMF cycle which occurs entirely below the embrittled temperature. Since the compressive strength of a nodular cast iron is generally much greater than its tensile strength (*Ductile Iron Society*, 1998), the capacity of the material to dissipate energy due to tensile and compressive loads may not be equivalent, despite the inactivity of the embrittlement mechanism. Such a consideration could be relevant to other industries where HiSiMo DCI is applied.

6.1.3 Refine the Definition of Model Parameters

Finally, future work should seek to refine the physical meaning of the tensile and compressive components of W_f'. Introduced in Equation 5.7 as W_f^T and W_f^C, these terms segregate the differing effects of embrittlement which occur under tensile and compressive stresses. An experimental test plan which systematically varies the proportions of energy dissipation due to compressive and tensile stresses would likely develop a relationship between W_f^T and W_f^C such that the empirical parameter α could be related to a material property.

APPENDIX

APPENDIX A

Non-Destructive Evaluation of Cast Bars

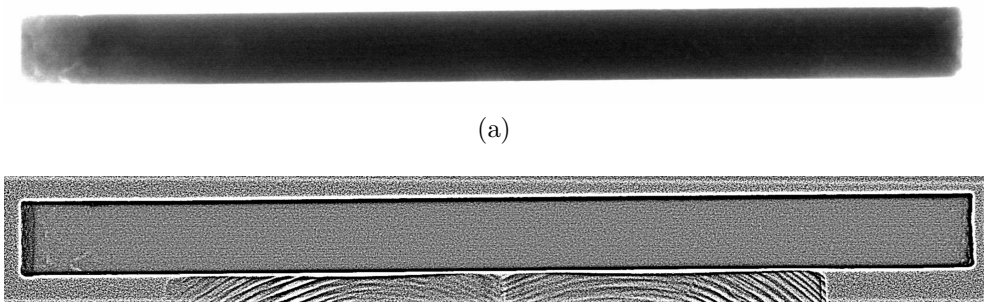

(a)

(b)

Figure A.1: (a) Raw radiograph of Bar 1 of 10 randomly selected cast bars. (b) Porosity-filtered image of the same radiograph.

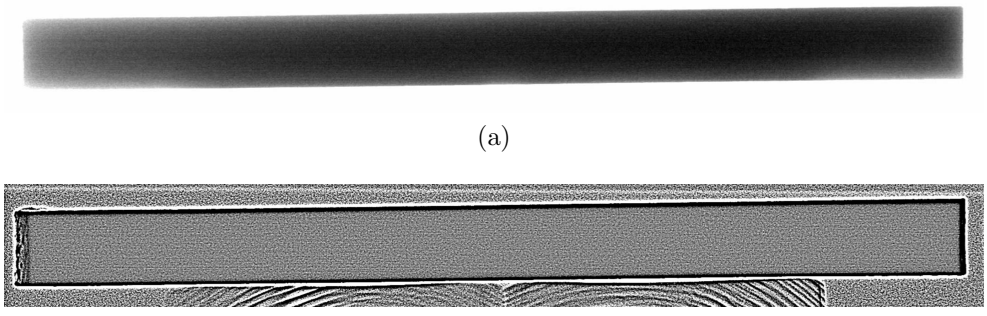

(a)

(b)

Figure A.2: (a) Raw radiograph of Bar 2 of 10 randomly selected cast bars. (b) Porosity-filtered image of the same radiograph.

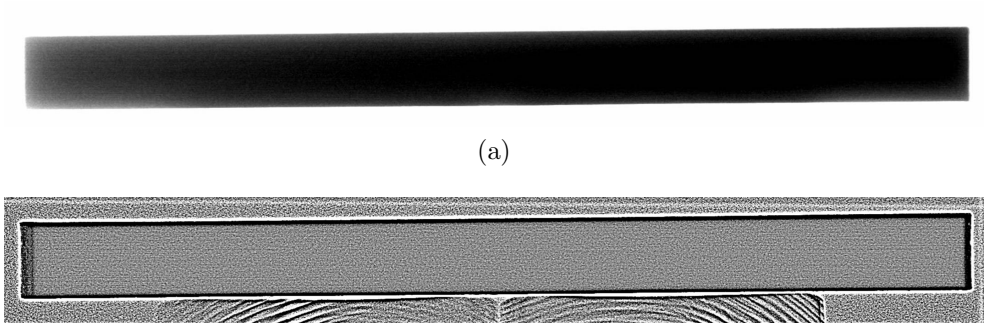

(a)

(b)

Figure A.3: (a) Raw radiograph of Bar 3 of 10 randomly selected cast bars. (b) Porosity-filtered image of the same radiograph.

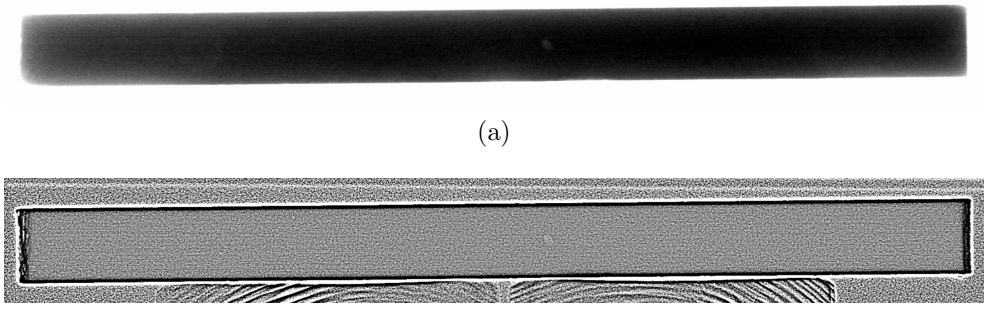

(a)

(b)

Figure A.4: (a) Raw radiograph of Bar 4 of 10 randomly selected cast bars. (b) Porosity-filtered image of the same radiograph.

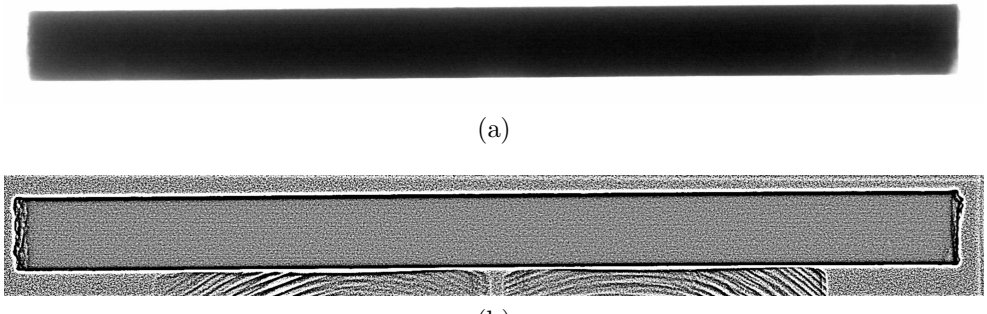

(a)

(b)

Figure A.5: (a) Raw radiograph of Bar 5 of 10 randomly selected cast bars. (b) Porosity-filtered image of the same radiograph.

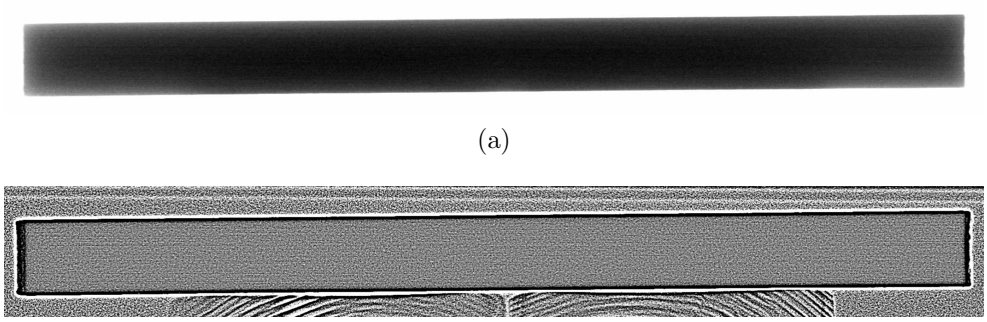

(a)

(b)

Figure A.6: (a) Raw radiograph of Bar 6 of 10 randomly selected cast bars. (b) Porosity-filtered image of the same radiograph.

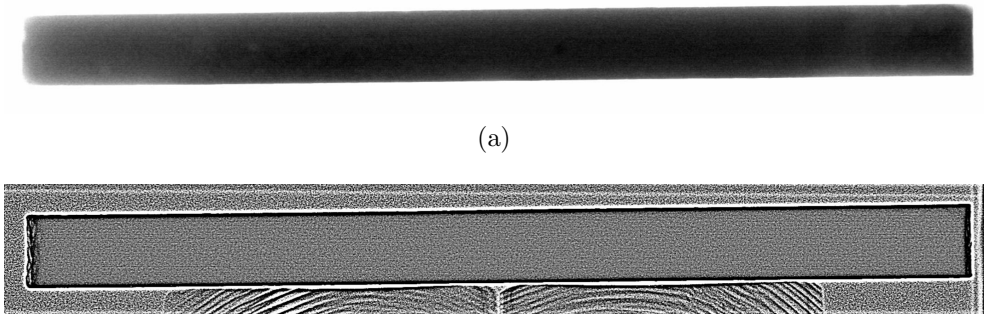

(a)

(b)

Figure A.7: (a) Raw radiograph of Bar 7 of 10 randomly selected cast bars. (b) Porosity-filtered image of the same radiograph.

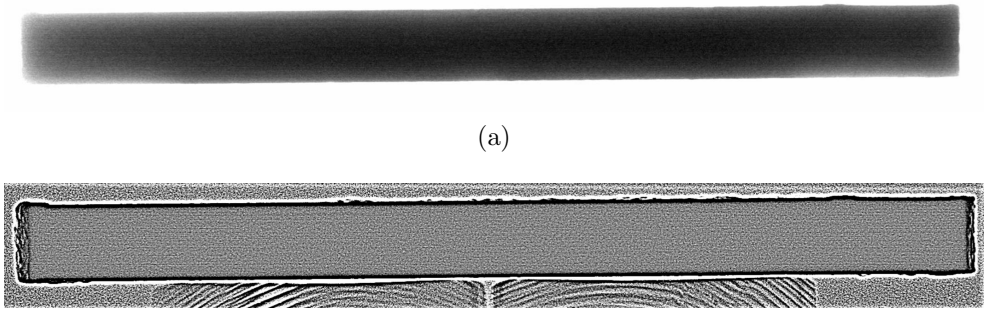

(a)

(b)

Figure A.8: (a) Raw radiograph of Bar 8 of 10 randomly selected cast bars. (b) Porosity-filtered image of the same radiograph.

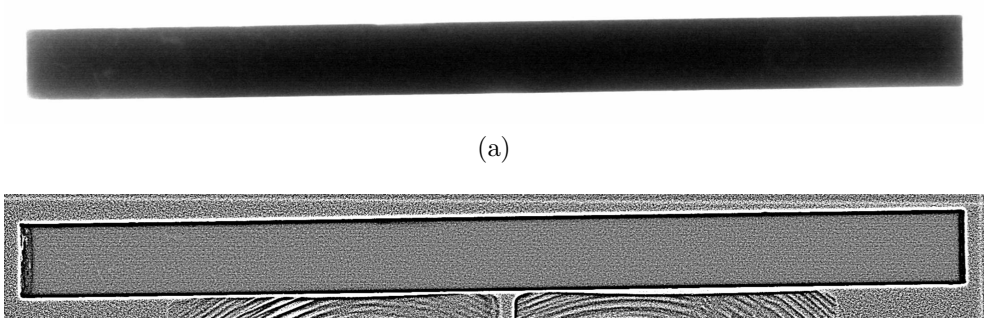

(a)

(b)

Figure A.9: (a) Raw radiograph of Bar 9 of 10 randomly selected cast bars. (b) Porosity-filtered image of the same radiograph.

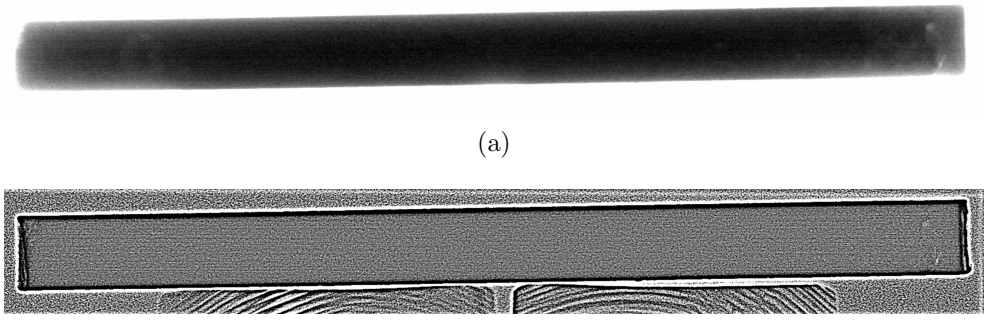

(a)

(b)

Figure A.10: (a) Raw radiograph of Bar 10 of 10 randomly selected cast bars. (b) Porosity-filtered image of the same radiograph.

BIBLIOGRAPHY

BIBLIOGRAPHY

Adewara, J., and C. Loper (1975), Effect of Carbides on Crack Initiation and Propagation in Ductile Iron, *Transactions of the Amercian's Foundryman's Society*, *83*, 507–512.

American Society of Mechanical Engineers (1984), Boiler and Pressure Vessel Piping Code, Section III, Case N-47-22.

American Society of Mechanical Engineers (1986), Boiler and Pressure Vessel Piping Code Section III, Case N-47-23.

Angus, H. (1960), *Cast Iron: Physical and Engineering Properties*, Butterworths.

Arkoosh, M., and N. Fiore (1972), Elevated Temperature Ductility Minimum in Hastelloy Alloy X, *Metallurgical Transactions*, *3*, 2235–2240.

ASTM A247 (2010), Standard Test Method for Evaluating the Microstructure of Graphite in Iron Castings.

ASTM E1012 (2014), Standard Practice for Verification of Testing Frame and Specimen Alignment Under Tensile and Compressive Axial Force Application.

ASTM E1019 (2011), Determination of Carbon, Sulfur, Nitrogen, and Oxygen in Steel and in Iron, Nickel, and Cobalt Alloys.

ASTM E1086 (2011), Standard Test Method for Analysis of Austenitic Stainless Steel by Spark Atomic Emission Spectrometry.

ASTM E112 (2013), Standard Test Methods for Determining Average Grain Size.

ASTM E1245 (2008), Standard Practice for Determining the Inclusion or Second-Phase Constituent Content of Metals by Automatic Image Analysis.

ASTM E1251 (2011), Standard Test Method for Analysis of Aluminum and Aluminum Alloys by Spark Atomic Emission Spectrometry.

ASTM E1999 (2011), Standard Test Method for Analysis of Cast Iron by Spark Atomic Emission Spectrometry.

ASTM E2368 (2010), Standard Practice for Strain-Controlled Thermomechanical Fatigue Testing.

ASTM E2567 (2014), Standard Test Method for Determining Nodularity and Nodule Count in Ductile Iron Using Image Analysis.

ASTM E415 (2014), Standard Test Method for Analysis of Carbon and Low-Alloy Steel by Spark Atomic Emission Spectrometry.

ASTM E606 (2004), Standard Practice for Strain-Controlled Fatigue Testing.

ASTM E8 (2009), Standard Test Methods for Tension Testing of Metallic Materials.

ASTM E83 (2010), Standard Practice for Verification and Classification of Extensometer Systems.

Avery, K., J. Pan, and C. Engler-Pinto (2015), Effect of Temperature Cycle on Thermomechanical Fatigue Life of a High Silicon Molybdenum Ductile Cast Iron, *Tech. Rep. 2015-01-0557*, Society of Automotive Engineers.

Baik, S., and R. Raj (1982a), Mechanisms of Creep-Fatigue Interaction, *Metallurgical Transactions A*, *13*, 1215–1221.

Baik, S., and R. Raj (1982b), Wedge Type Creep Damage in Low Cycle Fatigue, *Metallurgical Transactions A*, *13*, 1207–1214.

Basan, R., M. Franulovic, I. Prebil, and N. Crnjaric-Zic (2011), Analysis of Strain-Life Fatigue Parameters and Behaviour of Different Groups of Metallic Materials, *International Journal of Fatigue*, *33*, 484–491, doi::10.1016/j.ijfatigue.2010.10.005.

Basquin, O. (1910), The Exponential Law of Endurance Tests, *Proceedings of the American Society for Testing Materials*, *10*, 625–630.

Bastid, P. (1995), Comportement Thermomécaniques des Fontes à Graphite Sphéroïdal pour Collecteurs d'Échappement, Ph.D. thesis, École Nationale Supéprieure ds Mines de Paris.

Benoit, A., M. Maitournam, L. Rémy, and F. Oger (2012), Cyclic Behaviour of Structures Under Thermomechanical Loadings: Application to Exhaust Manifolds, *International Journal of Fatigue*, *38*, 65–74, doi:10.1016/j.ijfatigue.2011.11.012.

Bernard-Connolly, M., A. Biron, and T. Bui-Quoc (1978), Low-Cycle Cumulative Damage with Two Strain Repeated Blocks on a Stainless Steel at High Temperature, *Transactions of Candian Society of Mechanical Engineers*, *5*, 173–178.

Bouchaud, E., L. Kubin, and H. Octor (1991), Ductility and Dynamic Strain Aging in Rapidly Solidified Aluminum Alloys, *Metallurgical Transactions A*, *22*, 1021–1028.

Bui-Quoc, T., and A. Biron (1977), Low-Cycle Cumulative Fatigue Damage on a Stainless Steel at High Temperatures, *Pressure Vessel Technology*, *2*, 853–860.

Bui-Quoc, T., and R. Gomuc (1983), A Damage Approach for Analyzing the Combined Effect Under Creep-Fatigue Loading, in *Advances in Life Prediction*, edited by D. Woodford and J. Whitehead, pp. 105–113, American Society of Mechanical Engineers.

Chaboche, J. (1989), Constitutive Equations for Cyclic Plasticity and Cyclic Viscoplasticity, *International Journal of Plasticity*, *5*, 247–302.

Charkaluk, E., and A. Constantinescu (2000), An Energetic Approach in Thermomechanical Fatigue for Silicon Molybdenum Cast Iron, *Materials at High Temperatures*, *17*, 373–380, doi:0964-3409/00/01/0003512.

Charkaluk, E., A. Bignonnet, A. Constantinescu, and K. Dang Van (2002), Fatigue Design of Structures Under Thermomechanical Loadings, *Fatigue & Fracture of Engineering Materials & Structures*, *25*, 1199–1206, doi:10.1046/j.1460-2695.2002.00612.x.

Christ, H.-J. (2007), Effect of Environment on Thermomechanical Fatigue Life, *Materials Science and Engineering A*, *468-470*, 98–108, doi:10.1016/j.msea.2006.08.132.

Chute, H. (1907), Process of Making Steel, US Patent No. 874,391.

Coffin, L. (1954), A Study of the Effects of Cyclic Thermal Stresses on a Ductile Metal, *Transactions of the American Society of Mechanical Engineers*, *76*, 931–950.

Coffin, L. (1973), Fatigue at High Temperature, in *Fatigue at Elevated Temperatures*, STP 520, pp. 5–34, American Society for Testing and Materials.

Constantinescu, A., E. Charkaluk, G. Lederer, and L. Verger (2004), A Computational Approach to Thermomechanical Fatigue, *International Journal of Fatigue*, *26*, 805–818, doi:10.1016/j.ijfatigue.2004.01.006.

Davis, J. (Ed.) (1996), *ASM Specialty Handbook: Cast Irons*, ASM International, Materials Park, OH.

Di Cocco, V., F. Iacoviello, and M. Cavallini (2010), Damaging Micromechanisms Characterization of a Ferritic Ductile Cast Iron, *Engineering Fracture Mechanics*, *77*, 2016–2023, doi:10.1016/j.engfracmech.2010.03.037.

Di Cocco, V., F. Iacoviello, A. Rossi, M. Cavallini, and S. Natali (2012), Graphite Nodules and Fatigue Crack Propagation Micromechanisms in a Ferritic Ductile Cast Iron, *Fatigue & Fracture of Engineering Materials & Structures*, *36*, 893–902, doi:10.1111/ffe.12056.

Dong, M., C. Prioul, and D. Francois (1997), Damage Effect on the Fracture Toughness of Nodular Cast Iron: Part I. Damage Characterization and Plastic Flow Stress Modeling, *Metallurgical and Materials Transactions A*, *28*, 2245–2254.

Ductile Iron Society (1998), Ductile Iron Data for Design Engineers, http://www.ductile.org/didata/Section4/4intro.htm, accessed: 2015-06-16.

Eichlseder, W., G. Winter, and H. Köberl (2008), Material and Fatigue Life Models for Thermo-mechanical Loaded Components, *Materials Science & Engineering Technology*, *39*, 777–782, doi:10.1002/mawe.200800358.

Eldoky, L., and R. Voigt (1985), Fracture of Ferritic Ductile Cast Iron, *Transactions of the Amercian's Foundryman's Society*, *93*, 365–371.

Elliott, R. (1988), *Cast Iron Technology*, Butterworths, London, England.

Enomoto, N. (1955), On Fatigue Tests under Progressive Stress, in *ASTM*, vol. 55, p. 93.

Feltner, C., and J. Morrow (1961), Microplastic Strain Hysteresis Energy as a Criterion for Fatigue Fracture, *Journal of Fluids Engineering*, *83*, 15–22, doi:10.1115/1.3658884.

Fitzgeorge, D., and J. Pope (1953), British Shipbuilding Research Association, Report 123.

Gocmez, T., A. Awarke, and S. Pischinger (2010), A New Low Cycle Fatigue Criterion for Isothermal and Out-of-Phase Thermomechanical Loading, *International Journal of Fatigue*, *32*, 769–779, doi:10.1016/j.ijfatigue.2009.11.003.

Golos, K., and F. Ellyin (1988), A Total Strain Energy Density Theory for Cumulative Fatigue Damage, *Journal of Pressure Vessel Technology*, *110*, 36–41, doi:10.1115/1.3265565.

Goodrich, G. (Ed.) (2003), *Iron Castings Engineering Handbook*, American Foundary Society, Des Plaines, IL.

Gosar, A., and M. Nagode (2012), Energy Dissipation under Thermomechanical Fatigue Loading, *International Journal of Fatigue*, *43*, 160–167, doi:10.1016/j.ijfatigue.2012.03.011.

Halford, G. (1991), Evolution of Creep-Fatigue Life Prediction Models, in *Creep-Fatigue Interaction at High Temperatures*, vol. 21, edited by G. Haritos and O. Ochoa, pp. 43–57, American Society of Mechanical Engineers.

Halford, G., and J. Saltsman (1987), Calculation of Thermomechanical Fatigue Life Based on Isothermal Behavior, in *Thermal Stress, Material Deformation, and Thermo-Mechanical Fatigue*, vol. 123, edited by H. Sehitoglu and S. Zamrik, pp. 9–21, ASME.

Halford, G., B. Lerch, and V. Arya (2000), Thermal Strain Fatigue Modeling of a Matrix Alloy for a Metal Matrix Composite, *ASTM STP 1371*, pp. 186–203.

Hanstock, R. (1947), Damping Capacity, Strain Hardening and Fatigue, in *Physical Society*, vol. 59, pp. 275–287.

Hazime, R., S. Dropps, and D. Anderson (2003), Transient Non-Linear FEA and TMF Life Estimates of Cast Exhaust Manifolds, *Tech. Rep. 2003-01-0918*, Society of Automotive Engineers, doi:10.4271/2003-01-0918.

Heckel, T., and H.-J. Christ (2010), Thermomechanical Fatigue of the TiAl Intermetallic Alloy TNB-V2, *Experimental Mechanics*, *50*, 717–724, doi:10.1007/s11340-009-9264-3.

Hirschberg, M., and G. Halford (1976), Use of Strain-Range Partitioning to Predict High-Temperature Low-Cycle Fatigue, *Tech. Rep. NASA TN D-8072*, NASA.

Huang, Z., Z. Wang, S. Zhu, F. Yuan, and F. Wang (2006), Thermomechanical Fatigue Behavior and Life Prediction of a Cast Nickel-Based Superalloy, *Materials Science and Engineering A*, *432*, 308–316, doi:10.1016/j.msea.2006.06.061.

Inglis, N. (1927), Hysteresis and Fatigue of Wöhler Rotating Cantilever Specimen, *The Metallurgist*, *3*, 23–27.

Jaske, C. (1976), Thermal Fatigue of Materials and Components, *ASTM STP 612*, pp. 170–198.

Jaske, C. (1983), *Advances in Life Prediction Methods*, pp. 93–103, ASME.

Jaske, C., H. Mindlin, and J. Perrin (1973), Combined Low-Cycle Fatigue and Stress Relaxation of Alloy 800 and Type 304 Stainless Steel at Elevated Temperature, *ASTM STP 520*, pp. 365–376.

Jones, E. (2014), Wescast Industries, Inc., personal communication.

Karasek, M., H. Sehitoglu, and D. Slavik (1988), Deformation and Fatigue Damage in 1070 Steel under Thermal Loading, *ASTM STP 942*, pp. 184–205.

Kim, Y.-J., H. Jang, and Y.-J. Oh (2009), High-Temperature Low-Cycle Fatigue Property of Heat-Resistant Ductile-Cast Iron, *Metallurgical and Materials Transactions A*, *40*, 2087–2097, doi:10.1007/s11661-009-9911-4.

Kitagawa, M., and R. Weeks (1973), Analysis of Hold Time Fatigue Test Results of AISI 304 Stainless Steel by Five Existing Methods, in *Proc. Symposium on Mechanical Behavior of Materials*, pp. 233–338, Kyoto, Japan.

Kobayashi, T., K. Nishino, Y. Kimoto, Y. Awano, Y. Hibino, and H. Ueno (1998), 673 K Embrittlement of Ferritic Spheroidal Graphite Cast Iron by Magnesium, *Journal of Japan Foundary Engineering Society*, *70*(4), 273–278, doi:10.11279/jfes.70.273.

Korsunsky, A., D. Dini, F. Dunne, and M. Walsh (2007), Comparative Assessment of Dissipated Energy and Other Fatigue Criteria, *International Journal of Fatigue*, *29*, 1990–1995, doi:10.1016/j.ijfatigue.2007.01.007.

Laporte, V., and A. Mortensen (2009), Intermediate Temperature Embrittlement of Copper Alloys, *International Materials Review*, *54*, 94–116, doi:10.1179/174328009X392967.

Lederer, G., E. Charkaluk, and L. Verger (2000), Numerical Lifetime Assessment of Engine Parts Submitted to Thermomechanical Fatigue, Application to Exhaust Manifold Design, *Tech. Rep. 2000-01-0789*, Society of Automotive Engineers, doi:10.4271/2000-01-0789.

Lee, K.-O., S.-G. Hong, and S.-B. Lee (2008), A New Energy-Based Fatigue Damage PArameter in Life Prediction of High-Temperature Structure Materials, *Materials Science and Engineering A*, *496*, 471–477, doi:10.1016/j.msea.2008.07.035.

Lemaitre, J., and A. Pumtree (1979), Application of Damage Concepts to Predict Creep-Fatigue Failures, *Journal of Engineering Material Technology*, *101*, 284–292.

Levaillant, C., and A. Pineau (1982), Assessment of High-Temperature Low-Cycle Fatigue Life of Austenitic Stainless Steels by Using Intergranular Damage as a Correcting Parameter, in *Low-Cycle Fatigue and Life Prediction*, pp. 169–193, ASTM STP 770.

Li, D., R. Perrin, G. Burger, D. McFarlan, B. Black, R. Logan, and R. Williams (2004), Solidification Behavior, Microstructure, Mechanical Properties, Hot Oxidation and Thermal Fatigue Resistance of High Silicon SiMo Nodular Cast Iron, *Tech. Rep. 2004-01-0792*, Society of Automotive Engineers, doi:10.4271/2004-01-0792.

Liu, H., and Y. Oshida (1986), Grain Boundary Oxidation and Oxidation Accelerated Fatigue Crack Nucleation and Propagation, *Theoretical and Applied Fracture Mechanics*, *6*, 85–94.

Lui, G.-Y., M. Behling, and G. Halford (2000), Bithermal Low-Cycle Fatigue Evaluation of Automotive Exhaust System Alloy SS409, *Fatigue and Fracturing of Engineering Materials and Structures*, *23*, 787–794.

Majumdar, S. (1987), Thermomechanical Fatigue of Type 304 Stainless Steel, in *Thermal Stress, Material Deformation and Thermo-Mechanical Fatigue*, pp. 31–36, ASME.

Majumdar, S., and P. Maiya (1976), A Unified and Mechanistic Approach to Creep-Fatigue Damage, *Tech. Rep. ANL-79-58*, Argonne National Laboratory.

Majumdar, S., and P. Maiya (1979), Creep-Fatigue Interactions in an Austenitic Stainless Steel, *Canadian Metallurgical Quarterly*, *18*, 57–64.

Majumdar, S., and P. Maiya (1980), A Mechanistic Model for Time-Dependent Fatigue, *Journal of Engineering Material and Technology*, *102*, 159–167, doi:10.1115/1.3224774.

Manson, S. (1953), Behavior of Materials under Conditions of Thermal Stress, *Tech. Rep. NACA-TN-2933*, National Advisory Committee for Aeronautics.

Manson, S. (1973), The Challenge to Unify Treatment of High Temperature Fatigue - A Partisan Proposal Based on Strain-Range Partitioning, *ASTM STP 520*, pp. 744–782.

Manson, S., and G. Halford (2009), *Fatigue and Durability of Metals at High Temperatures*, ASM International.

Manson, S., G. Halford, and M. Hirschberg (1971), Creep-Fatigue Analysis by Strain-Range Partitioning, in *Proc. of First Symposium on Desing for Elevated Temperature Environment*, edited by S. Zamrik, pp. 12–24.

Mao, J., C. Engler-Pinto, and X. Su (2015), Comparative Assessment of Elasto-Viscoplatic Models for Thermal Stress Analysis of Autotmotive Powertrain Component, *SAE Tecnical Paper 010533*, doi:10.4271/2015-01-0533.

Maurel, V., L. Rémy, F. Dahmen, and N. Haddar (2009), An Engineering Model for Low Cycle Fatigue Life Based on a Partition of Energy and Micro-Crack Growth, *International Journal of Fatigue*, *31*, 952–961, doi:10.1016/j.ijfatigue.2008.09.004.

Miller, M., D. McDowell, R. Oehmke, and S. Antolovich (1993), A Life Prediction Model for Thermomechanical Fatigue Based on Microcrack Propagation, in *Thermomechanical Fatigue Behaviour of Materials*, edited by H. Sehitoglu, STP 1186, pp. 35–49, American Society for Testing and Materials, Philadelphia, PA.

Millis, K. (1949), Cast Ferrous Alloy, US Patent No. 2,485,760.

Min, B., and R. Raj (1978), Hold-Time Effects in High Temperature Fatigue, *Acta Metallurgica*, *26*, 1007–1022.

Minichmayr, R., M. Riedler, G. Winter, H. Leitner, and W. Eichlseder (2008), Thermo-mechanical Fatigue Life Assessment of Aluminum Components Using the Damage Rate Model of Sehitoglu, *International Journal of Fatigue*, *30*, 298–304, doi:10.1016/j.ijfatigue.2007.01.054.

Minkoff, I. (1983), *The Physical Metallurgy of Cast Iron*, John Wiley and Sons.

Nagesha, A., M. Valsan, R. Kannan, K. Bhanu Sankara Rao, V. Bauer, H.-J. Christ, and V. Singh (2009), Thermomechanical Fatigue Evaluation and Life Prediction of 316L(N) Stainless Steel, *International Journal of Fatigue*, *31*, 636–643, doi:10.1016/j.ijfatigue.2008.03.019.

National Highway Traffic Safety Administration (2008), Ford to Equip Half a Million Vehicles with EcoBoost Engine Technology for up to 20 Percent Better Fuel Economy, `http://www.at.ford.com/news/cn/ArticleArchives/26521.aspx`, accessed: 2015-06-12.

National Highway Traffic Safety Administration (2014), CAFE - Fuel Economy, `http://www.nhtsa.gov/fuel-economy`, accessed: 2015-04-02.

Neu, R., and H. Sehitoglu (1989a), Thermomechanical Fatigue, Oxidation and Creep: Part I.Damage Mechanisms, *Metallurgical Transactions A*, *20A*, 1755–1767.

Neu, R., and H. Sehitoglu (1989b), Thermomechanical Fatigue, Oxidation and Creep: Part II. Life Prediction, *Metallurgical Transactions A*, *20A*, 1769–1783.

Nissley, D. (1995), Thermomechanical Fatigue Life Prediction in Gas Turbine Superalloys: A Fracture Mechanics Approach, *Journal of the American Institute of Aeronautics and Astronautics*, *3*, 1114–1120.

Norman, B., D. Keith, and P. Albert (1949), Cast Ferrous Alloy, uS2485760 A.

Office of the Press Secretary (2012), Obama Administration Finalizes Historic 54.5 MPG Fuel Efficiency Standards, `https://www.whitehouse.gov/the-press-office/2012/08/28/obama-administration-finalizes-historic-545-mpg-fuel-efficiency-standard`, accessed: 2015-04-02.

Office of Transportation and Air Quality (2012), Gas Guzzler Tax Program Overview, `http://www.epa.gov/fueleconomy/guzzler/420f12068.pdf`, accessed: 2015-06-12.

Ostergren, W. (1976), A Damage Function and Associated Failure Equations for Predicting Hold-Time and Frequency Effects in Elevated Temperature, Low-Cycle Fatigue, *Journal of Testing and Evaluation*, *4*, 327–339.

Park, S., J. Kim, H. Kim, S. Ko, H. Park, and J. Lim (2005), Development of Heat Resistant Cast Iron Alloy for Engine Exhaust Manifolds, *Tech. Rep. 2010-01-1688*, Society of Automotive Engineers, doi:10.4271/2005-01-1688.

Park, Y., R. Gundlach, and J. Janowak (1987), Effects of Molybdenum on Thermal Fatigue Resistance of Ductile and Compacted Graphite Irons, *Transactions of the Amercian's Foundryman's Society*, *95*, 267–272.

Quan, T. (2015), Wescast Industries, Inc., personal communication.

Rémy, L., F. Szmytka, and L. Bucher (2013), Constitutive Models for BCC Engineering Iron Alloys Exposed to Thermal-Mechanical Fatigue, *International Journal of Fatigue*, *53*, 2–14, doi:10.1016/j.ijfatigue.2011.11.007.

Reuchet, J., and L. Rémy (1979), High Temperature Fatigue Behavior of a Cast Cobalt-Base Superalloy, *Fatigue & Fracture of Engineering Materials & Structures*, *2*, 51–62, doi:10.1111/j.1460-2695.1979.tb01342.x.

Rie, K.-T., and R.-M. Schmidt (1987), Lifetime Prediction Under Creep-Fatigue Conditions, in *Int. Conf. on Low Cycle Fatigue and Elasto-Plastic Behaviour of Materials*, pp. 223–228, Munich, Germany.

Robinson, E. (1952), Effect of Temperature Variation on the Long-Time Strength of Steels, *Transactions of ASME*, *73*, 777–780.

Roth, M., and H. Biermann (2008), Thermo-mechanical Fatigue Behaviour of a Modern $\gamma-$tial alloy, *International Journal of Fatigue*, *30*, 352–356, doi:10.1016/j.ijfatigue.2007.01.049.

Roth, M., G. Weatherly, and W. Miller (1980), The Temperature Dependence of the Mechanical Properties of Aluminum Alloys Containing Low-Melting-Point Inclusions, *Acta Metallurgica*, *28*, 841–853.

SAE J2582 (2001), Automotive Ductile Iron Castings for High Temperature Applications.

Sandchez-Medina, M., R. Sangiorgi, and N. Eustathopouslos (1981), On the Embrittlement of Copper by Liquid Lead Inclusions, *Scripta Metallurgica*, *15*, 737–738.

Saxena, A., and J. Bassani (1984), Time-Dependent Fatigue Crack Growth at Elevated Temperature, in *Proc. of AIME on Fracture: Interactions of Microstructure, Mechanisms and Mechanic*, edited by J. Wells and J. Landes, pp. 357–383, AIME.

Seifert, T., and H. Riedel (2010), Mechanism-Based Thermomechanical Fatigue Life Prediction of Cast Iron. Part I: Models, *International Journal of Fatigue*, *32*, 1358–1367, doi:10.1016/j.ijfatigue.2010.02.004.

Seifert, T., G. Maier, A. Uihlein, K.-H. Lang, and H. Riedel (2010), Mechanism-Based Thermomechanical Fatigue Life Prediction of Cast Iron. Part II: Comparison of Model Predictions with Experiments, *International Journal of Fatigue*, *32*, 1368–1377, doi:10.1016/j.ijfatigue.2010.02.005.

Seifert, T., R. Hazime, and S. Dropps (2014), TMF Life Prediction of High Temperature Components Made of Cast Iron HiSiMo: Part II: Multiaxial Implementation and Component Assessment, *SAE International Journal of Materials and Manufacturing*, *7*, 421–431, doi:10.4271/2014-01-0905.

Simon, V., G. Oberholz, and M. Mayer (2000), Exhaust Gass Temperature1050 °C, *Tech. rep.*, Borg Warner Turbo Systems.

Sivak, M., and B. Schoettle (2015), Fuel-Economy Distributions of Purchased New Vehicles in the U.S.: Model Years 2008 and 2014, *Tech. Rep. UMTRI-2015-4*, University of Michigan Transportation Research Institute.

Skelton, R. (1978), Environment Crack Growth in 0.5Cr-Mo-V Steel During Isothermal High Strain Fatigue and Temperature Cycling, *Materials Science and Engineering*, *35*, 287–298.

Skelton, R. (1991), Energy Criteria for High Temperature Low Cycle Fatigue, *Materials Science Technology*, *7*, 427–439.

Skelton, R. (2004), Hysteresis, Yield, and Energy Dissipation During Thermomechanical Fatigue of a Ferritic Stainless Steel, *International Journal of Fatigue*, *26*, 253–264, doi:10.1016/S0142-1123(03)00144-0.

Skelton, R., G. Webster, B. de Mestral, and C.-Y. Wang (2000), Modelling Thermo-Mechanical Fatigue Hysteresis Loops from Isothermal Cyclic Data, in *Thermo-Mechanical Fatigue Behaviour of Materials*, edited by H. Sehitoglu and H. Maier, STP 1371, pp. 69–84, American Society of Testing and Materials, West Conshohocken, PA.

Smith, K., P. Watson, and T. Topper (1970), A Stress-Strain Function for the Fatigue of Metals, *Journal of Materials*, *5*, 767–778.

SOP CH-IO-002 (2015), Element Wixom Standard Operating Procedure.

Spera, D. (1969), Calculation of Thermal-Fatigue Life Based on Accumulated Creep Damage, *Tech. Rep. NASA TN D-5489*, NASA.

Sponseller, D., W. Scholz, and D. Rundle (1968), Development of Low-Alloy Ductile Irons for Service at 1200-1500 F, *American Foundary Society Transactions*, *76*, 353–368.

Su, X., M. Zubeck, J. Lasecki, C. Engler-Pinto Jr., and C. Tang (2002), Thermal Fatigue Analysis of Cast Aluminum Cylinder Heads, *Tech. Rep. 2002-01-0657*, Society of Automotive Engineers, doi:10.4271/2002-01-0657.

Suzuki, H., S. Nishimura, J. Imamura, and Y. Nakamura (1981), Hot Ductility in Steels in the Temperature Range Between 900 and 600 deg C: Related to the Transverse Facial Crack in Continuously Cast Slabs, *The Journal of the Iron and Steel Institute*, *67*, 1180–1189.

Swindeman, R., and D. Douglas (1959), The Failure of Structural Metals Subjected to Strain-Cycling Conditions, *Journal of Basic Engineering*, *81*, 203–212.

Szmytka, F., L. Rmy, H. Maitournamc, A. Ksterb, and M. Bourgeoisa (2010), New Flow Rules in Elasto-Viscoplastic Constitutive Models for Spheroidal Graphite Cast-Iron, *International Journal of Plasticity*, *26*, 905–924, doi:doi:10.1016/j.ijplas.2009.11.007.

Taira, S. (1962), Lifetime of Structures Subjected to Varying Load and Temperature, in *Creep in Structures*, edited by N. Hoff, pp. 96–119, Springer Verlag.

Taira, S. (1973), Relationship Between Thermal Fatigue and Low-Cycle Fatigue at Elevated Temperatures, *ASTM STP 520*, pp. 80–101.

Thomas, J., L. Verger, A. Bignonnet, and E. Charkaluk (2004), Thermomechanical Design in the Automotive Industry, *Fatigue & Fracture of Engineering Materials & Structures*, *27*, 887–895, doi:10.1111/j.1460-2695.2004.00746.x.

Tien, J., S. Nair, and V. Nardone (1985), *Flow and Fracture at Elevated Temperatures*, pp. 179–213, ASM.

Tomkins, B. (1981), *Creep and Fatigue in High Temperature Alloys*, pp. 111–143, Applied Science Publishers, London.

von Hartrott, P., T. Seifert, and S. Dropps (2014), TMF Life Prediction of High Temperature Components Made of Cast Iron HiSiMo: Part I: Uniaxial Tests and Fatigue Model, *SAE International Journal of Materials and Manufacturing*, *7*, 439–445, doi:10.4271/2014-01-0915.

Wareing, J. (1977), Creep-Fatigue Interaction in Austenitic Stainless Steels, *Metallurgical Transactions A*, *8*, 711–721.

Weber, G., G. Faubert, M. Rothwell, A. Tagg, and D. Wirth (1998), High Si-Mo Ductile Iron: Views from Users and Producers, *Modern Casting*, *88*, 48–51.

Wilshire, B., and D. Owen (1983), *Engineering Approach to High Temperature Design*, vol. 2, pp. 177–235, Pineridge Press Ltd.

Wright, R., and T. Farrell (1985), Elevated Temperature Brittleness of Ferritic Ductile Iron, *Transactions of the American Foundryman's Society*, *93*, 853–866.

Wu, X., T. Quan, and C. Sloss (2013), Failure Mechanisms and Damage Model of Ductile Cast Iron under Low-Cycle Faitgue Conditions, *Tech. Rep. 2013-01-0391*, Society of Automotive Engineers, doi:10.4271/2013-01-0391.

Wu, X., G. Quan, R. MacNeil, Z. Zhang, X. Liu, and C. Sloss (2015), Thermomechanical Fatigue of Ductile Cast Iron and Its Life Prediction, *Metallurgical and Materials Transactions A*, *46*, 2530–2543, doi:10.1007/s11661-015-2873-9.

Yanagisawa, O., M. Maruyama, K. Arii, T. Ishigai, and M. Konishi (1980), Tensile and Fatigue Strength and Fracture of Spheroidal Graphite Cast Iron with Ferritic Matrix in Temperature Range from Room Temperature to 500C, *IMONO*, *52*, 331–336, doi:10.11279/imono.52.6_331.